

The CMS Experiment: on
and Under Ground Motions
of Structures Due to the
Magnetic Field Forces as
Observed by the Link
Alignment System

CIEMAT	IFCA/CSIC - UC	UNIV. OVIEDO
(Madrid)	(Santander)	(Oviedo)
J. Alberdi	J. Brochero	J. Fernández
P. Arce	A. Calderón	
J. M. Barcala	M. G. Fernández	
E. Calvo	G. Gómez	
A. Ferrando	F. J. González-Sánchez	
M. I. Josa	C. Martínez-Ribero	
A. Molinero	F. Matorras	
J. Navarrete	T. Rodrigo	
J. C. Oller	P. Ruiz-Arbol	
C. Yuste	L. Scodellaro	
	M. Sobrón	
	I. Vila	
	A. L. Virto	

Toda correspondencia en relación con este trabajo debe dirigirse al Servicio de Información y Documentación, Centro de Investigaciones Energéticas, Medioambientales y Tecnológicas, Ciudad Universitaria, 28040-MADRID, ESPAÑA.

Las solicitudes de ejemplares deben dirigirse a este mismo Servicio.

Los descriptores se han seleccionado del Thesaurus del DOE para describir las materias que contiene este informe con vistas a su recuperación. La catalogación se ha hecho utilizando el documento DOE/TIC-4602 (Rev. 1) Descriptive Cataloguing On-Line, y la clasificación de acuerdo con el documento DOE/TIC.4584-R7 Subject Categories and Scope publicados por el Office of Scientific and Technical Information del Departamento de Energía de los Estados Unidos.

Se autoriza la reproducción de los resúmenes analíticos que aparecen en esta publicación.

Catálogo general de publicaciones oficiales
<http://www.060.es>

Depósito Legal: M -14226-1995

ISSN: 1135 - 9420

NIPO: 471-10-018-X

Editorial CIEMAT

CLASIFICACIÓN DOE Y DESCRIPTORES

S71

MAGNETIC FIELDS; UNDERGROUND; ALIGNMENT; SOLENOIDS;
DATA ACQUISITION SYSTEMS; DETECTION; EVALUATED DATA

**The CMS Experiment: on and under Ground Motions of Structures Due to the Magnetic Field Forces
as Observed by the Link Alignment System**

Alberdi, J.; Arce, P.; Barcala, J. M.; Calvo, E.; Ferrando, A.; Josa, M.I.; Molinero, A.; Navarrete, J.;
Oller, J.C. and Yuste, C.
CIEMAT* (Madrid, Spain)

Brochero, J.; Calderón A.; Fernández, M. G.; Gómez, G.; González-Sánchez, F. J.;
Martínez-Ribero, C.; Matorras, F.; Rodrigo, T.; Ruiz-Arbol, P.; Scodellaro, L.; Sobrón, M.
Vila, I. and Virto, A. L.

Instituto de Física de Cantabria, CSIC- Univerity of Cantabria** (Santander, Spain)
Fernández, J.
University of Oviedo*** (Oviedo, Spain)
144 pp. 66 fig. 23 ref.

Abstract:

This document describes results obtained from the Link Alignment System data recorded during the CMS Magnet Test (at SX5 on ground Hall) and the CRAFT08 and 09 periods data taking in the point P5 (UX5), 100 m underground. A brief description of the system is followed by the discussion of the detected relative displacements (from micrometres to centimetres) between detector elements and rotation of detector structures (from microradians to milliradians). Observed motions are studied as functions of the magnetic field intensity. Comparisons between recorded data on and under ground are made.

**Movimientos de Estructuras del Experimento CMS, Debidos a la Acción del Campo Magnético Observados
por el Sistema de Alineamiento Link: Datos Sobre y Bajo Tierra**

Alberdi, J.; Arce, P.; Barcala, J. M.; Calvo, E.; Ferrando, A.; Josa, M.I.; Molinero, A.; Navarrete, J.;
Oller, J.C. and Yuste, C.
CIEMAT* (Madrid, España)

Brochero, J.; Calderón A.; Fernández, M. G.; Gómez, G.; González-Sánchez, F. J.;
Martínez-Ribero, C.; Matorras, F.; Rodrigo, T.; Ruiz-Arbol, P.; Scodellaro, L.; Sobrón, M.
Vila, I. and Virto, A. L.

Instituto de Física de Cantabria, CSIC- Univerity of Cantabria** (Santander, España)
Fernández, J.
University of Oviedo*** (Oviedo, España)
144 pp. 66 fig. 23 ref.

Resumen:

Este documento describe los resultados obtenidos con el Sistema de Alineamiento Link de CMS durante las pruebas del Solenoide en 2006 y las tomas de datos "CRAFT" 08 y 09, en el pozo, en 2008 y 2009. Se describe brevemente el sistema y se discuten los desplazamientos y rotaciones observados en las estructuras, comparando las observaciones hechas en superficie y en el punto P5 (UX5), 100 m bajo tierra.

*Under CICYT (Spain) Grant: FPA 2008-05696-C02-01.

**Under CICYT (Spain) Grant: FPA 2008-06112-C02-01

***Under CICYT (Spain) Grant: FPA 2008-06112-C02-02

1. Introduction

From the point of view of the muon measurement, the Compact Muon Solenoid Detector (CMS) [1-3] is a muon spectrometer and the detection of these particles is favored.

Attending to the magnet field intensity, two different technologies are employed for their measurement. In the barrel region, surrounding the coil of the solenoid, four layers of drift chambers, interleaved with the return iron yoke, will make a redundant measurement of the muon momenta. A muon chamber is made of three superlayers. Each superlayer is made of four layers of drift cells. The drift cell is the basic unit measuring the drift time of a muon, providing a spatial resolution of 250 μm . Each superlayer will contribute with a measurement of one coordinate. Two superlayers will measure the $R\Phi$ coordinate and one layer will measure the Z coordinate. The mechanical design of a drift chamber is driven by the precision in the determination of a point of the muon track, 100 μm , which is obtained by fit of the individual hits in each cell.

The muon drift chambers will be subject to variable residual magnetic fields, below 0.4 T for all the chambers except for the MB1 chamber near the endcaps. There, the magnetic field will rise up to 0.8 T. At the level of the ME1/1 chamber the field will be $B_z \approx 3$ T. For such magnetic field intensity the operation of the muon drift chambers is limited, since the drift cell escapes the linear regime. CMS uses, at the endcaps, other gaseous detectors called Cathode Strip Chambers (CSCs) that can operate in large and non-uniform magnetic fields without significant deterioration of performance. CSCs are multiwire proportional chambers in which one cathode plane is segmented into strips running across wires, both of them instrumented, giving 2D information of the particle passage. Due to the intense magnetic field, the trajectories of the muons bend more in the vicinity of the first endcap station where the higher precision requirement is needed (75 μm). For the rest of the chambers the precisions will be of about 150 μm .

As well known, the measurement of the muon momentum is related with its bending in the transverse plane. The radius of curvature ρ and the momentum perpendicular to the magnetic field (p_t) of a muon are related by $\rho[\text{m}] = p_t[\text{GeV}/c]/0.3 B[\text{T}]$. The radius of curvature can be obtained from the measurement of the muon trajectory sagita s , after traversing a distance d in the magnetic field, using the approximate expression $\rho = d^2/8s$.

An error in the sagita measurement results in an error in the momentum measurement. The relative error in the sagita measurement is $\delta s/s = \delta p_t/p_t \propto \sigma_s[\text{mm}]p_t[\text{TeV}]/d^2[\text{m}^2]B[\text{T}]$, where σ_s is the resolution in the sagita measurement. The relative resolution deteriorates with the muon momentum and improves linearly with the magnetic field and quadratically with the traversed distance.

The accuracy required in the position of the muon chambers is determined by the resolution demanded in the reconstruction of the momentum of high energy muons. CMS is designed to achieve a combined (Tracker and Muon System) momentum resolution for the region $|\eta| < 2.4$ of 0.5 – 1% for $p_t \approx 10$ GeV, 1.5 – 5% for $p_t \approx 100$ GeV and 5 – 20% for $p_t \approx 1$ TeV. This design accuracy will require the knowledge of the position of the chambers with a precision *comparable* to their resolution.

In order to quantify the importance of the chambers misalignment in the momentum resolution, several simulations studies have been performed [4]. As a result, for the most important coordinate from the physics point of view, $(R\Phi)$, the alignment system should reconstruct the position of the chambers within 150 – 300 μm range for MB1 – MB4 and within the 75 – 200 μm range for ME1 – ME4. The constraints are tighter for ME1 and MB1 since, as already said, most of the muons reach the maximum curvature near the first muon station. These stations give the main contribution to the momentum measurement precision and therefore lead the requirements of measurement resolution of the chamber and the accuracy on their position knowledge.

However, the stability of the muon chambers at the level of the 100 μm is not guaranteed at all when CMS enters in operation. The expected movements and deflections of the muon spectrometer will exceed this value. To monitor these movements, CMS is instrumented with an opto-mechanical alignment system that allows a continuous and precise information on the relative position of the muon chambers amongst them (in the barrel and endcaps), as well as on the position of the muon chambers with respect to the tracker, assumed to be a rigid body. The information provided by the alignment will be used for off-line corrections in the track reconstruction.

A test of part of the Alignment System [5] took place in summer and autumn 2006 when the CMS four Tesla Magnet was for the first time commissioned. The test (Magnet Test and Cosmic Challenge, MT) took place, in two different phases, in the SX5 assembly Hall at CERN. Several components of the Muon detector were also tested with cosmic rays [5].

In 2008 the full Link System was installed in CMS and took data in the P5 cavern and data was taken during the CRAFT (CMS Cosmics Run at Four Tesla) run. As from then it was decided that CMS will, in the future, operate at a maximum field of 3.8T and during 2009 several CRAFT09 runs took place at this magnet intensity. In this document we analyse on and under ground data and compare results when possible.

The data we are going to review is an input to the “CMS Object oriented Code for Optical Alignment”, COCOA [6], the software that makes the full geometrical reconstruction of positions and orientations, in the CMS space coordinates, of all mechanical structures and calculates the relative position and orientation of the Tracker Body with respect to the Muon Chambers.

In the present document we are going to restrict ourselves to the observation of motions and rotations of relevant CMS mechanical elements due to the various forces in presence: magnetic field, gravity, frictions, etc. without entering in the full spatial geometrical reconstructions that will be the object of a separated paper.

This document is organized as follows: An introduction to the CMS Alignment System, with special emphasis on the description of the Link Alignment System, is given in section 2 followed (section 3) by some notes devoted to the CMS magnetic field and the resulting forces. The information about the elements installed for the Magnet Test and for the underground runs are given in section 4, while some notes concerning the associated Data Acquisition and Detector Control Systems are given in section 5. In section 6 we give details about the data sets we have selected for analysis and comparisons of motions on and under ground.

Data analysis and comparison of observations among the various runs will start in section 7 that deals with the Link laser systems and photosensors information. Section 8 is devoted

to the study of relative displacements between pairs of CMS elements. The angular monitoring with electrolytic clinometers is the object of section 9.

Finally, summary and conclusions are presented in section 10.

2. The CMS Alignment System

A longitudinal view of a quarter of the detector is shown in Fig. 1, which includes marks and dimensions. A transverse view of the detector can be seen in Fig. 2, where the three alignment planes are shown. Finally, an overall layout of CMS is shown in Fig. 3.

At the heart of CMS sits a 13 m long, 6 m inner diameter, 4T superconducting solenoid, which provides a large bending power: 12 Tm. The return field is large enough to saturate 1.5 m of iron, allowing 4 muon stations to be integrated to ensure robustness and full geometrical coverage.

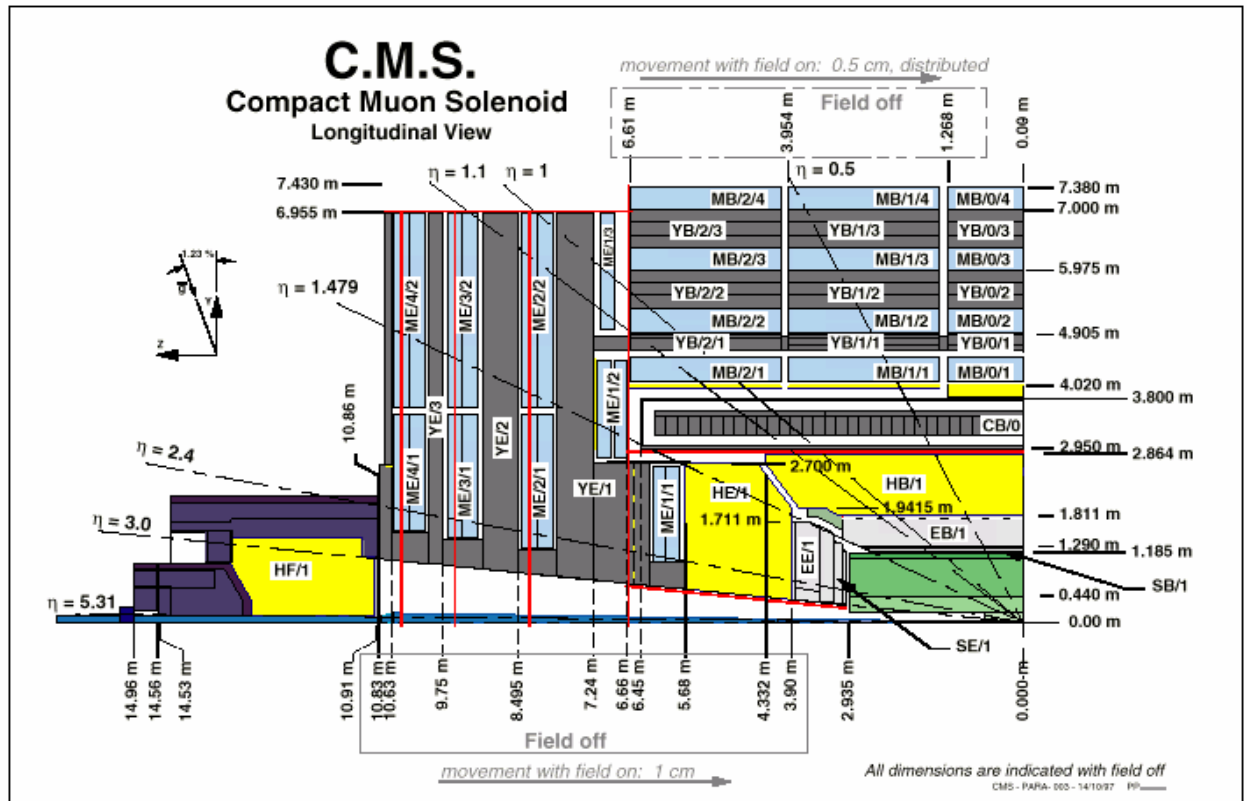


Fig. 1: Longitudinal view of a quarter of the CMS detector.

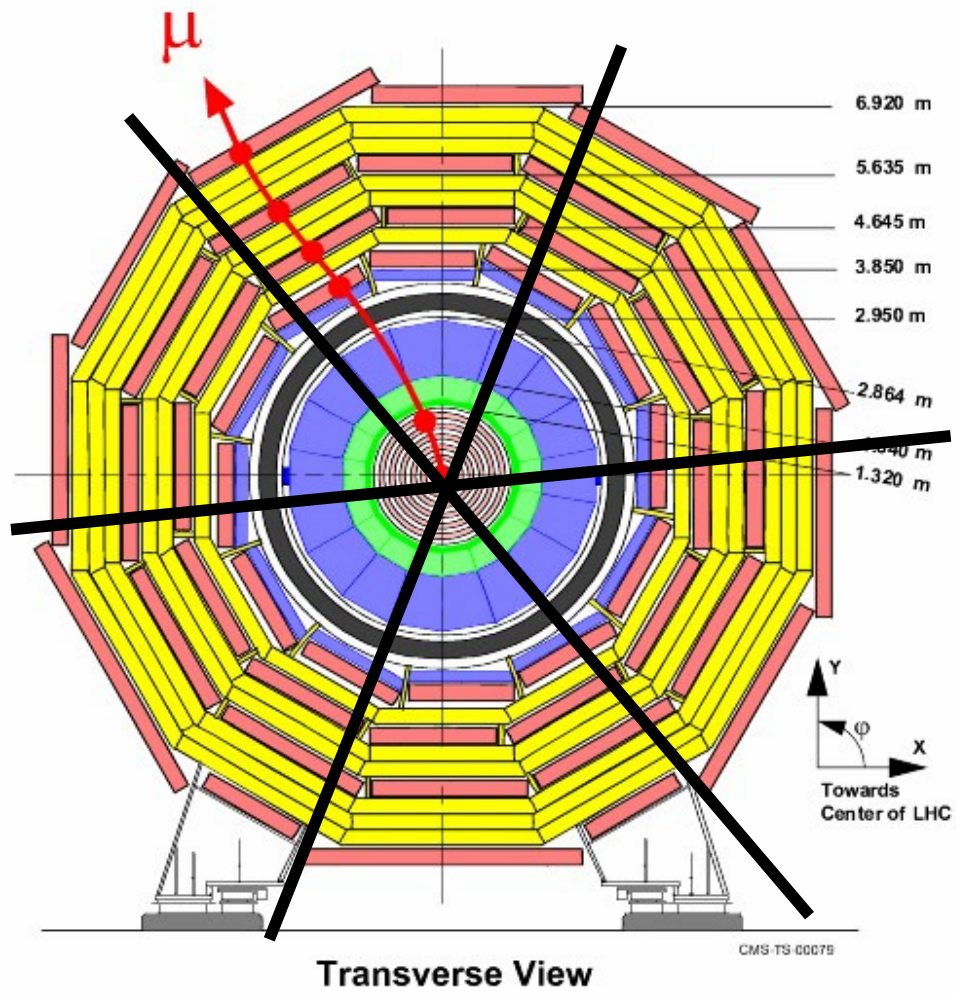


Fig. 2: Transverse view of the CMS detector with the three Alignment planes.

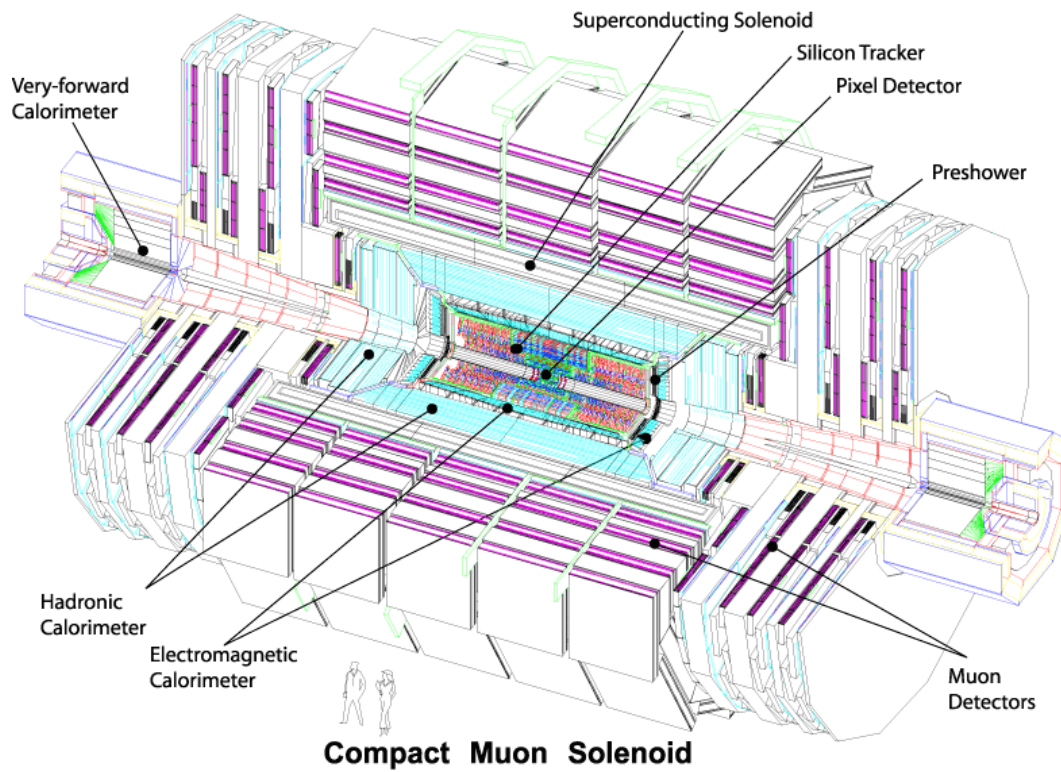


Figure 3: A perspective view of the CMS detector.

The muon system consists of about 25000 detection planes embedded in the 15 m diameter, 20 m long return yoke. To cope with all the muon momentum resolution requirements explained at the Introduction, the system is instrumented with a complex opto-mechanical Alignment System organised in three basic blocks:

- The Tracker internal alignment, to measure the positions of the various modules and monitor the eventual internal deformations.
- The Muon Systems (Barrel and Endcaps) internal alignment, to monitor the relative position among the chambers.
- The Link System, to relate the position of the various elements of the muon system (barrel and endcaps) with the position of the Tracker body, and to monitor the relative movements between both systems.

We show in Fig. 4 one of the Φ alignment planes where the three alignment subsystems can be seen. There are in total three Φ planes (see Fig. 2). Each plane contains four independent alignment quarters where the three systems are connected.

2.1 The Tracker Alignment

The alignment of the tracker units (silicon sensors) is done with internal laser beams (see Fig. 5). The Laser Alignment System (LAS) [7] uses infrared laser beams to monitor the position of selected tracker modules. It operates globally on tracker substructures and cannot determine the position of individual modules. The goal of the system is to generate alignment information on a continuous basis, providing the geometry of the tracker substructures at the level of 100 μm . In addition, possible tracker structures movements can be monitored at the level of 10 μm using offline alignment algorithms based on the information of the tracks crossing the detectors.

In each Tracker Endcap structure (TEC), 8 axial laser beams, distributed in R and Φ , cross all 9 endcap discs. At each TEC end-face, 3 mechanical supports –pillars- rigidly attached to the most external (9th) disc transfer the internal tracker geometry information to the outside world. The relation between the position of the Tracker body and the Muon Chambers systems (barrel and end-caps) is done through the Link System, and in particular by means of 12 laser beams (6 on each side) housed on a carbon fibre structure (Alignment Ring, AR) which is supported by the 3 TEC pillars. Its position and orientation is therefore known precisely in the tracker coordinate system. The goal is to monitor motions of the Muon structures with respect to the Tracker system with an accuracy of about 200 μm .

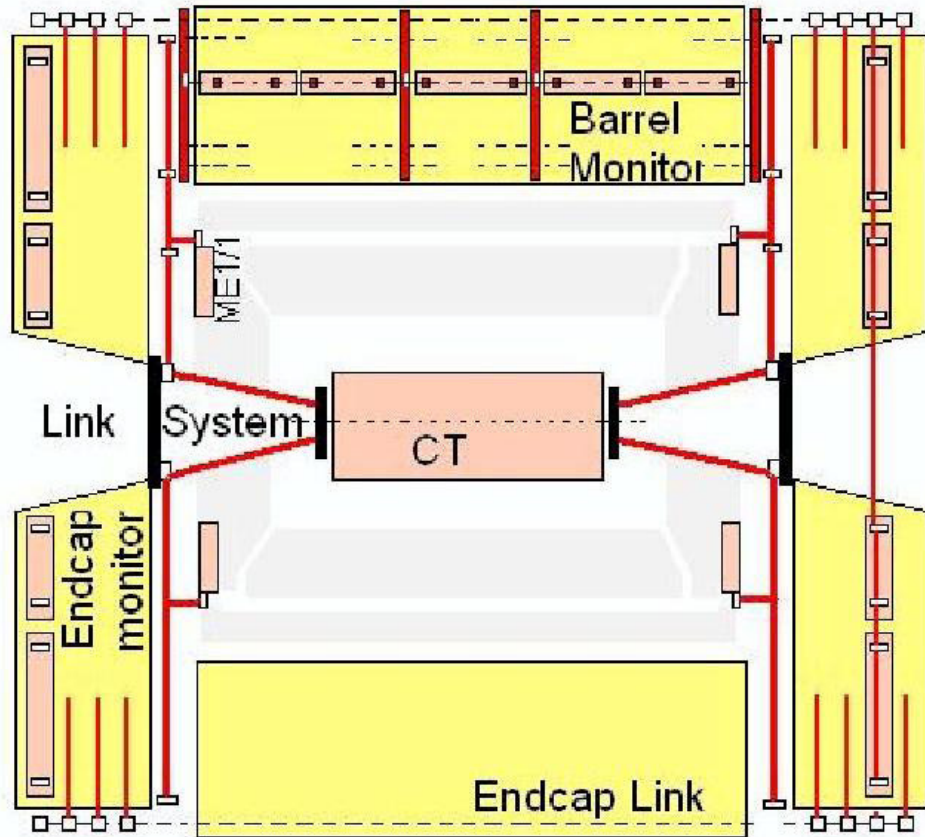


Fig. 4: One of the ϕ alignment planes showing the three alignment subsystems.

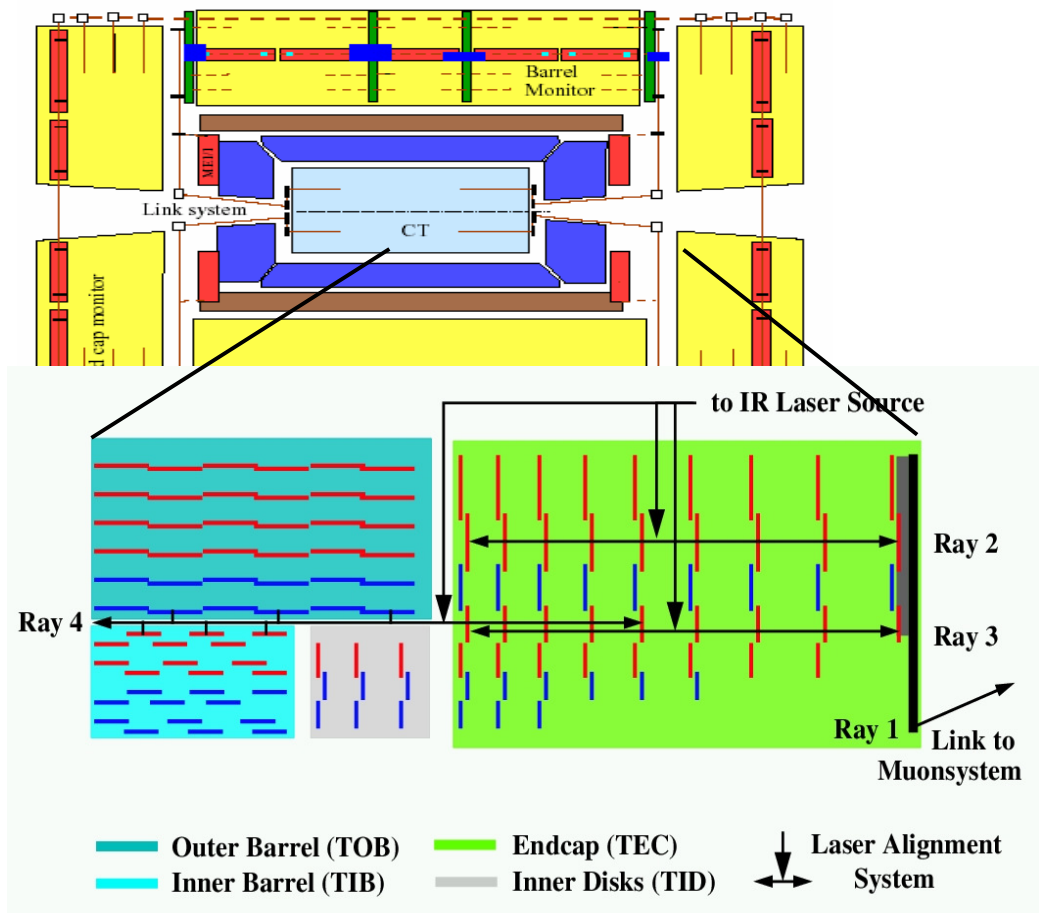


Fig. 5: The Tracker Alignment System

2.2 The Barrel Alignment

The Barrel Alignment system [3] measures the positions of the barrel muon chambers with respect to each other and to the whole barrel muon spectrometer (see sketch in Fig. 6). Each barrel muon chamber is equipped with light sources (LEDs, more than 9000 in total). The LEDs are observed by small video-cameras (600 in total) mounted on rigid carbon-fibre structures called MABs (Module for the Alignment of the Barrel). There are direct observations between the MABs called diagonal connections.

The system is completed with long carbon fibre bars called z-bars fixed to the vacuum-tank of the magnet. The z-bars (12 in total, 6 per side) are also equipped with LED light sources and observed by video-cameras mounted on the MABs. The MABs (36 altogether) are fixed to the return yoke in the gaps between the barrel wheels (6 per gap) and on both ends of the barrel (6 per side). The MABs on the two ends, containing Link and Endcap elements, are used to connect the three alignment subsystems to each other.

2.3 The Endcap Alignment

The Endcap Alignment system [8] is designed (see Fig. 7) to monitor the relative positions of the CSC chambers. The system uses a complex arrangement of 5 types of sensors for the transferring and monitoring of the Φ , R, and Z coordinates. It measures only a set of selected chambers per layer, in total a sixth of all endcap chambers.

The main monitoring tools within the R- Φ plane are the Straight Line Monitors (SLM). Each SLM consists of 2 cross-hair lasers, which emit a nearly radial laser beam across 4 chambers from each end, and provide straight reference lines that are picked up by 2 optical sensors (Digital CCD Optical Position Sensors, DCOPS) placed at each CSC chamber. The Φ coordinate alignment is handled by optical SLMs and transfer lines. Transfer lines run parallel to the CMS Z-axis along the outer cylinder envelope of CMS at 6 points separated 60° in Φ . Transfer lines allow connecting optically the full barrel and endcap muon structures.

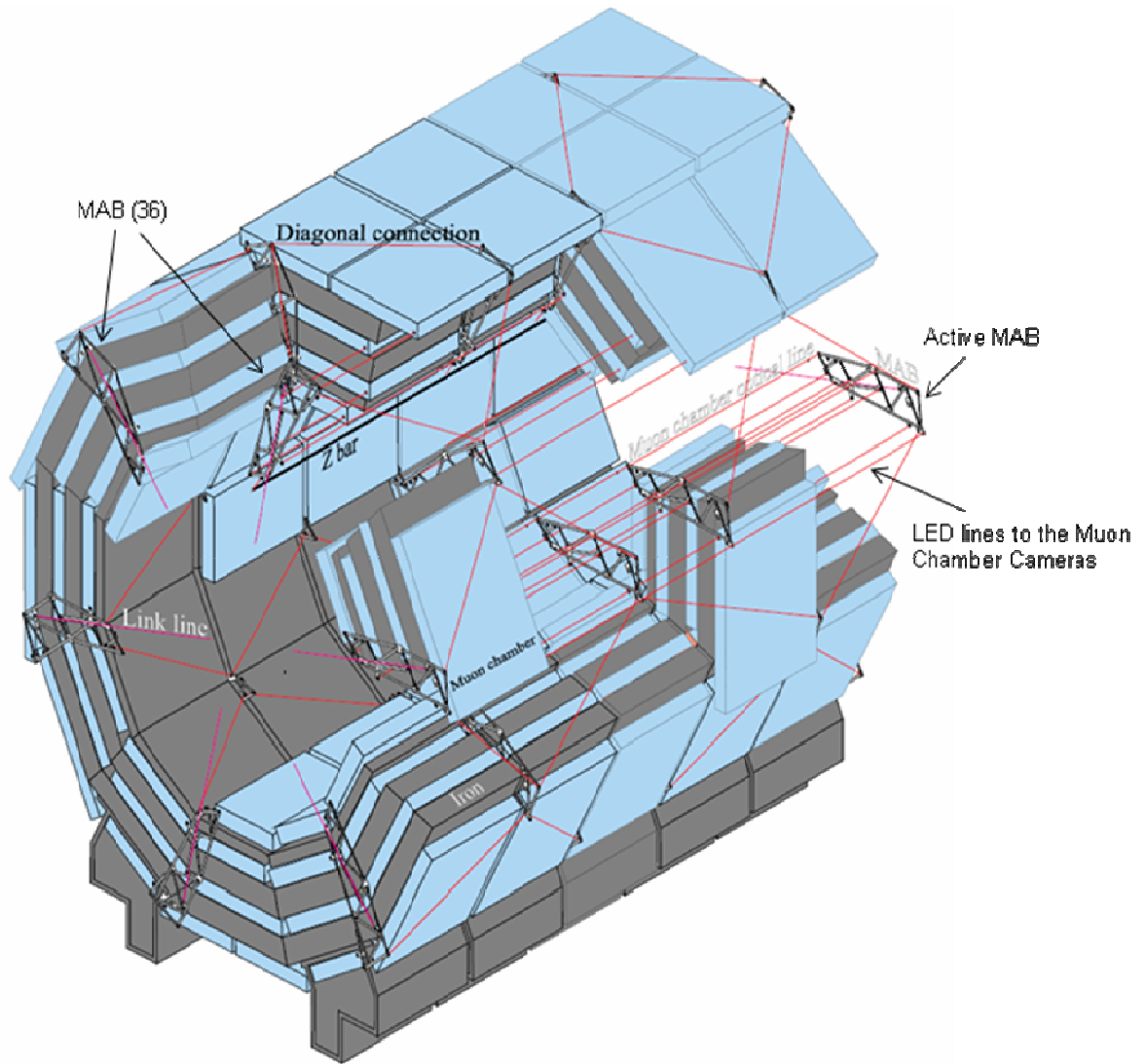
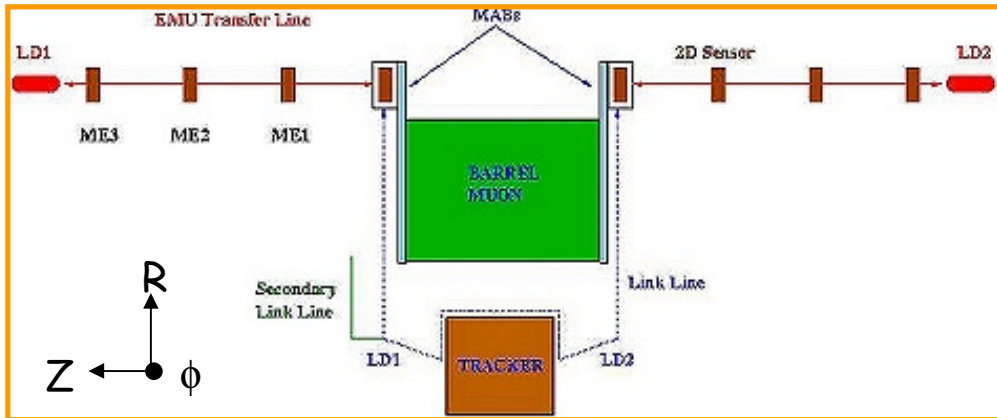


Fig. 6: The barrel muon alignment system.

a)



b)

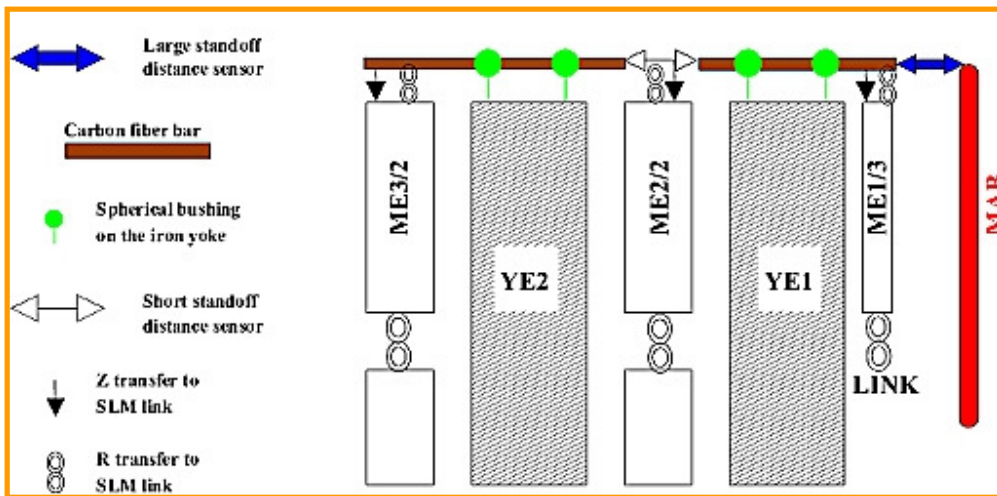


Fig. 7: The Endcap Alignment System.

2.4 The Link Alignment System

The purpose of the Link Alignment System is to measure the relative positions of the muon spectrometer and the tracker body in a common CMS coordinate system. It is designed to work in a challenging environment of very high radiation and magnetic fields; meet tight space constraints, and provides high precision measurements over long distances.

A distributed network of Amorphous Silicon Position Sensors (ASPDs) placed around the muon spectrometer and tracker volumes are connected by laser lines. An ASPD sensor [9,11] consists of two groups of 64 silicon micro-strips, with a pitch of 430 μm , oriented perpendicularly. The intrinsic sensor position resolution is better than 5 μm . The centring of the sensor in its mechanical mount was measured with 3D and 2D coordinate measuring machines with a precision in the range 5-10 μm .

The entire Link System is divided into three Φ planes 60° apart starting at $\Phi = 15^\circ$. Each plane consists of four independent quadrants, resulting in 12 laser paths, or lines: 6 on each side (positive or negative Z) of the CMS detector. Fig. 8 shows a sketch of a quarter of Φ plane with its instrumentation. The three laser light paths, originated at three different regions, Tracker, EndCap, and Barrel, are also indicated in Fig. 8. All laser sources-collimators are housed in carbon fibre structures called ARs (Alignment Rings), MABs, and LDs (Link Disks).

The AR's, rigid carbon fibre annular structures, are placed at both ends of the tracker as described in 2.1. The LD is suspended from the outer diameter of the YN/1 iron disk of the end-cap muon spectrometer by means of aluminium tubes attached to the mechanical assemblies called Transfer Plates (TP). MABs are mounted onto the barrel yoke as described in 2.2. Fig. 9 shows the AR and LD installed in CMS.

The ME/1/1 and ME/1/2 disks of chambers of the end-cap muon spectrometer are linked to the Tracker and the barrel muons via the laser paths and opto-mechanical sensors installed in the TPs and MABs.

The multiple lasers-ASPDs link measurement network is complemented by electrolytic tilt-meters (for angular measurements with respect to the gravity vector of the elements to which they are attached), proximity sensors (optical and mechanical, for short distances measurements), aluminium tubes for long distances measurements, magnetic probes and temperature sensors, which location in the detector is also shown in Fig. 8.

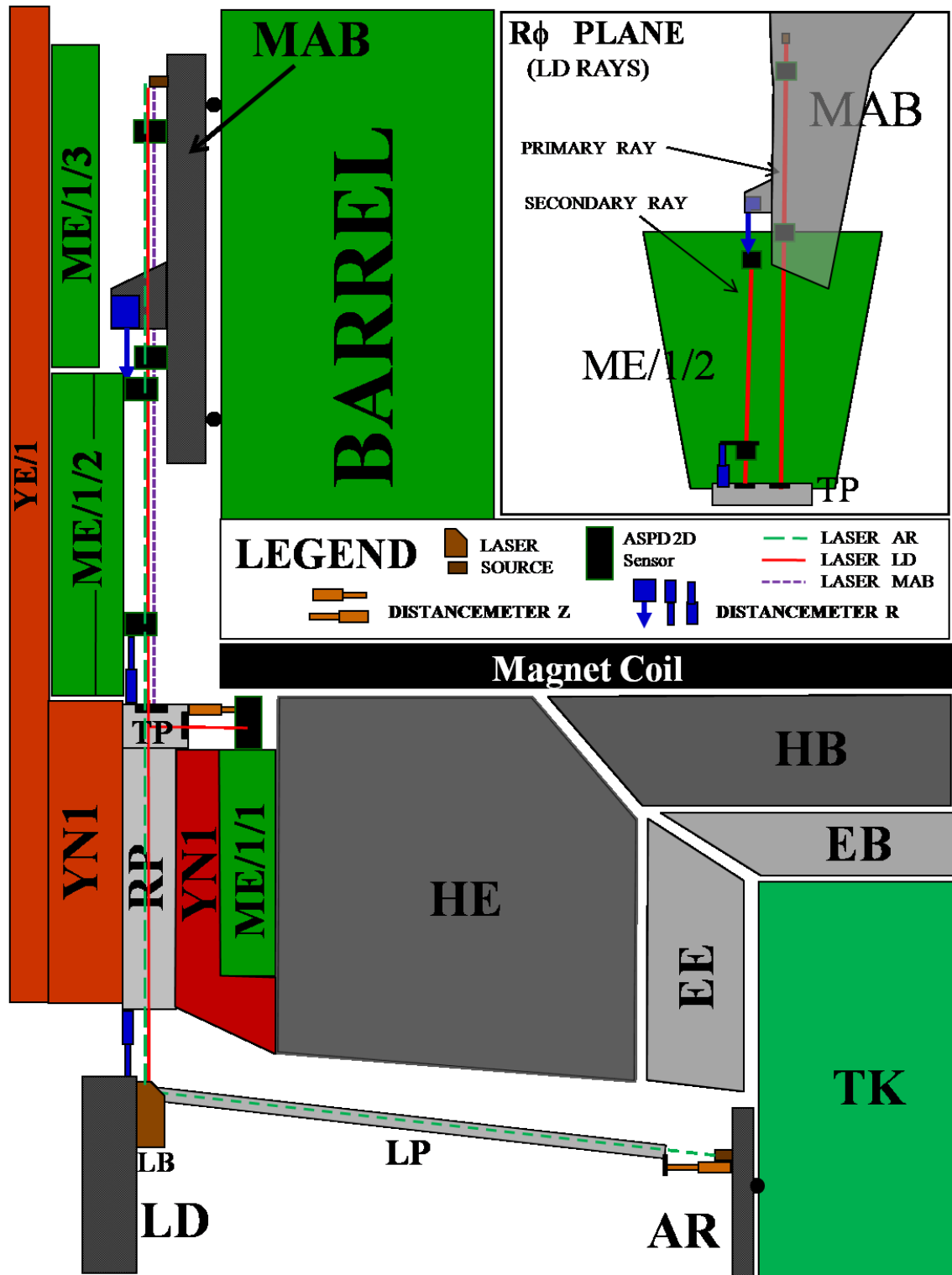


Figure 8: Link Alignment elements in a quarter of ϕ plane.

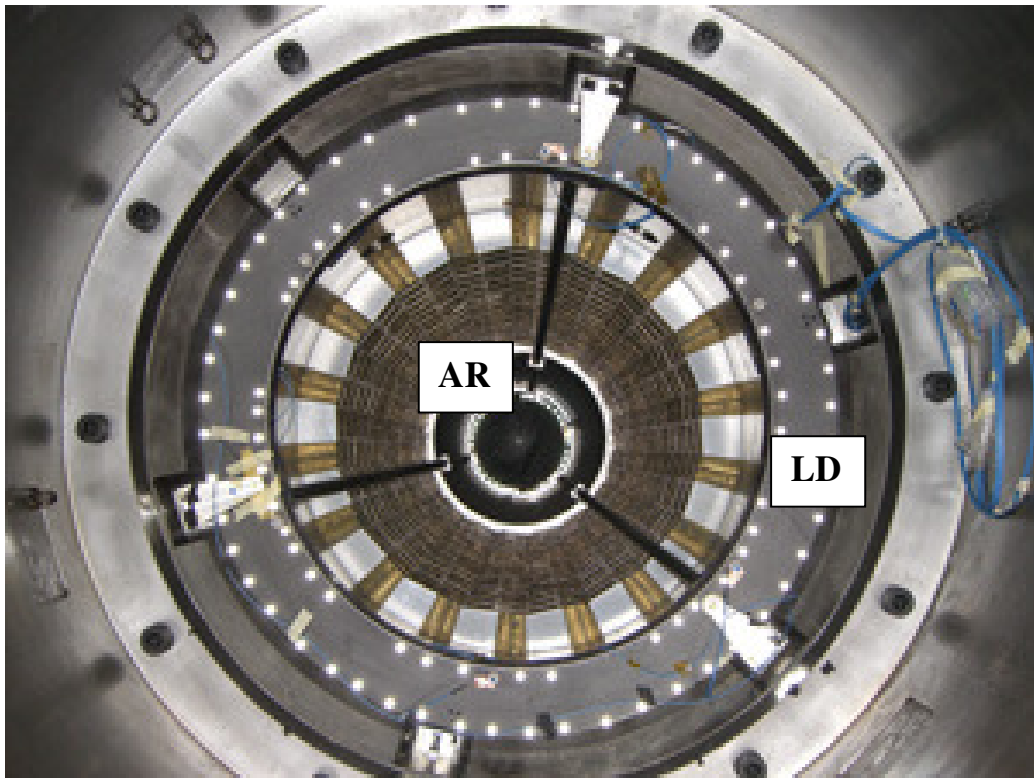


Fig. 9: Photograph of the Link Disk and the Alignment Ring as seen from the +Z CMS axis.

The monitoring of the relative displacements (along Z and $R\Phi$ directions) between some CMS elements, relevant for the system, is done with the help of aluminium bars (longitudinal and radial profiles, labelled LP and RP in Fig. 8) for long distances, and contact and non contact proximity sensors for short distances. Changes in length of the aluminium profiles due to temperature variations are controlled by the readout of the appropriate temperature probes.

A 3600 mm long LP relates LD and AR approximately in the region $\eta=3$. On its closest end to the AR a target is in contact with a potentiometer [12], located at the AR, allowing to monitor the relative distance between LD and AR structures along the CMS Z coordinate, at three different Φ positions. The other Z monitoring in a Φ quarter is the relative distance between the TP and the ME1/1 chamber. This is done also with a contact potentiometer installed in the TP, which rod touches a target situated on the top side of the ME1/1 chamber (see Fig 8).

The rest of the relative distance measurements between CMS elements, in a Φ quarter, monitor eventual motions in the $R\Phi$ direction. The longest monitored distance is the one between LD and TPs. A 1977 mm long radial profile (RP in Fig. 8), instrumented with a potentiometer in the closest end to the LD, measures the LD to TP relative distance. Relative displacements between the TP and the bottom side of the ME1/2 chamber are monitored as well using contact potentiometers. The $R\Phi$ relative distance between the MAB structure and the top side of the ME/1/2 chamber in the corresponding Φ quarter, is monitored with a non contact proximity device [13]. A sensor is installed at the bottom place of each MAB structure. The sensor emitting/receiving head directs a laser light and receives the reflected light to/from a target located on the top region of the ME/1/2 chamber. All proximity measurements along $R\Phi$ are labelled as Distancemeter R in Fig. 8.

Concerning measurement errors, the length of the longitudinal profiles are determined with an error smaller than 30 μm . The lengths of the various sensor mechanical supports are measured with a 3D measuring machine with a precision in the range 5 - 10 μm . The typical precision in the short-distances measurement with the contact and optical sensors used in the Link System stays, according with our bench calibrations [14], in the region 30 – 40 μm . However, the uncertainty in the spatial location of sensors related to the mounting in CMS is never smaller than 300 μm .

The estimated combined errors (mechanical support length plus proximity sensor output plus the mounting uncertainty) in the measurements of absolute positions, is about 305 μm . Nevertheless, the relative distances measurements are only affected by the precision of the proximity sensors, $\sim 40 \mu\text{m}$.

Complementing the laser and distance measurement system, all the alignment structures (ARs, BDs, LDs, TPs, and MABs) are instrumented with different models of tiltmeter sensors [15] which provide direct information on changes in orientations.

3. Some notes about the magnetic field forces and magnetic field map in CMS

Motions of CMS structures are mainly provoked by the magnetic field forces of the internal 4 T magnet solenoid. The field flux is almost contained in the yoke of the 12,000 ton experimental structure.

We say *mainly* because beside the field forces there are the effects due to frictions between metallic touching structures, large size pieces not fitting perfectly in the corresponding holes, etc. Note that the CMS is like an enormous puzzle assembled with very heavy pieces subject to the gravity forces. Therefore we do not expect easy open/close operations in the first years of operation.

The monitoring of the resulting motions of the CMS structure is, as already mentioned, the task of the Link Alignment System (with the final aim of giving at any moment the position of the Muon Chambers System with respect to the Tracker Body) through their optic-mechanical net of laser lines, photodetectors, long and short distance measuring devices, tilt sensors, etc. The data read-out from sensors allows the observations to be described in the chapters that follow.

Incidentally, we also said in the first paragraph that the field flux is *almost* contained in the yoke because, in fact, the lines extend in the axial and radial directions beyond the experiment contours as we will see.

Having all above in mind, let us start by saying that the 4 T solenoid induces an axial force on the endcap iron yoke (on both Z sides), in the direction of the centre of the solenoid, of about 10,000 ton, and therefore, the most important deformation of the structures is done on the endcap disks [16].

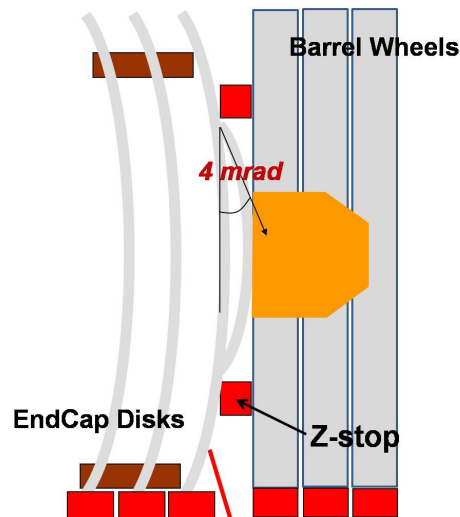


Fig. 10: Sketch of the deformation of the first endcap iron disk as a result of the compression due to the magnetic field forces and the resistance of the barrel Z-stops

The YN1 iron structure (both Z sides), from which the LDs hang (see Fig. 8), is pushed towards the IP by a force of about 6.5 kt. The various Z-stops, which prevent the disks from getting pushed into each other and crash onto the barrel wheels, make the endcap disks to bend into a cone shape (see sketch in Fig. 10). The resulting bending angle of the inner ring of the first encap iron, relative to the vertical, is of about 4 mrad.

The relationship between the current in the coils and the magnetic field strength was measured at the SX5 Hall during the magnet test. For currents in the range of 4000 – 19140 A, the relation was linear following the expression:

$$B \text{ (T)} = 0.00020988 \text{ T/A} \times I \text{ (A)} + 0.011 \text{ T},$$

at the CMS coordinates origin.

The calculation of the full magnetic field map is very complex and needs the use of various computer codes [16]. The numbers we quote hereafter come from the CMS Field Map release of July 2009, for $\mathbf{B}(0, 0, 0) = 3.811 \text{ T}$.

3.1 Magnetic field intensities at the Link Alignment sensitive locations

From the above mentioned CMS Field Map release we have extracted the expected magnetic field strengths at some places close to the locations where the Link proximity or photodetector sensors are installed. We have chosen quotations in the $Y > 0, Z > 0$ quadrant at the $X = 0$ CMS plane, therefore Y_{CMS} is identical to R_{CMS} and B_y translates into B_R . The summary of expectations is given in Table 1. Figs. 1 and 8 help in finding the geometrical coordinates used in the Table.

As shown, and in agreement with the above quoted calculated forces, the zones of maximum intensity are those in the neighborhood of the $\eta = 3$ in the Tracker region, where the proximity sensors monitoring the LD – AR distances are placed and the YN1 region where are sitting the Link System proximity sensors measuring the LD – YN1 distances. The zones at the Transfer Plates locations have also not negligible ($> 1 \text{ T}$) field intensities. The operation of the Link System proximity sensors is not affected by the magnetic field, but the quoted numbers will explain some of the observed motions of the related structures.

Finally, in the MAB regions, where ASPD sensors are placed, the field is in the order of 0.5 T, that cannot affect the light spot spatial reconstruction resolutions [11].

X (mm) B_X (T)	Y (mm) $B_Y \equiv B_R$ (T)	Z (mm) B_Z (T)	Location & Sensor
0.	260.	2900.	TK bottom; proximity LD-AR
0.0002	0.016	3.643	
0.	600.	6660.	YN1; proximity LD-YN1
0.0002	0.502	1.498	
0.	2800.	6660.	YN1; Transfer Plate & ASPD
0.00007	0.692	1.077	
0.	1180.	6660.	YN1; proximity LD-YN1
0.0006	0.525	3.098	
0.	2700.	6660.	Transfer Plate; proximity TP-ME/1/1
0.0001	0.640	1.019	
0.	2860.	6660.	Transfer Plate, proximity TP-ME/1/2
0.00004	0.734	1.092	
0.	4500.	6660.	MAB; proximity MAB-ME/1/2
0.004	0.616	-0.222	
0.	4500.	6660.	MAB; ASPD at MAB bottom
0.004	0.616	-0.222	
0.	6500.	6660.	MAB; ASPD at MAB top
0.001	0.019	-0.464	

Table 1: *Expected magnetic field strengths at some places close to the locations where Link proximity or photodetector sensors are placed.*

3.2 Direct measurement of the magnetic field intensity with Hall probes

The Link Alignment System includes, among their sensors, Hall magnetic probes (MP) at some specific places for a direct measurement of the field intensity in air. A pair of MPs is installed on top of each of the twenty two electrolytic clinometers used for the angular monitoring (Sec. 8). The MPs, on a tiltmeter, are spaced about 2.5 cm which is the distance between the two excitation electrodes of the tilt sensor.

The MPs belongs to the model 2D-VH-11, integrated 2-axis Hall element, $1 \text{ V} = 2.0770 \text{ T}$ [17]. It measures the field in two perpendicular directions (see Fig. 11) and they are placed such that one of the directions coincides with the CMS B_z . Since on top of tiltmeter sensors, the Hall probes are placed in a plane parallel to the CMS X-Z plane, the second component is measuring B_x , related to B_r by $B_x = B_r \times \cos\Phi$.

The idea of installing two MPs on top of each tiltmeter was to be able to measure the field gradient between the two excitation electrodes, $G = B_z(\text{MP1}) - B_z(\text{MP2})$ to eventually correct the tiltmeter output voltage [18]. Finally, the observation said that the two B_z readout measurements are compatible among them and therefore the electrolytic clinometers output voltages are insensible to the field lines crossing them perpendicular to the long sensor axis.

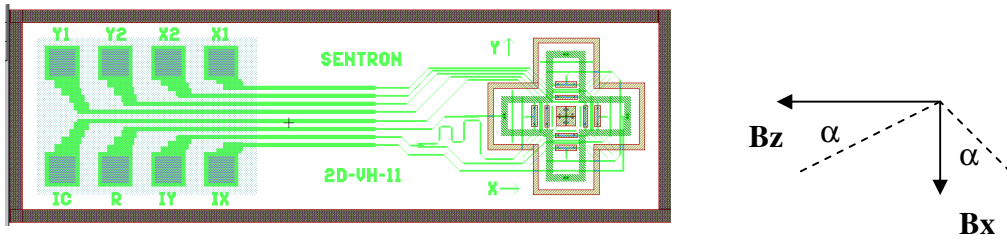


Fig. 11: The SENTRON AG 2D-VH-11 magnet probe topology and the sensitive directions (CMS coordinates) on tiltmeters tops. The angle α indicates an eventual misalignment (rotation) during the installation on top of the corresponding tiltmeter. We can do the positioning with a precision better than 3° .

Since all the MPs were installed for underground runs, we have used them to compare their measurements with the CMS Field Map expectations. We have done that using the 3.8 T underground CRAFT09 data taken on August 27th, 2009 (867 events recorded, 1 evt./5 min, current in the coils $I = 18160 \text{ A}$, providing a field intensity of $B = 3.813 \text{ T}$) and the mentioned Map at $B = 3.811 \text{ T}$.

Comparisons are given in Tables 2 a) to v). Each Table corresponds to the MPs placed on top of a given tiltmeter. Since the two MPs in the same clinometer give compatible measurements we quote in the tables the average of the two numbers. Errors on the readout values are statistical and systematic added in quadrature. Systematic error in the readout voltage of the MPs is about 5%.

Note that the Bz measurement of the MPs placed on top of the tiltmeters located at AR+ (Top and Bottom) and the ones at BD+ (Top and Bottom) were saturating as from B = 3.0 T and there is no quotation for them.

Each Table 2 gives the following information:

First row: spatial CMS (X, Y, Z) coordinates of the geometrical center of the set (MP1, MP2) in mm.

Second row: expected Bx, By and Bz, in mT, as extracted from the CMS magnetic field map.

Third row: average measurement, with errors as explained above, of Bx and Bz, in mT. The Table caption includes the MPs locations in the CMS Z-side and Φ coordinate and the agreement/disagreement calculation, in terms of number of statistical deviations, between the measured Bz and the expected one. CMS magnetic field map values are assumed quantities without error.

(X, Y, Z) (mm)	-46	260	2934
(Bx, By, Bz) (mT)	-3	17	3638
(Bx, -, Bz) (mT)	-30 ± 4	-	-

Table 2 a): *Expected and measured magnetic field strengths at AR+ Top.*

Nominal $\Phi = 90^\circ$.

(X, Y, Z) (mm)	46	-260	2934
(Bx, By, Bz) (mT)	3	-17	3638
(Bx, -, Bz) (mT)	41 ± 4	-	-

Table 2 b): *Expected and measured magnetic field strengths at AR+ Bottom.*

Nominal $\Phi = 270^\circ$.

(X, Y, Z) (mm)	-46	260	-2934
(Bx, By, Bz) (mT)	3	-17	3634
(Bx, -, Bz) (mT)	38 ± 6	-	3688 ± 130

Table 2 c): *Expected and measured magnetic field strengths at AR- Top.*

Nominal $\Phi = 90^\circ$. Degree of agreement in Bz 0.4 σ .

(X, Y, Z) (mm)	46	-260	-2934
(B _x , B _y , B _z) (mT)	-3	17	3634
(B _x , -, B _z) (mT)	45 ± 6	-	3727 ± 132

Table 2 d): Expected and measured magnetic field strengths at AR– Bottom.

Nominal $\Phi = 270^\circ$. Degree of agreement in B_z 0.7 σ .

(X, Y, Z) (mm)	0	804	2789
(B _x , B _y , B _z) (mT)	0	50	3660
(B _x , -, B _z) (mT)	47 ± 10	-	-

Table 2 e): Expected and measured magnetic field strengths at BD+ Top.

Nominal $\Phi = 90^\circ$.

(X, Y, Z) (mm)	0	804	2789
(B _x , B _y , B _z) (mT)	0	50	3660
(B _x , -, B _z) (mT)	43 ± 10	-	-

Table 2 f): Expected and measured magnetic field strengths at BD+ Bottom.

Nominal $\Phi = 270^\circ$.

(X, Y, Z) (mm)	0	804	-2789
(B _x , B _y , B _z) (mT)	0	-51	3656
(B _x , -, B _z) (mT)	11 ± 10	-	3693 ± 149

Table 2 g): Expected and measured magnetic field strengths at BD– Top. Nominal $\Phi = 90^\circ$. Degree of agreement in B_z 0.3 σ .

(X, Y, Z) (mm)	0	-780	-2789
(B _x , B _y , B _z) (mT)	0	49	3656
(B _x , -, B _z) (mT)	15 ± 10		3672 ± 130

Table 2 h): Expected and measured magnetic field strengths at BD– Bottom.

Nominal $\Phi = 270^\circ$. Degree of agreement in B_z 0.1 σ .

(X, Y, Z) (mm)	30	550	6650
(B _x , B _y , B _z) (mT)	25	462	1516
(B _x , -, B _z) (mT)	70 ± 8	-	1525 ± 54

Table 2 i): Expected and measured magnetic field strengths at LD+. Nominal $\Phi = 90^\circ$. Degree of agreement in B_z 0.2 σ .

(X, Y, Z) (mm)	24	547	-6644
(B _x , B _y , B _z) (mT)	-20	-459	1520
(B _x , -, B _z) (mT)	-10 ± 4	-	1542 ± 54

Table 2 j): Expected and measured magnetic field strengths at LD-. Nominal $\Phi = 90^\circ$. Degree of agreement in B_z 0.4 σ .

(X, Y, Z) (mm)	6864	1809	6654
(B _x , B _y , B _z) (mT)	-2	-1	-415
(B _x , -, B _z) (mT)	-17 ± 4	-	-372 ± 13

Table 2 k): Expected and measured magnetic field strengths in MAB at Z+, $\Phi = 15^\circ$. Degree of agreement in B_z 3.3 σ .

(X, Y, Z) (mm)	6864	1809	-6654
(B _x , B _y , B _z) (mT)	2	1	-414
(B _x , -, B _z) (mT)	9 ± 4	-	-373 ± 13

Table 2 l): Expected and measured magnetic field strengths in MAB at Z-, $\Phi = 15^\circ$. Degree of agreement in B_z 3.1 σ .

(X, Y, Z) (mm)	1882	6858	6654
(B _x , B _y , B _z) (mT)	-1	-3	-416
(B _x , -, B _z) (mT)	-2 ± 2		-396 ± 14

Table 2 m): Expected and measured magnetic field strengths in MAB at Z+, $\Phi = 75^\circ$. Degree of agreement in B_z 1.4 σ .

(X, Y, Z) (mm)	1882	6858	-6654
(B _x , B _y , B _z) (mT)	1	3	-414
(B _x , -, B _z) (mT)	10 ± 10	-	-396 ± 14

Table 2 n): Expected and measured magnetic field strengths in MAB at Z-, $\Phi = 75^\circ$. Degree of agreement in B_z 1.3 σ .

(X, Y, Z) (mm)	-4982	5068	6654
(B _x , B _y , B _z) (mT)	2	-2	-416
(B _x , -, B _z) (mT)	10 ± 2		-392 ± 14

Table 2 o): Expected and measured magnetic field strengths in MAB at Z+, $\Phi = 135^\circ$. Degree of agreement in B_z 1.7 σ .

(X, Y, Z) (mm)	-4982	5068	-6654
(B _x , B _y , B _z) (mT)	-2	2	-414
(B _⊥ , B _z) (mT) (# σ)	-6 ± 8	-	-387 ± 17

Table 2 p): Expected and measured magnetic field strengths in MAB at Z-, $\Phi = 135^\circ$. Degree of agreement in B_z 1.4 σ .

(X, Y, Z) (mm)	-6864	-1771	6654
(B _x , B _y , B _z) (mT)	2	1	-416
(B _x , -, B _z) (mT)	9 ± 2	-	-400 ± 14

Table 2 q): Expected and measured magnetic field strengths in MAB at Z+, $\Phi = 195^\circ$. Degree of agreement in B_z 1.1 σ .

(X, Y, Z) (mm)	-6864	-1771	-6654
(B _x , B _y , B _z) (mT)	-2	-1	-414
(B _x , -, B _z) (mT)	-13 ± 2		-367 ± 13

Table 2 r): Expected and measured magnetic field strengths in MAB at Z-, $\Phi = 195^\circ$. Degree of agreement in B_z 3.6 σ .

(X, Y, Z) (mm)	-1882	-6820	6654
(B _x , B _y , B _z) (mT)	-3	21	-517
(B _x , -, B _z) (mT)	-20 ± 6	-	-404 ± 14

Table 2 s): Expected and measured magnetic field strengths in MAB at Z+, $\Phi = 255^\circ$. Degree of agreement in B_z 8.1 σ .

(X, Y, Z) (mm)	-1882	-6820	-6654
(Bx, By, Bz) (mT)	3	21	-515
(Bx, -, Bz) (mT)	12 ± 2	-	-359 ± 13

Table 2 t): Expected and measured magnetic field strengths in MAB at Z-, $\Phi = 255^\circ$. Degree of agreement in Bz 10.4 σ .

(X, Y, Z) (mm)	4982	-5030	6654
(Bx, By, Bz) (mT)	-1	-1	-406
(Bx, -, Bz) (mT)	-1 ± 2	-	-367 ± 13

Table 2 u): Expected and measured magnetic field strengths in MAB at Z+, $\Phi = 315^\circ$. Degree of agreement in Bz 3.0 σ .

(X, Y, Z) (mm)	4982	-5030	-6654
(Bx, By, Bz) (mT)	1	1	-405
(Bx, -, Bz) (mT)	12 ± 2	-	-380 ± 14

Table 2 v): Expected and measured magnetic field strengths in MAB at Z-, $\Phi = 315^\circ$. Degree of agreement in Bz 1.8 σ .

Inspection of Tables 2 a) to j), referred to the central CMS volume, shows a perfect agreement (less than 1 σ) between the magnet probes Bz field measurements and the expectations from the CMS magnetic field map.

Concerning the comparison between measurements and expectations at the MABs positions (all of the MPs are at R ~ 7 m and Z = ± 6.654 m), inspection of Tables 2 k) to v) shows, in general, disagreement between the two quantities at both Z CMS sides: the field intensity extracted from the CMS field map is always larger than the readout MPs values.

The disagreement exceeds the 3 σ for (Z side, Φ angle) +/- 15°, - 195°, +/- 255° and + 315°. For the above R, Z and Φ coordinates the ratio, for the Bz quotations:

$$O = \Sigma(\text{Field map values}) / \Sigma(\text{MP measured values}) = 1.19$$

Therefore, at those 6 locations the overestimation given by the CMS field map is, in average, of the order of 19%. The eventual miss orientation of the MPs tandem to account for the corresponding underestimation would be of $\alpha \approx 32.8^\circ$, which is far from being credible.

In the remaining 6 MABs positions, +/- 75°, +/- 135°, + 195° and - 315°, the disagreement is smaller than 2 σ , the value of the ratio is O = 1.06 and the corresponding overestimation is about 6%. An eventual miss orientation of the MPs of $\alpha \approx 19.4^\circ$, would afford for this discrepancy but is still far away from the precision we can reach.

4. The CMS Alignment System elements installed on ground for the Magnet Test and under ground for CRAFT

Fig. 12 sketches the elements of the CMS Alignment System operational during the test of the CMS Magnet. The system consisted of three Link System quarters of Φ planes (75° , 255° and 315°) in the positive side of the detector; the full positive Endcap Alignment System, and the full instrumentation of two bottom barrel sectors (Sectors 10 and 11) of the Barrel Alignment System.

During the first part (Phase I) of the Magnet Test a mock-up of the Tracker was installed, allowing the installation of the AR, to perform full alignment measurements. Both elements, the Tracker mock-up and the AR were removed for the second part of the test (Phase II) in order to carry out a precise filed mapping inside the solenoid.

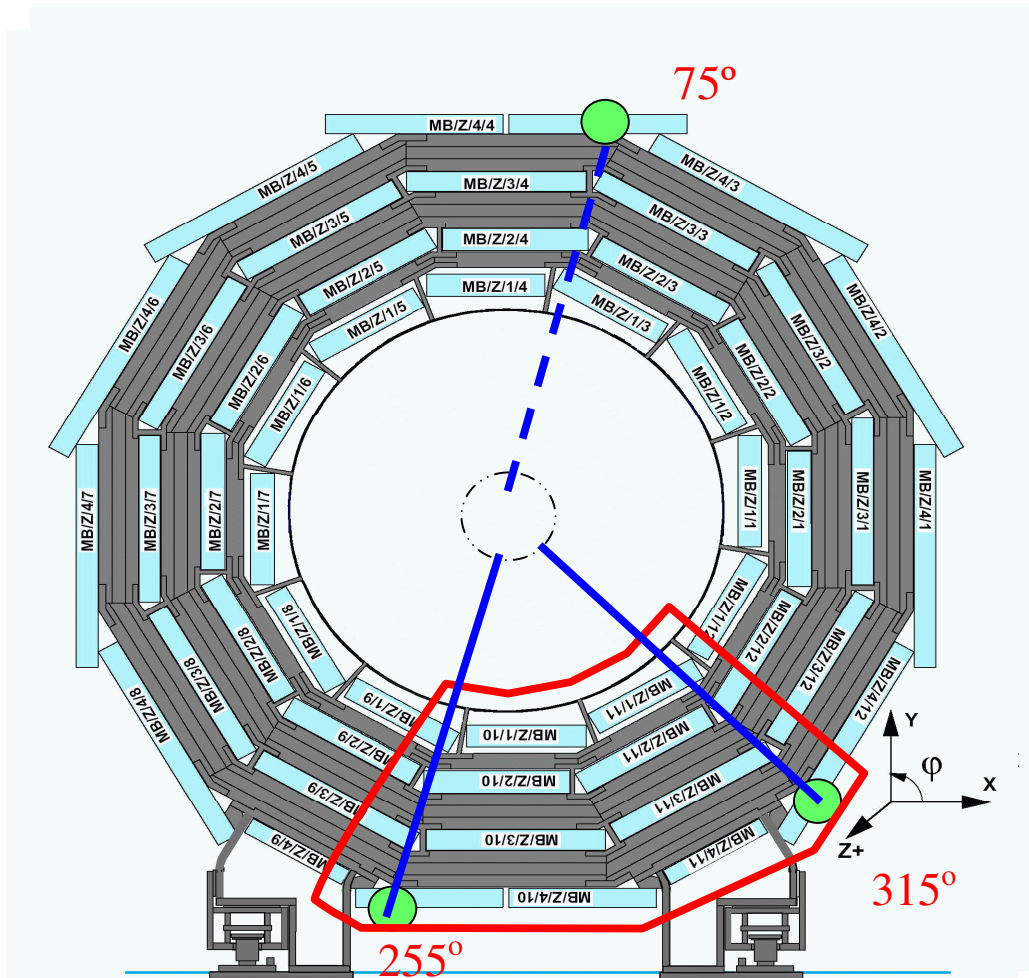


Fig. 12: Transverse view of the muon barrel system with indication of the installed elements for the Magnet Test.

Before placing the CMS experiment in P5, one hundred meters underground, we installed the full Link Alignment System as described in subsection 2.4.

All components, carbon fibre structures and all type of sensors were calibrated, previous to their installation, on specific benches, with precisions in the tenths of μm for lengths and tenths of μrad for angular orientations.

In addition and during installation, survey and photogrammetry of components were done with precisions in the 50 – 300 μm for spatial positions.

5. Data Acquisition and Detector Control Systems

The DAQ and detector control systems are integrated into the DCS (Detector Control System) environment. The standard slow control software adopted by CMS is PVSS, used within a framework called JCOP (Joint Controls Project) which provides a set of guidelines, conventions and common software tools. Hardware devices and sensors are controlled and readout through specialized electronics which communicate with PVSS via the OPC (OLE –Object Linking and Embedding-- for Process Control) or DIM (Discrete Information Management) protocols.

All sensors except the photosensors are controlled through standard ELMB (Embedded Local Monitor Board) cards, for which tools exist within the JCOP Framework for the creation of PVSS data structures which allow easy access and control. ASPDs are readout and controlled by custom dedicated electronic cards which are not contemplated in the JCOP Framework. Data structures and PVSS panels are therefore developed specifically for these cards. Fig. 13 shows, as an illustration, three different PVSS panels, one is the general control panel and the other two show the monitoring of an ASPD 2D sensor and different 1D sensors in a line.

An FSM (Finite State Machine) tool provided in the JCOP Framework facilitates the construction of a hierarchical tree of devices (Device Units) and logical partitions (Control Units) which allow to control and configure the hardware and to coordinate the traffic of commands, states and alarms between different nodes. It automatically controls the different partitions, states and alarms of each subsystem and allows enabling or disabling any part of the system.

Data taking is not limited to passive recording. Different sequences and reading cycles can be performed for each device by complementing the FSM tree with a PVSS script which coordinates the reading sequences and checks the state of each device. This can also be done through an external script, using Java, to communicate with PVSS via DIM.

Data are recorded in an on-line Oracle database through the use of the RDB (Relational Database) Manager provided by PVSS. The data are subsequently organized and written into Root *n-tuples* by specialized online scripts which perform database queries, apply calibrations and construct full events for each subsystem. These root files are then transferred from the private online domain to the Tier-0 and the CAF (offline) by means of the CMS Storage Manager, essentially following the same path as CMS event data, to be used as input to COCOA for offline geometry reconstruction.

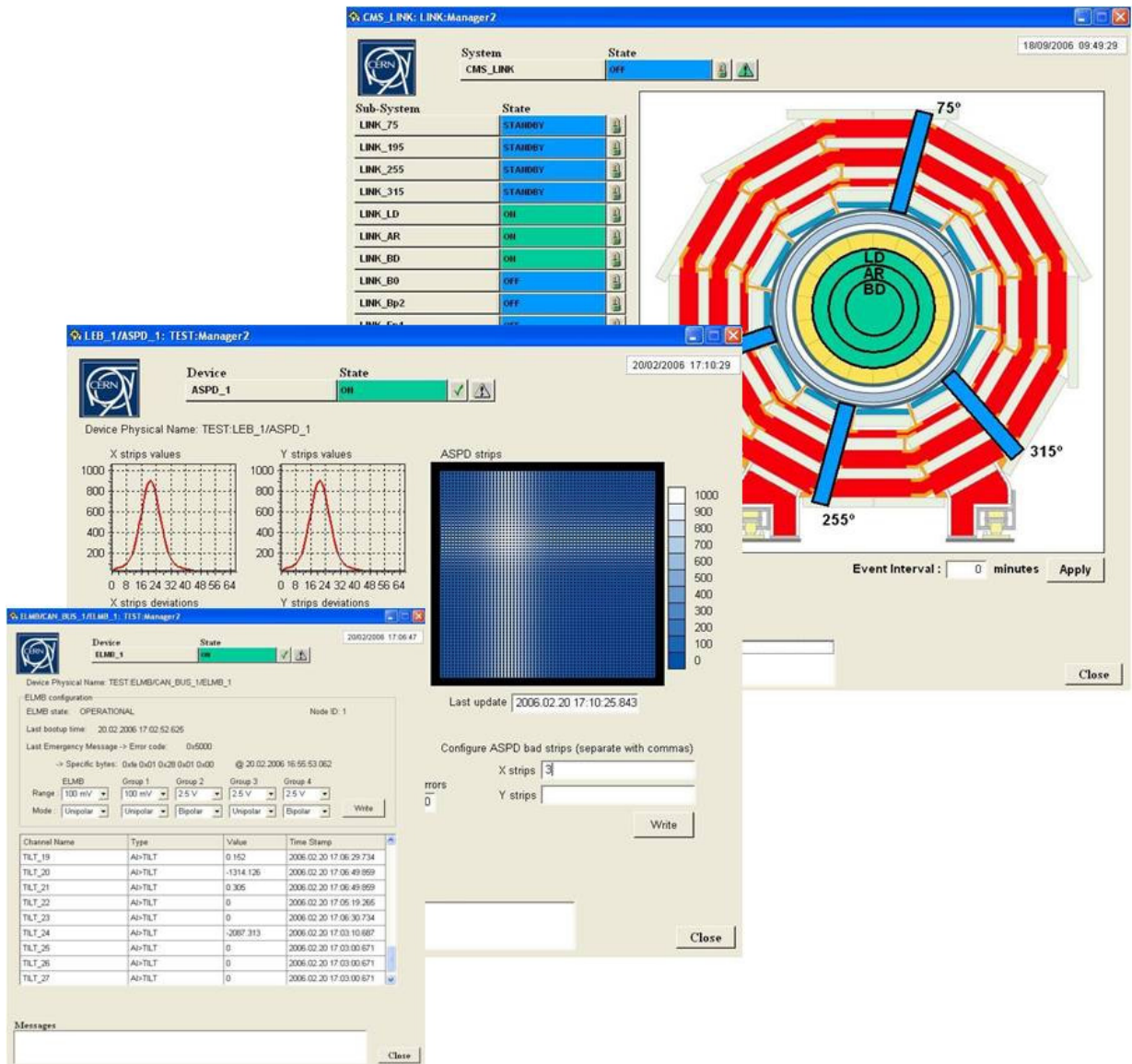


Fig. 13: Illustration of the PVSS monitoring panels.

6. Selecting data sets for analysis and comparisons

The inexistence of pure elastic motions shows the difficulty of making any accurate prediction based on previous motion behaviours. The lack of motion reproducibility will be, as said somewhere else [19], a constant during CMS operation.

Data from the Link Alignment system were recorded in continuous mode during the two Phases of the MT and during the underground CRAFT08 and CRAFT09 runs. In the three sections that follow (7 to 9) we analyze the data quality of the different source of measurements provided by the system, performing comparisons between the various measurement types, and the two phases of the MT and CRAFT runs. The coherence of the results and reproducibility of the observed measurements will be discussed.

For the study we will use three runs: for MT Phase I we will use the data corresponding to Fig. 14 a), for Phase II the data corresponding to Fig. 15 a) and for CRAFT the data corresponding to Fig. 16 a). Plots accompanying figures a) are illustrations of observed motions during the selected runs. In Fig. 14 the motions represented are the relative radial distances measured between the TPs and the ME/1/2 chambers, while in Figs. 15 and 16 the relative axial distances between TPs and ME/1/1 chambers are used as illustrations. Distances are given in mm with respect to the first data in the respective run at $B = 0T$.

The analysis of the recorded data from each sensor will concern to: 1) study of “recoveries”, whether or not the CMS elements retrieve the initial positions after switching off the magnet; 2) study of maximum displacements; 3) study, when possible, phenomenological descriptions of the monitored movements as a function of the magnetic field strength.

For the study of motions as a function of B , in Phase I, we will use only the data collected in the range $B = 0T$ to $B = 3.8 T$, before the down to $3.2 T$, so, about the first 1600 events in Fig. 14 a). In Phase II we will use the first 14000 events in Fig. 15 a), so the first rump up from $B = 0T$ to $B = 4T$ and, for the CRAFT run we will use the first 103 events in Fig. 16, so up to the first data recorded at $B = 4T$.

Note that two different expressions are used to calculate the magnetic field intensity from the recorded current intensity in the coils.

$$B (T) = 0.00020988 T/A \times I (A) + 0.011 T \text{ is used for the MT runs and}$$

$$B (T) = 0.00020725 T/A \times I (A) + 0.031 T \text{ is used for the CRAFT run.}$$

When data from the same sensor is available on (MT) and under (CRAFT) ground, comparison of the various sets of results will be done. For the CRAFT run comparison will be made between observations at $+Z$ and $-Z$ CMS sides.

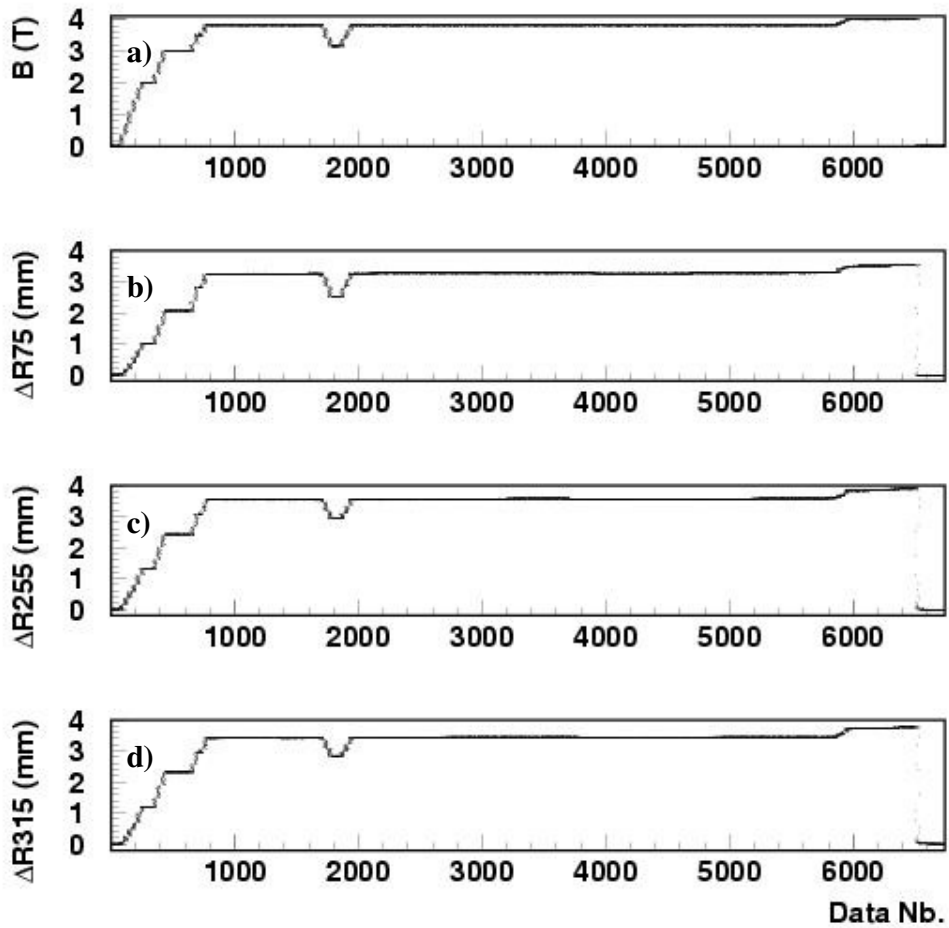


Fig. 14: From the last run in Phase I. a) Magnetic field intensity as a function of time (data number). b), c) and d) Relative distance between the TP and the ME/1/2 muon chamber in each of the three equipped quarters.

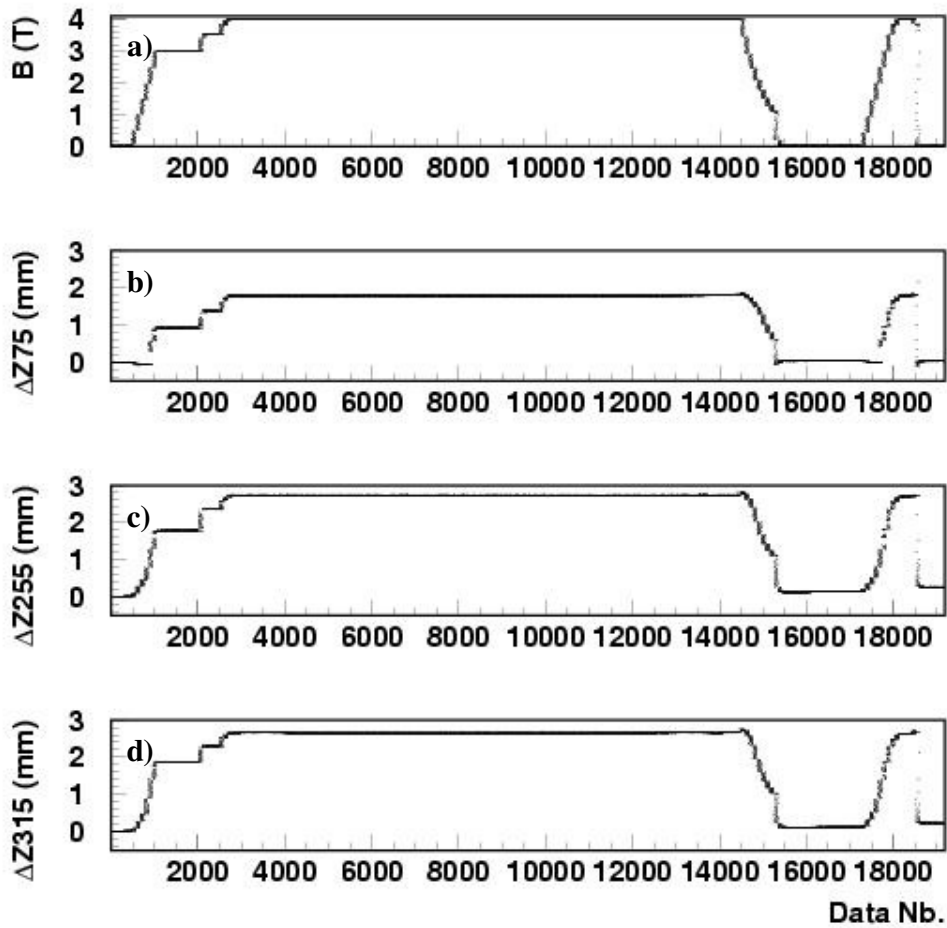


Fig. 15: From the last run in Phase II. a) Magnetic field intensity as a function of time (data number). b), c) and d) Relative distance between the TP and the ME/1/1 muon chamber in each of the three equipped quarters.

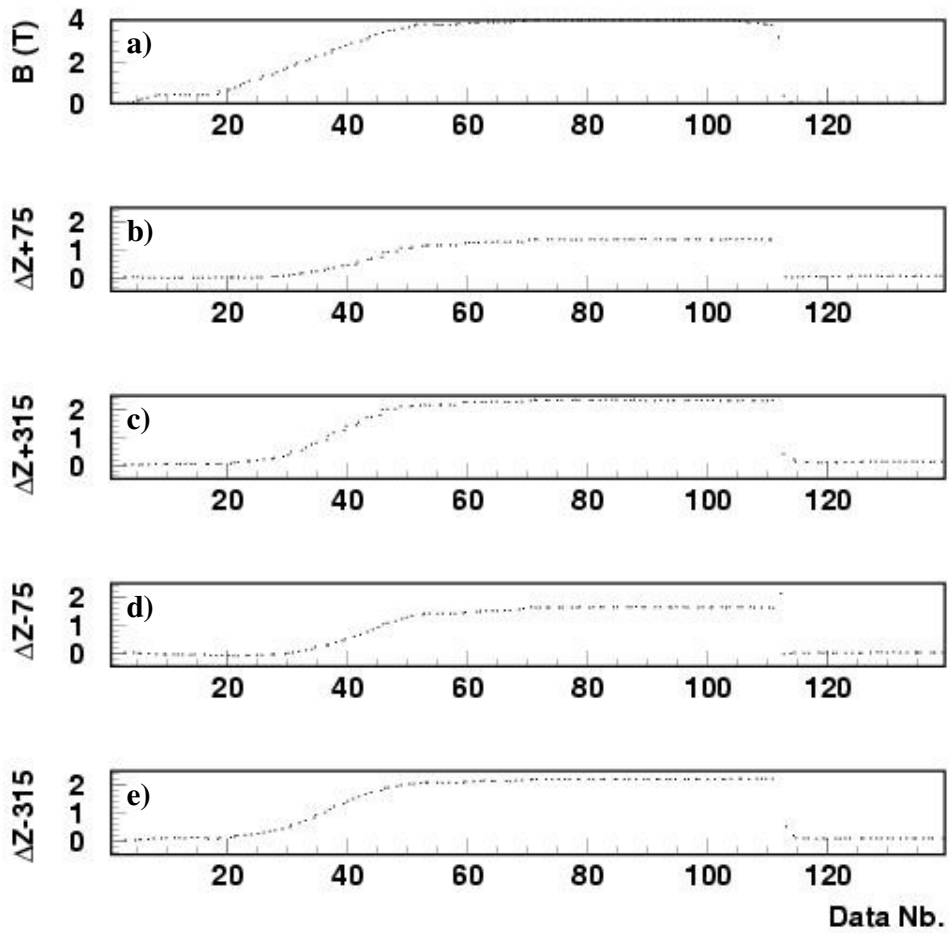


Fig. 16: From CRAFT run. a): Magnetic field intensity as a function of time (data number). b), c), d) and e): Relative distance between the TP and the ME/1/1 muon chamber in various quarters at +Z and -Z CMS sides.

7. Lasers system and photo-sensors information

During the MT the System reads-out the information provided by eight Amorphous Silicon Position Detectors (ASPDs), which monitor the five light paths originated by three lasers (collimators) in each of the three Φ quarters that are instrumented.

At the final CMS instrumentation of the twelve Φ quarters, only six ASPD are installed per quarter as it will be explained later in the text.

The ASPD 2D position detecting sensors [9, 10, 11, 20] installed in CMS for the Link System, are constructed following the sketch of Fig. 17 a). They consist of a layer of hydrogenated amorphous silicon carbon (a-Si_{0.9}C_{0.1}:H) of 195 nm thickness, sandwiched between two layers of 110 nm thick Al-doped zinc oxide (ZnO:Al) electrodes, perpendicularly segmented to form a semitransparent 2D matrix of 64 × 64 Schottky photodiodes. The zinc oxide contacts are segmented using photolithographic patterning. The ASPD layer stack is deposited onto a ~ 1 mm thick glass substrate.

In operation mode, a small fraction of the incident light of the positioning laser is absorbed in the a-SiC:H, thereby generating position dependent photocurrents on the strips. The photocurrent signals, extracted via Al bond pads on top of the ZnOAl strips, are multiplexed, converted to voltage and transferred to a dedicated electronics board. The position of a light spot on the sensor surface is then represented by the centre of gravity of the local photoresponses generated by the 2D matrix of photodiode pixels.

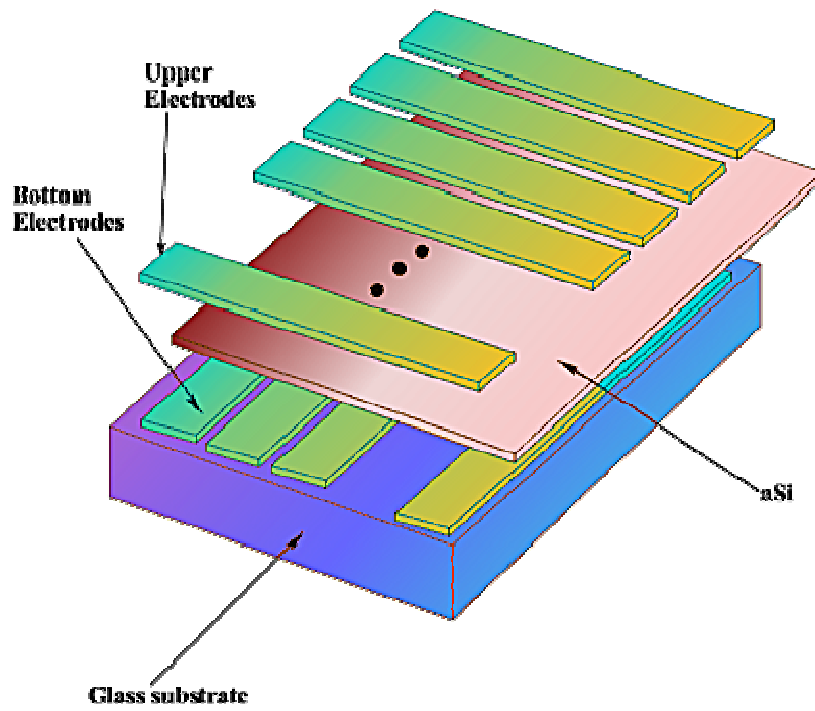
The most important parameters of the ASPD sensors are summarized in Table 3. In Fig. 17 b) we show the compact final configuration of an ASPD with its front end electronics. Total volume is $4.7 \times 4.7 \times 4.7 \text{ cm}^3$.

a-SiC:H thickness	295 nm
Strip thickness	110 nm
Glass thickness	1 mm
Active area	$28 \times 28 \text{ mm}^2$
Number of strips	64 horizontal + 64 vertical
Strip pitch	430 μm
Strip gap	22 μm

Table 3: *The ASPD construction parameters.*

The average characteristics of the sensors installed in the Link System Light Paths [21] are shown in Table 4. Quantities σ_x and σ_y represent the spatial point reconstruction precisions in the horizontal and vertical directions, respectively, while Θ_x and Θ_y stand for the two components of the deflection angle.

a)



b)

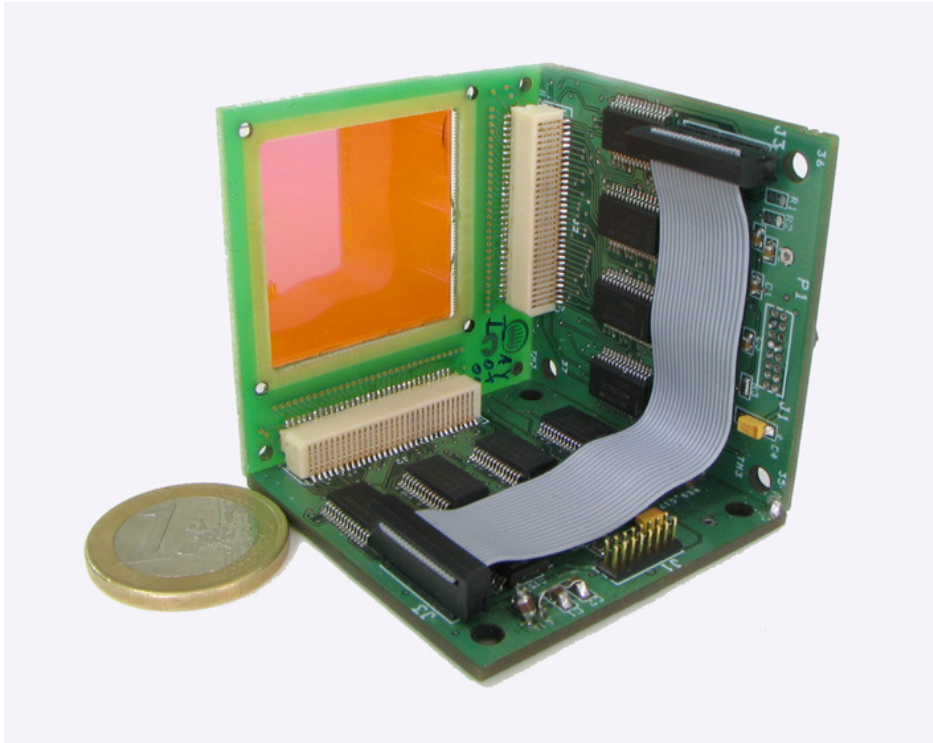


Fig. 17: Sketch of the geometry and photograph of the final configuration of an ASPD.

Sensitivity (mA/W)	16.3 ± 7.6
σ_x (μm)	5.2 ± 2.6
σ_y (μm)	5.1 ± 2.4
Θ_x (μrad)	-1.1 ± 5.1
Θ_y (μrad)	0.8 ± 3.8
Transmittance (%)	84.8 ± 2.9

Table 4: Average characteristics of the ASPD sensors for the CMS Alignment System.

The five mentioned light paths existing during the MT are originated by the three collimators installed in each of the Φ quarters, as sketched in Fig. 18. For the final network of Light Paths and intercepting ASPD sensors, units P7 and P8, due to technical reasons, were not installed. The missing information related to the position of the ME/1/1 chambers is provided by biaxial electrolytic clinometers and short distance measuring potentiometers. Light Path 3, in Fig. 18, is therefore inexistent in the CRAFT runs.

As an example, Light Path 1 starts at the collimator located at the Laser Box. The Laser Box (LB) is a small optical bench (see sketches in Fig. 19) containing the LD collimator, a modified rhomboidal prism that splits the laser beam into two parallel beams, about 4.5 cm apart from each other, and a transparent glass layer that allows the LD laser light passing through and to reflect the laser beam coming from the AR.

Let us detail now, for one quadrant (see Fig. 18), the data taking procedure. First, the laser from the AR turns on and the beam outgoing from the corresponding collimator (Light Path 5) arrives to the Laser Box mirror and it is deflected to the sensors P1 (placed on the Transfer Plate), P2 and P3 (both located in the MAB). Distances are: $d(\text{AR-LB}) = 3.682$ m, $d(\text{LB-P1}) = 2.151$ m, $d(\text{P1-P2}) = 1.654$ m, $d(\text{P2-P3}) = 2.538$ m. Total Light Path 5 length is then 10.025 m.

Second, the AR laser is switched off and the MAB laser is turned on. The corresponding collimator, installed in the MAB close to the 1D tiltmeter, sends a beam (Light Path 4) crossing in sequence the sensors P3, P2 and P1. Then the beam is deflected by the mirror in the direction of the AR, with no target. Distance between the collimator in the MAB and sensor P3 is 0.010 m..

Third, the MAB laser (located inside the Laser Level mounting) is switched off and the LD laser is turned on. The corresponding Laser Box collimator sends a beam that is splitted into two by the modified rhomboidal prism. One of the beams (light Path 1) crosses the sensors P1, P2 and P3, while the second one (parallel to the first) goes out in the direction of the TP.

At the TP, a splitter divides the incoming ray into two. One (Light Path 2) crosses sensors P4 (at the TP), P5 and P6 (both attached to the ME/1/2 camber), while the second one (Light Path 3, only existing at the MT runs, but not at CRAFT one as above mentioned) crosses sensors P7 (installed at the TP) and P8 (attached to the ME/1/1 chamber). Distances are: $d(\text{P4-P5}) = 0.067$ m, $d(\text{P5-P6}) = 1.736$ m and $d(\text{P7-P8}) = 0.050$ m.

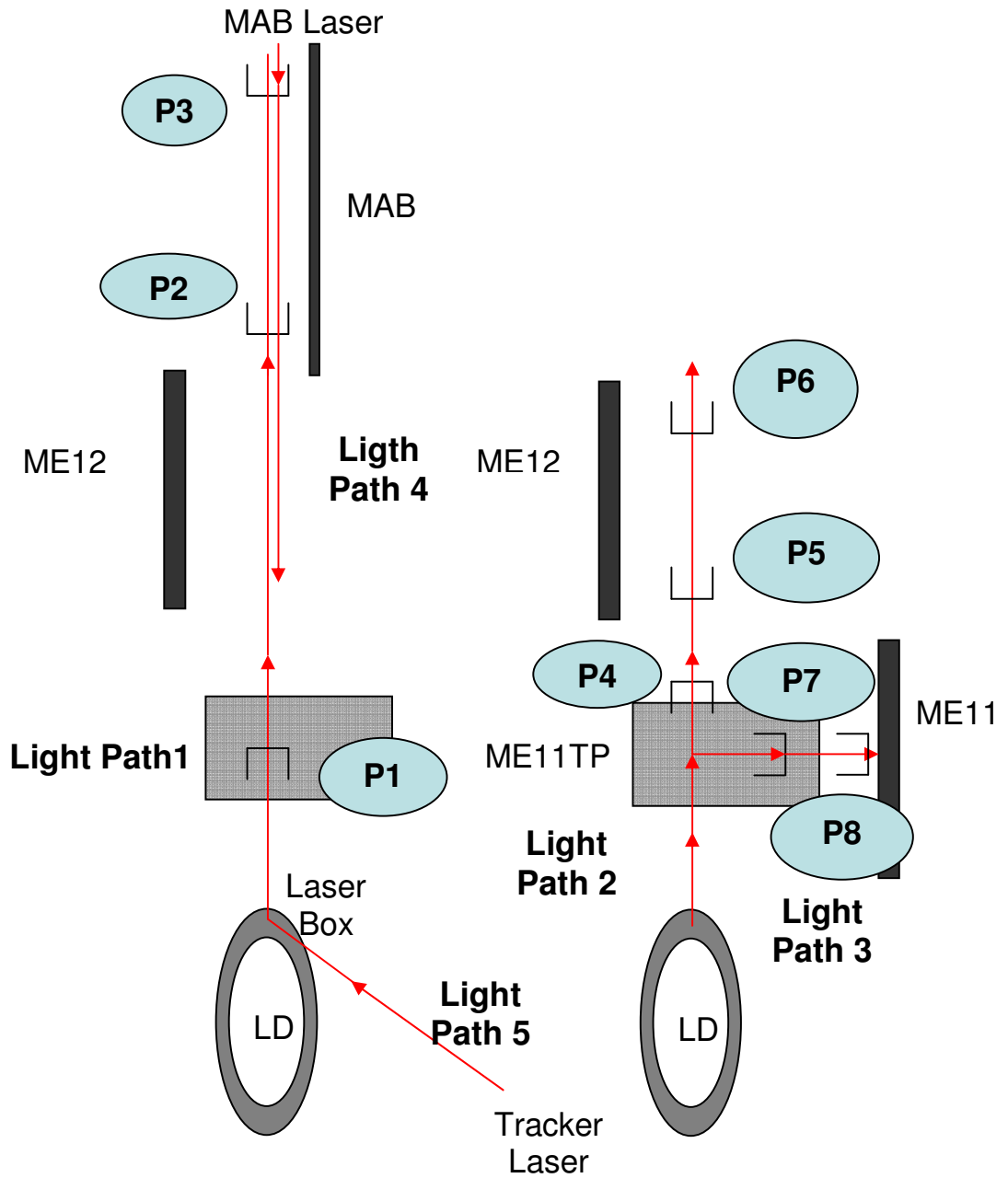


Fig. 18: The five light paths in a Φ quadrant during the Magnet Test. At underground Light Path 3 is not equipped.

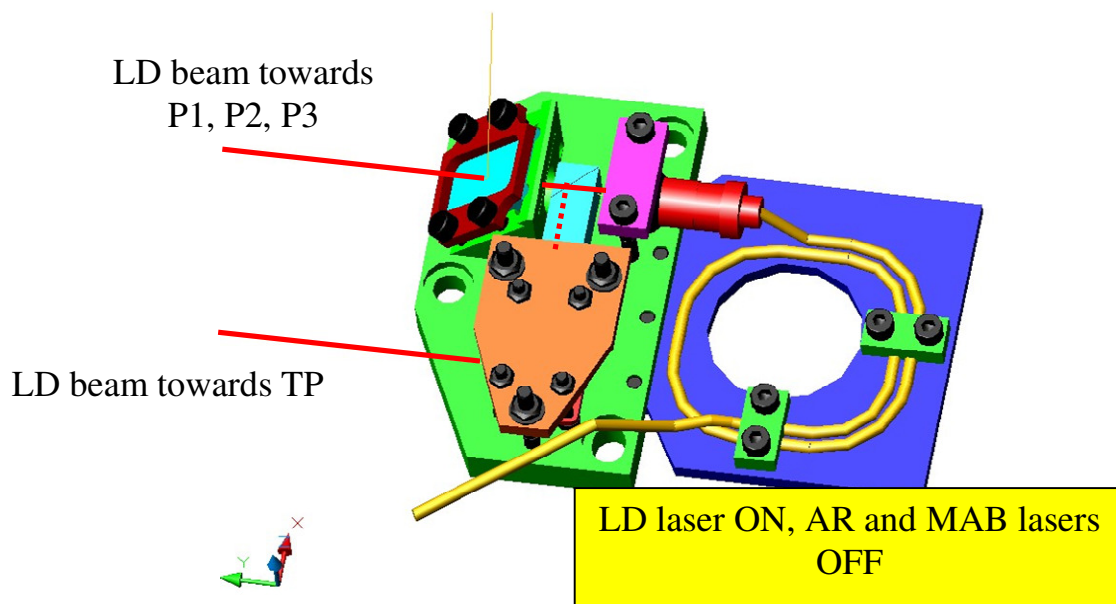
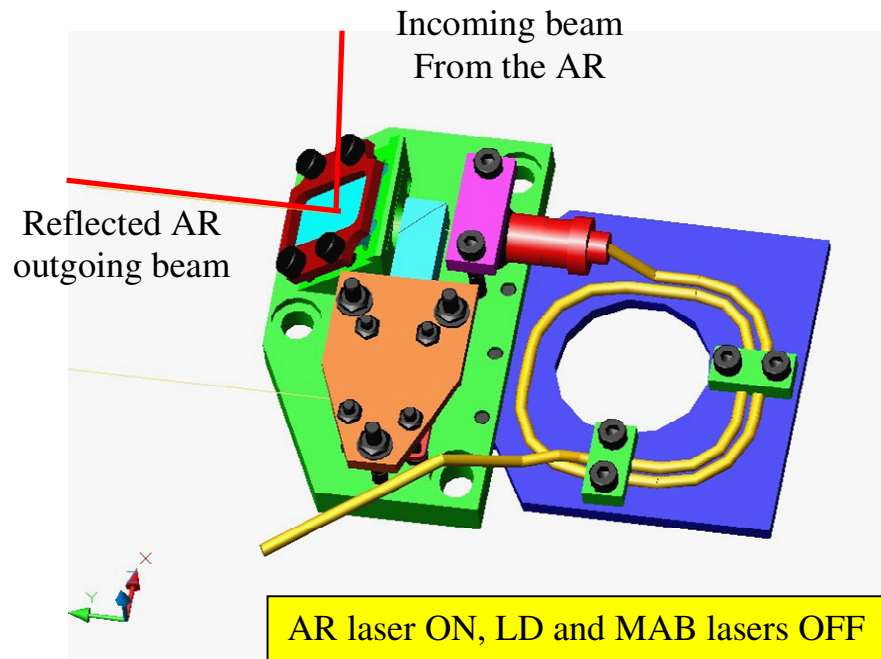


Fig. 19: Sketch of a Laser Box.

As a consequence of the obligatory sequence of lighting on and off of lasers and the reading out of photocurrents in the sensors and the reconstruction of the centres of the light spots on the ASPD surfaces, one full sensors data set takes a total of six minutes during MT runs and more than twenty for the full system in CRAFT runs.

The task of ASPD readout and control is accomplished by a devoted home made electronics called Local Electronic Board [11].

7.1 The Local Electronic Board.

The Local Electronic Board (LEB) is the signal processor board that controls the ASPD readout. It converts current to voltage, digitises analogue signals, reconstructs the light beam spatial position coordinates and communicates with a central PC. A single LEB can control up to 4 ASPD sensors simultaneously.

The LEB board diagram is shown in Fig. 20 a). The LEBs can communicate with each other through a specific purpose bus, the *Bus Interface (BI)*. Since CAN bus is a common standard, LEBs also integrate a *CAN Interface (CI)* card consisting of a CAN driver (DRV), an optocoupled interface (OI) and a CAN controller (CC), which allow LEBs to communicate between each other and with a central PC using the CANopen communication protocol.

An *ASPD Control Interface (ACI)* generates and sends control signals to up to 4 remote ASPD units. The *ASPD Signal Conditioner (ASC)* converts output currents to voltage and amplifies the signals to adapt voltage levels to the ADC input voltage. The current to voltage conversion proceeds in two steps. In the first one a high precision resistor is used as feedback of an operational amplifier in order to convert current to voltage. In the second one a variable gain amplifier adapts the signal to the ADC input range. Gains are adjustable and may be different for each sensor in a chain and even different for horizontal and vertical strips in a given sensor.

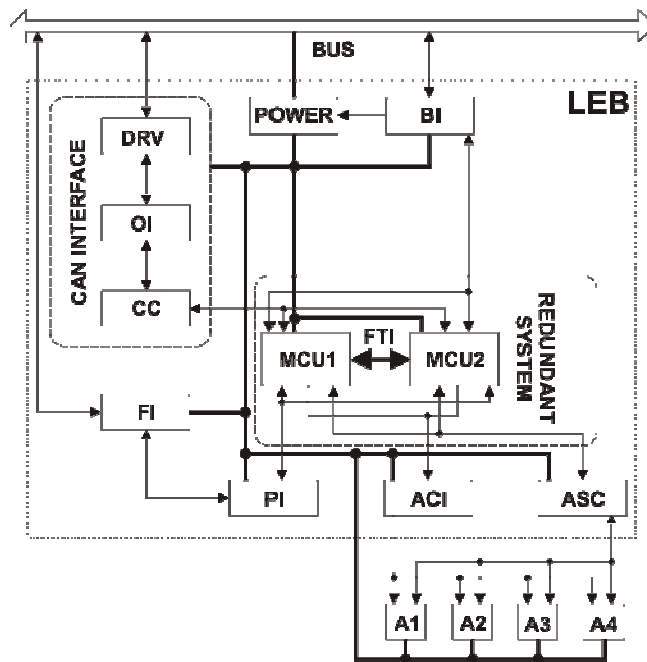
In order to overcome eventual environmental radiation effects (latch up included), fault tolerant mechanisms are implemented by a *Redundant Controller System* with a *Fault Tolerant Interface (FTI)* which controls LEB operation in a redundant mode. It includes two *Micro Controller Units (MCU, Hitachi, H8S/2357)* and the interface between them.

A *Fault Injection board interface (FI)* is used to program the MCUs via an RS-232 serial port. It controls fault injection campaigns and communicates with an external application.

Finally, a *Programming Interface (PI)* allows one to configure the MCUs programming. It supports two programming modes: via PC and cloning through the FI board.

The photograph in Fig. 20 b) shows an uncovered LEB after mounting of all of its components.

a)



b)

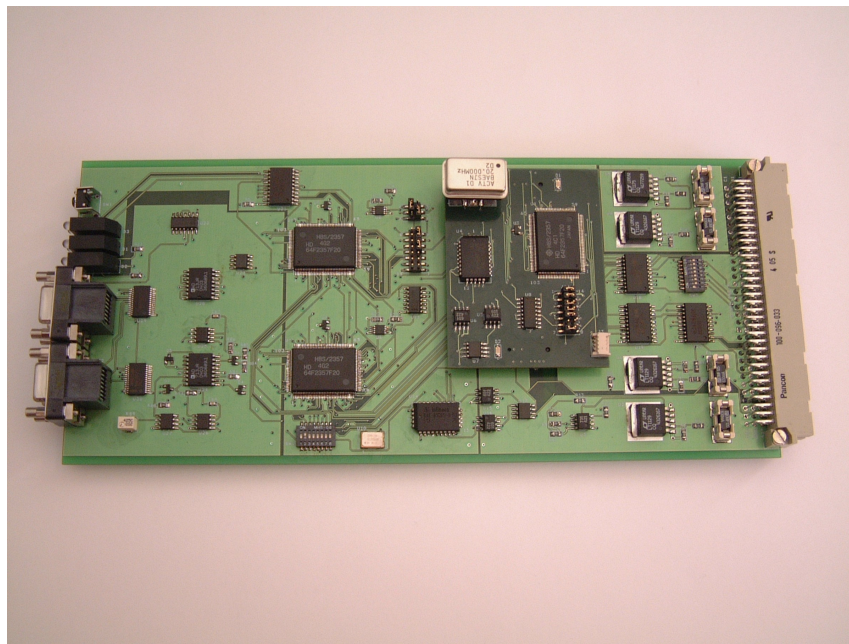


Figure 20: The Local Electronic Board for ASPD control, readout and light spots reconstructions. a) Board diagram. b) Uncovered LEB after mounting of all of its components.

7.2 Expected average resolutions in the reconstruction of the light spots on the sensors

The laser beam in a given light path crosses a first sensor and then reaches a second one with an incident angle (in the X and the Y directions) that follows a Gaussian distribution with central value and width (rms) as measured in the characterization process of the first sensor. The reconstruction uncertainty in the second one, $\sigma_2(\text{rec})$, is therefore affected by an additional term, related to the uncertainty in the deflection angles, that can be written as: $\sigma_2^{\text{def}} = \sigma_1(\text{def}) \times d_{12}$ (where $\sigma_1(\text{def})$ is the width of the deflection angle distribution of sensor 1 and d_{12} the distance between sensors 1 and 2), to be added quadratically to the spatial reconstruction resolution of the second sensor.

The light ray is subsequently deflected in each of the downstream sensors in the given light path, always according with their measured values of deflection angles. In a general way, the resulting incident angular distribution on the sensors surfaces is the convolution of the deflections happening successively in the upstream sensors, each of them having its own Gaussian-like distribution. The average deflection in sensor “j”, due to the presence of several upstream sensors “i” ($i=1, j-1$), can therefore be written as:

$$\Delta_j = \sum_{i=1, j-1} (\Theta_i \times d_{ij}),$$

where Θ_i is the deflection angle of sensor “i”. The error induced in the reconstruction process in sensor “j” can be expressed as:

$$\sigma_j = \{ \sigma_j^2(\text{rec}) + \sum_{i=1, j-1} [\sigma_i(\text{def}) \times d_{ij}]^2 \}^{1/2}$$

Above expressions apply to both coordinates, X and Y.

The value of σ_j is precisely the resolution in the detection of displacements of the j^{th} sensor in the line: the quantity that will allow determining whether a given sensor has moved or not from its initial position in the beam light. This quantity defines the spatial point reconstruction resolutions of a given sensor inside its light path and it will be used as the light spot coordinates reconstruction error.

Table 5 shows the calculated typical reconstruction resolutions of the various sensors in the various light paths using the average characteristics appearing in Table 4 and the sensor-to-sensor distances. All quantities appearing in Table 5 are given in micrometers.

Of course the table only provides an idea about the expected resolutions. For calculations one should use the actual characteristics of the sensors placed in a given laser line on top of the sensor-to-sensor distances, as it will be done in the examples given below.

Sensor	P1	P2	P3	P4	P5	P6	P7	P8
Light Paths 1 and 5	± 5	± 10	± 26					
Light Path 2				± 5	± 7	± 11		
Light Path 3							± 5	± 7
Light Path 4	± 24	± 14	± 5					

Table 5: *Expected average reconstruction resolutions of the ASPD sensors.*

The used sensor coordinate system is sketched in Fig. 21: X- and Y-axis are the detector local coordinates. The beam in the figure incomes by the active face of the sensor. In the Link System this is not always the case: in the Light Paths there are sensors receiving the laser beam by the glass face. Moreover, some of them are receiving laser light from both sides. On the other hand, sensors, on their supporting plates, are attached to different CMS elements in different orientations, as can be inferred by looking at Fig. 18. The meaning of the local to the sensor coordinates in terms of CMS coordinates may be complicated.

With the distribution of the photocurrents in the vertical strips one reconstructs the local to the sensor X-coordinate of the light spot (according to Fig. 21) while using the information provided by the horizontal strips one reconstructs the local to the sensor Y-coordinate. Notice that the spot light reconstruction on the sensors will be referred to its geometrical center, whose coordinates are taken to be (0, 0). Since the strip pitch is 0.430 mm and we cannot reconstruct in front of the centre of the strip 0, nor beyond the centre of the strip 63, the reconstruction limits are ± 13.545 mm in the two directions of the plane perpendicular to the incoming laser beam. The usable active area of an ASPD is then $\sim 27 \times 27$ mm².

In what follows we give two examples of the analysis of ASPD data.

7.3 First example: monitoring of motions along the Light Path 1, at the $\Phi = +75^\circ$ quarter, during the Phase I of the MT and the CRAFT runs and comparison of results

The light path 1 starts at the collimator placed in the Laser Box (see Figs. 18 and 19). The beam goes out and crosses the sensors P1, located at the TP and P2 and P3, attached at the bottom and the top of the corresponding MAB.

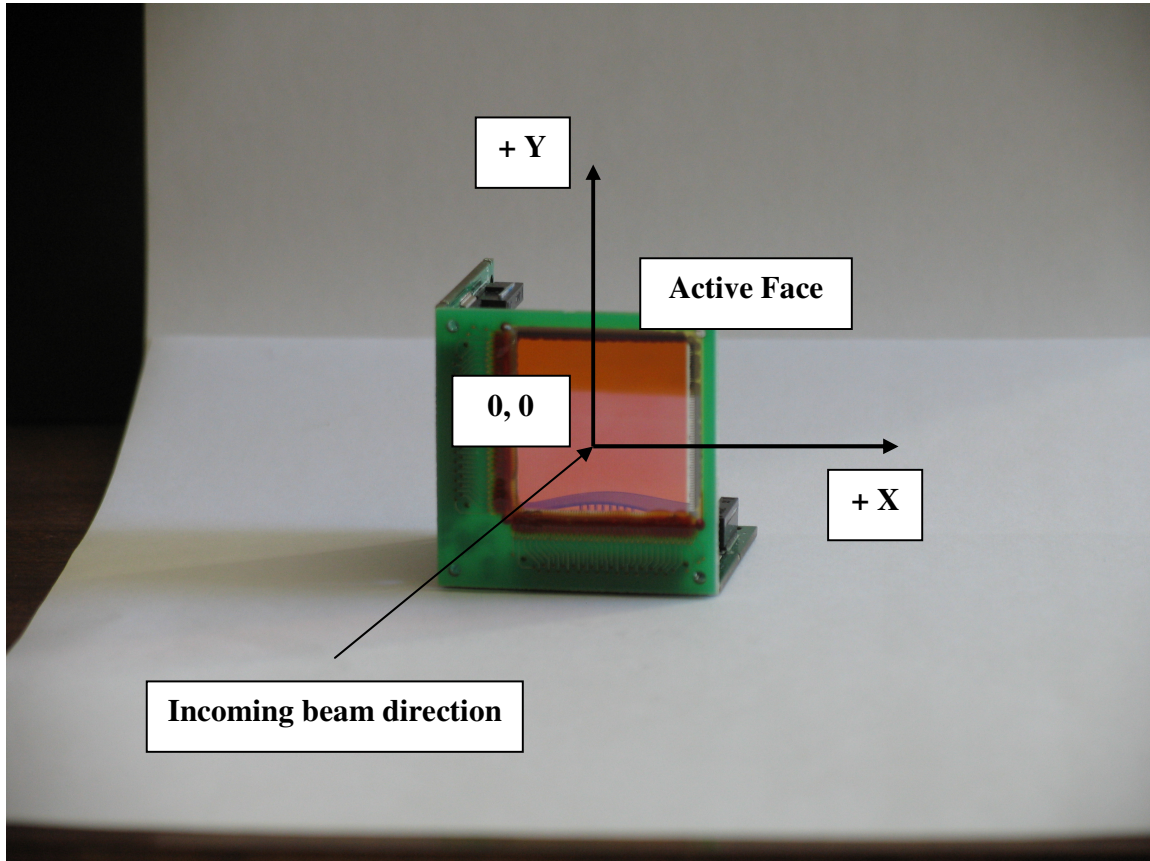


Fig. 21: Photograph of an ASPD sensor with its local axis system of coordinates.

What we are monitoring with this laser beam are the relative motions, in a plane perpendicular to the laser beam, of the elements TP, and bottom ant top positions of the MAB structure. Note that the MAB is, in principle, a rigid structure and hence, this laser beam also monitors eventual MAB deformation.

For the three sensors in the light line 1 (see Fig. 18), their local coordinates (X and Y) are related to the CMS coordinates and angular definitions as follows: Y is parallel to the $-Z$ CMS axis and X is perpendicular to R at the Z position of sensor PI (I = 1, 3) in CMS in this Φ quarter.

Therefore, a variation in Y corresponds to a displacement in Z and a variation in X corresponds to a rotation in Φ . For two reconstructions of the light spot done at different times, t1 and t2, the interpretation in terms of the CMS variables will be,

$$\text{At } +Z_{\text{cms}}: \Delta Z = Z_2 - Z_1 = -(Y_{t2} - Y_{t1}) \text{ and } \Delta\Phi = \Phi_2 - \Phi_1 = \arctg(X_{t2} - X_{t1})/RPI, I = 1, 2, 3.$$

$$\text{At } -Z_{\text{cms}}: \Delta Z = Z_2 - Z_1 = Y_{t2} - Y_{t1} \text{ and } \Delta\Phi = \Phi_2 - \Phi_1 = -\arctg(X_{t2} - X_{t1})/RPI, I = 1, 2, 3.$$

With: RP1 = 2.770 m, RP2 = 4.423 m and RP3 = 6.961 m.

For the spatial reconstruction errors we have to use the characteristics of the three sensors installed in the light line [22, 23], the sensor-to-sensor distances given in 7 and the formula for σ_j given in 7.2.

Table 6 summarizes the reconstruction of signals, for this Light Path 1 in the quarter plane of $\Phi = +75^\circ$ during the MT Phase I run. X_i and Y_i represent, in the local sensor coordinates system, the reconstruction of the center of the light spot, at the beginning of the cycle $B = 0T - 4T - 0T$. X_{4T} and Y_{4T} , the reconstructed beam position at $B = 4T$ and X_f and Y_f the reconstructed coordinates at the end of the cycle, at $B = 0T$.

The interpretation of the results in Table 6 is far to be unique. For instance, measured displacements and rotations with sensor P1 may be due to a convolution of eventual displacements and/or rotations of the following elements: TP, LD and AR.

In the same manner, measured displacements and rotations with sensors P2 and P3 may be due to a convolution of eventual displacements and/or rotations of the following elements: MAB, TP, LD and AR. The correct interpretation can only be done by a full geometrical reconstruction of the Link data in a given event [19].

Due to the fact that the full ASPDs data taking last 27 min. at the CRAFT run, we have only four data points recorded at $B = 0T$ and other four at $B = 4T$. Therefore the on and under ground comparison will be reduced to the overall $0T$ to $4T$ motions. Results are displayed in the last two rows of Table 4.

Sensors	P1	P2	P3
X_i (mm)	-2.665 ± 0.007	10.171 ± 0.006	10.732 ± 0.015
Y_i (mm)	3.169 ± 0.005	8.876 ± 0.006	12.495 ± 0.014
X_{4T} (mm)	-1.097 ± 0.007	-4.516 ± 0.006	-3.690 ± 0.015
Y_{4T} (mm)	3.225 ± 0.005	9.325 ± 0.006	13.477 ± 0.014
X_f (mm)	-3.043 ± 0.007	10.893 ± 0.006	11.008 ± 0.015
Y_f (mm)	3.284 ± 0.005	9.013 ± 0.006	12.512 ± 0.014
$\Delta\Phi$ [f-i] (mrad)	-0.136 ± 0.004	0.163 ± 0.002	0.004 ± 0.003
ΔZ [f-i] (mm)	-0.115 ± 0.007	-0.137 ± 0.008	-0.017 ± 0.020
$\Delta\Phi_{04T}$ (mrad)	0.566 ± 0.004	-3.321 ± 0.002	-2.072 ± 0.003
ΔZ_{04T} (mm)	-0.056 ± 0.007	-0.449 ± 0.008	-0.982 ± 0.020
$\Delta\Phi_{04T}$ CRAFT (mrad)	0.168 ± 0.004	-2.784 ± 0.002	-1.241 ± 0.003
ΔZ_{04T} CRAFT (mm)	-0.087 ± 0.007	-0.524 ± 0.008	-0.402 ± 0.020

Table 6: Summary of the reconstruction of signals, from the Light Path 1 in the quarter plane of $\Phi = 75^\circ$ during the MT Phase I and the **CRAFT** run: recovery and maximum motions

Observations on and under ground, from this particular Φ quarter and this Light Path, are in a very fair agreement: as seen from the LB, the effect of the magnetic field is a translation of the TP towards the ME/1/1 chamber (towards the IP) of $87 \mu\text{m}$ at CRAFT ($56 \mu\text{m}$ at MT) and a simultaneous small tilt of the same mechanical element of 0.168 mrad at CRAFT (0.566 mrad at MT), while the corresponding $\Phi=+75^\circ$ MAB also seems to move towards the IP in a ΔZ of $463 \mu\text{m}$ at CRAFT ($716 \mu\text{m}$ at MT), but tilting in Φ in the opposite direction of that of the TP by about -2.013 mrad at CRAFT (-2.697 mrad, at MT).

7.4 Second example: monitoring of motions along the Light Path 1: LB→ P1-P2-P3 and Light Path 4: LL→ P3-P2-P1 at $\Phi = 75^\circ$ during the CRAFT run data: comparison of results at +Z and -Z CMS sides

As said we have only four data points recorded at B = 0T and other four at B= 4T. Therefore the analysis will only relate to the difference in the sensors positions at this two magnetic field values from the reconstructed light spots originated by the LB and LL (the Laser Level installed on each MAB, see Fig. 8) collimators.

The results are shown in Tables 7 and 8 for the +Z side and Tables 9 and 10 for the - Z CMS side.

B Motions	XP1(mm)	YP1(mm)	XP2(mm)	YP2(mm)	XP3(mm)	YP3(mm)
4T	-6.250 ± 0.007	2.068 ± 0.005	0.454 ± 0.006	2.105 ± 0.006	6.331 ± 0.015	3.656 ± 0.014
0T	-6.715 ± 0.007	1.981 ± 0.005	12.767 ± 0.006	1.581 ± 0.006	14.968 ± 0.015	3.254 ± 0.014
ΔZ (mm)		-0.087 ± 0.007		-0.524 ± 0.008		-0.402 ± 0.020
$\Delta\Phi$ (mrad)	0.168 ± 0.004		-2.784 ± 0.002		-1.241 ± 0.003	

Table 7: Positions and motions monitored by the ASPDs in the Light Path 1 during the CRAFT run in quarter $\Phi = 75^\circ$ at +Z side

Inspection of Table 7 reveals that, as seen from the LB, the effect of the magnetic field is a translation of the TP towards the ME/1/1 chamber (towards the IP) of 87 μm and a simultaneous small tilt of the same mechanical element of 0.168 mrad, while the corresponding MAB also seems to move towards the IP in a ΔZ of 463 μm , but tilting in Φ in the opposite direction of that of the TP by about -2.013 mrad.

B Motions	XP1(mm)	YP1(mm)	XP2(mm)	YP2(mm)	XP3(mm)	YP3(mm)
4T	-6.691 ± 0.017	-7.494 ± 0.031	-2.095 ± 0.011	-5.040 ± 0.020	-0.095 ± 0.007	0.060 ± 0.004
0T	-6.098 ± 0.017	-7.212 ± 0.031	-0.099 ± 0.011	0.056 ± 0.020	-0.097 ± 0.007	0.056 ± 0.004
ΔZ (mm)		0.282 ± 0.044		5.096 ± 0.028		-0.004 ± 0.006
$\Delta\Phi$ (mrad)	-4.617 ± 0.009		-0.451 ± 0.004		0.0003 ± 0.002	

Table 8: Positions and motions monitored by the ASPDs in the Light Path 4 during the CRAFT run in quarter $\Phi = 75^\circ$ at +Z side

In the Light Path 4 the laser beam goes out from the collimator at the LL, about 10 cm above P3 on the MAB, crossing sequentially sensors P3, P2 and P1.

Since LL, P3 and P2 are all three attached to the MAB, we expect to see no variation in Φ of these two sensors. However, the result, displayed in the fifth row in Table 8, shows a small tilt of $\Delta\Phi = -0.225$ mrad, while P1, at the TP, seems to tilt in $\Delta\Phi = -4.617$ mrad, twice the detected Φ tilt of the MAB in Table 7.

Concerning ΔZ displacements, both TP and MAB seems to move towards ME/1/1 chamber, in values of 282 μm and about 2.5 mm respectively.

B Motions	XP1(mm)	YP1(mm)	XP2(mm)	YP2(mm)	XP3(mm)	YP3(mm)
4T	5.590 \pm 0.003	-10.584 \pm 0.006	-11.814 \pm 0.005	-3.898 \pm 0.005	-6.100 \pm 0.013	10.631 \pm 0.013
0T	5.630 \pm 0.003	-10.861 \pm 0.006	-10.050 \pm 0.005	-4.300 \pm 0.005	-6.012 \pm 0.013	12.706 \pm 0.013
ΔZ (mm)		0.277 \pm 0.008		0.402 \pm 0.007		-0.075 \pm 0.018
$\Delta\Phi$ (mrad)	0.014 \pm 0.002		0.399 \pm 0.002		0.013 \pm 0.003	

Table 9: Positions and motions monitored by the ASPDs in the Light Path 1 during the CRAFT run in quarter $\Phi = 75^\circ$ at $-Z$ side

Inspection of Table 9 reveals that, as seen from the LB, the effect of the magnetic field is a displacement of the TP towards the ME/1/1 chamber (towards the IP) of 277 μm and a negligible tilt of +0.014 mrad, while the corresponding $\Phi = -15^\circ$ MAB also seems to displace towards the IP in ~ 164 μm , tilting in Φ by about 0.206 mrad.

B Motions	XP1(mm)	YP1(mm)	XP2(mm)	YP2(mm)	XP3(mm)	YP3(mm)
4T	-1.683 \pm 0.007	-8.214 \pm 0.013	1.302 \pm 0.006	1.200 \pm 0.004	0.621 \pm 0.005	0.382 \pm 0.004
0T	-1.664 \pm 0.007	4.398 \pm 0.013	1.335 \pm 0.006	1.333 \pm 0.004	0.618 \pm 0.005	0.384 \pm 0.004
ΔZ (mm)		-12.606 \pm 0.018		-0.133 \pm 0.006		-0.002 \pm 0.006
$\Delta\Phi$ (mrad)	0.007 \pm 0.003		0.007 \pm 0.002		-0.0004 \pm 0.0010	

Table 10: Positions and motions monitored by the ASPDs in the Light Path 4 during the CRAFT run in quarter $\Phi = 75^\circ$ $-Z$ side

As expected we see no variation in Φ of sensors P2 and P3 as displayed in the fifth row in Table 10, while P1, at the TP, shows also no tilt: $\Delta\Phi = 0.007$ mrad.

Concerning ΔZ displacements, we observe a negligible shift of the MAB of about $65\ \mu\text{m}$ away from the IP and an unphysical shift of almost $13\ \text{mm}$ of the TP away from the IP, clearly denoting a data miss recording.

8. Monitoring of displacements with proximity sensors from on ground (MT) and under ground (CRAFT) runs

The monitoring of the relative displacements (along the Z and $R\Phi$ directions) between some CMS elements, relevant for the Link Alignment System, is done with the help of long aluminium bars (for long distances) and contact and non contact proximity sensors (for short distances).

8.1 Monitoring the axial (along Z) distance between the Link Disk and the Alignment Ring at the MT

The monitoring of the distance between the Link Disk and the Alignment Ring is done via an aluminium tube (LP, longitudinal profile, in Fig. 8), attached to the LD, $\sim 3600\ \text{mm}$ long, to which, on its closed end to the AR is installed a target. The rod of a Sakae [12] potentiometer (PS_AR), located at the AR, contacts the LP target (see Figs. 8 and 22), allowing to monitor the relative motions between LD and AR structures.

In that manner, the long distance between the LD and the AR will be given by the LP length plus the length of the potentiometer mechanical support ($89.087\ \text{mm}$) plus the distance measured by the potentiometer.

The error of the 3D measuring machine used to determine the length of the various sensor mechanical supports is in the range $5 - 10\ \mu\text{m}$ and the typical precision in the short-distances measurement with the sensors used in the Link System stays, according with our bench calibrations [14], in the range $30 - 40\ \mu\text{m}$. However, the uncertainty in the spatial location of sensors related to the mounting in CMS is never smaller than $100\ \mu\text{m}$.

Three LP/PS_AR sets are attached to the LD at Φ angles of 75° , 195° and 315° . As already mentioned and sketched in Figs. 8 and 20, the LD is “hanging” from the Transfer Plate by means of six aluminium profiles, each attached to its corresponding TP, that, in turn, is attached to the YN/1 iron disk; therefore, what we are measuring is, in fact, the motions of the endcap iron wheels towards the Tracker, when the solenoid is switched on, and their retraction away from the Tracker when the magnet is switched off.

The length of the sensor mechanical support plus the sensor output signal is the quantity we are going to study to analyse the LD–AR (or YN/1–TK) relative displacements at the three +Z equipped angles during the MT. This length will be called Z.

The estimated combined errors (mechanical support length plus proximity sensor output plus the mounting uncertainty) on this measurement, is about $120\ \mu\text{m}$. However, when

measuring relative distances the resolution is that of the used sensor. So, for the study of relative displacements we will use $40\ \mu\text{m}$ as the measurement error.

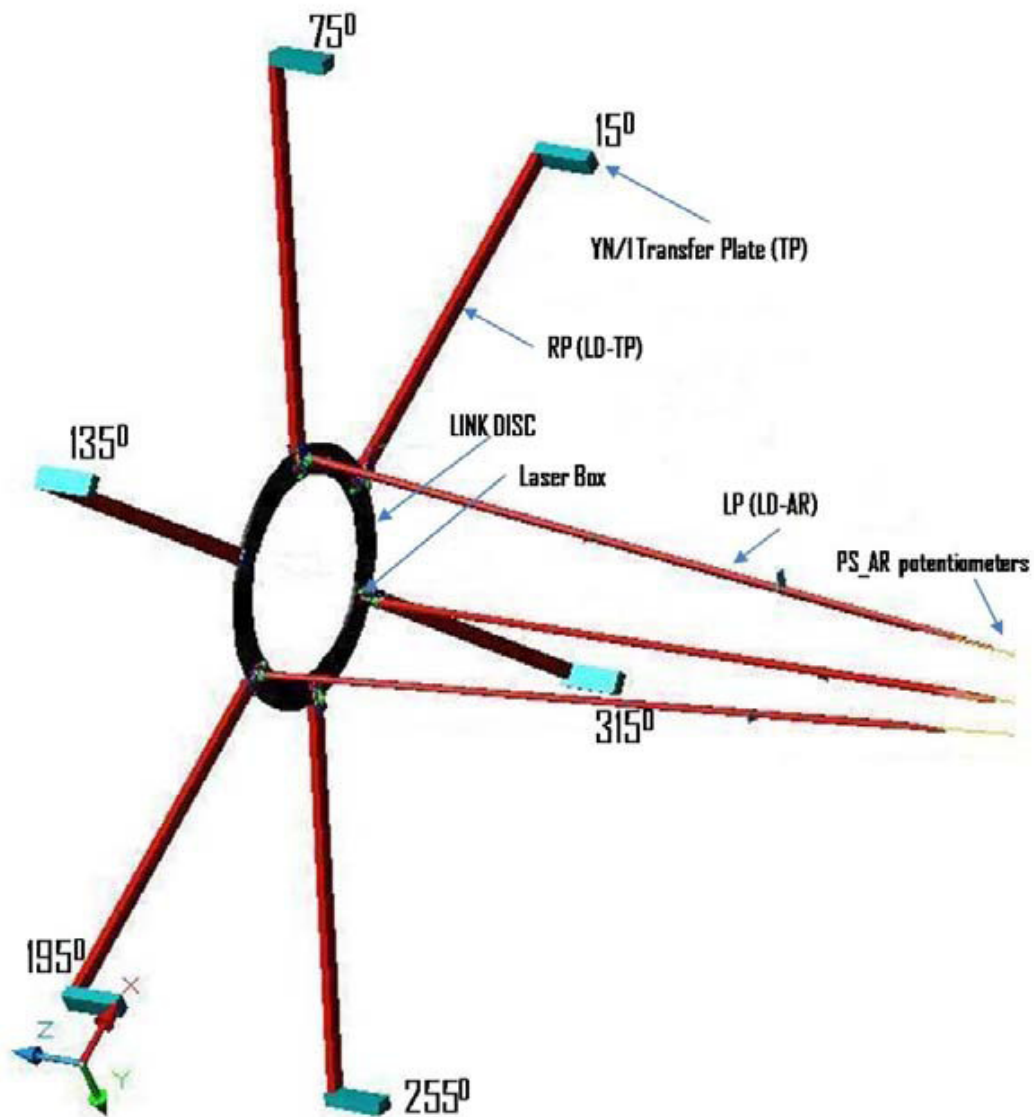


Fig. 22: Sketch of the monitoring of the relative distance between AR and LD (see text).

The AR was in place only during the Phase I of the MT. Before starting the Phase II, the TK mock-up and therefore the AR, were removed to allow the insertion of the field mapper to construct the field map inside the solenoid.

Let us start by comparing the repositioning of the LD in the three instrumented quarters in the selected run for Phase I.

Table 11 (three first rows) shows the value of Z , at $B = 0$ T, at the beginning (Z_b) and the end (Z_a) of the run and the differences between these two measurements, $\Delta Z = Z_a - Z_b$, for each of the three Φ quarters.

Φ quarter	75°	195°	315°
Z_b (mm)	93.678 ± 0.040	88.915 ± 0.040	89.909 ± 0.040
Z_a (mm)	93.514 ± 0.040	88.863 ± 0.040	89.338 ± 0.040
ΔZ (mm)	-0.165 ± 0.057	-0.052 ± 0.057	-0.571 ± 0.057
Z_{4T} (mm)	77.937 ± 0.040	73.375 ± 0.040	74.309 ± 0.040
ΔZ_{04T} (mm)	-15.741 ± 0.057	-15.540 ± 0.057	-15.599 ± 0.057

Table 11: Monitoring of the relative distance between the LD (YNI) and the AR (TK) during the Phase I.

Also in Table 11 (last two rows) we give the values of Z measured at $B = 4$ T, Z_{4T} , and the corresponding displacements, ΔZ_{04T} , with respect to the initial value Z_b .

Two relevant facts derive from the inspection of Table 11. First, the expected elastic motions (see ΔZ values) are verified (within 3σ) only in the 75° and 195° regions, but not in the 315° one. At the bottom quadrant the initial LD – AR distance is not retrieved: the LD is repositioned closer to the AR (Tracker) that it was before the ramp in field by about half a millimetre.

Second, these measurements may reveal a slight up/down asymmetry (smaller than 3σ) in the motion of the CMS components when the magnet is on (see ΔZ_{04T} values).

The behaviour of the difference $\Delta Z = Z(B) - Z(0)$, in the three quadrants, as a function of the field intensity B , is shown in Fig. 23. $Z(B)$ is the output signal of the sensor when the field reaches the intensity B and $Z(0)$ is the measured distance at the start of the run. Dots, circles and stars in Fig. 23 correspond to sensors at 75° , 195° and 315° quarters, respectively. For clarity of the figure, only one data every 100 was plotted. The curves represent fits to each of the three data sets. The behaviour is very similar for the three quadrants: data points and fitted curves are almost on top of each others.

The behaviour is quadratic in B and the three sets of data points accept fits to the form:

$$\Delta Z = a \times B^2 + b \times B + c$$

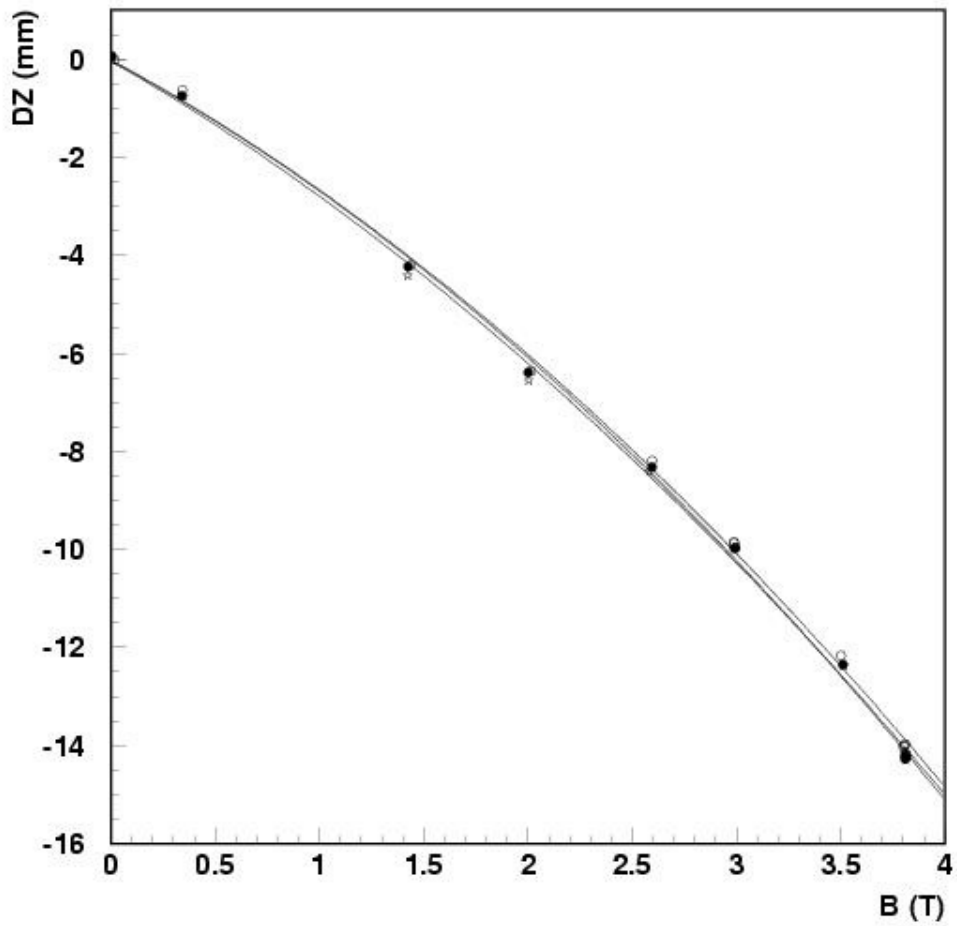


Fig. 23: Measured distance between the LD and the AR (with respect to the measured distance at the beginning of the phase) as a function of \mathbf{B} in the phase I of the MT. Dots, circles and stars correspond to sensors at 75° , 195° and 315° , respectively. The curves represent the fits to each of the three data sets (see text).

The results of the fits are given in Table 12. The imposed theoretical error for ΔZ in the X^2 fit was 0.057 mm.

	a (mm/T ²)	b (mm/T)	c (mm)	X ² /NDF	Residuals widths (mm)
75°	-0.371 ± 0.006	-2.283 ± 0.024	-0.043 ± 0.022	2285/1048	0.177
195°	-0.350 ± 0.006	-2.308 ± 0.024	-0.017 ± 0.022	2523/1048	0.186
315°	-0.328 ± 0.006	-2.426 ± 0.024	-0.048 ± 0.022	2670/1048	0.191

Table 12: Fitted parameters of the relative displacements between LD and AR as a function of B .

The fitted parameters are of the same order of magnitude for the three Φ quarters. The only observation is the need of a substantial linear term in B in the fitted function.

8.1.1 Monitoring the axial (along Z) distance between the Link Disk and the Alignment Ring at the CRAFT run and comparison with the on ground observations.

At the P5 pit, six LP/PS_AR sets are attached to the LD at Φ angles of $\pm 75^\circ$, $\pm 195^\circ$ and $\pm 315^\circ$. The sign in front of the angle refers to the CMS Z side (Φ is positive defined). During the CRAFT run, the proximity sensor at $\Phi = -75^\circ$ was not connected properly and the readout was all the time 0V.

Let us start by watching at the ΔZ behaviours, as a function of the data number (time), in both runs on (Fig. 24, MT, Phase I) and under ground (Figs. 25 and 26). Plot a) in all the three figures is the magnetic field intensity along the corresponding run. All other plots show the relative distance (with respect to the first data in each run) measured between the LD and the AR. It is clear, in all cases, that the recorded distance follows the changes in the field intensity.

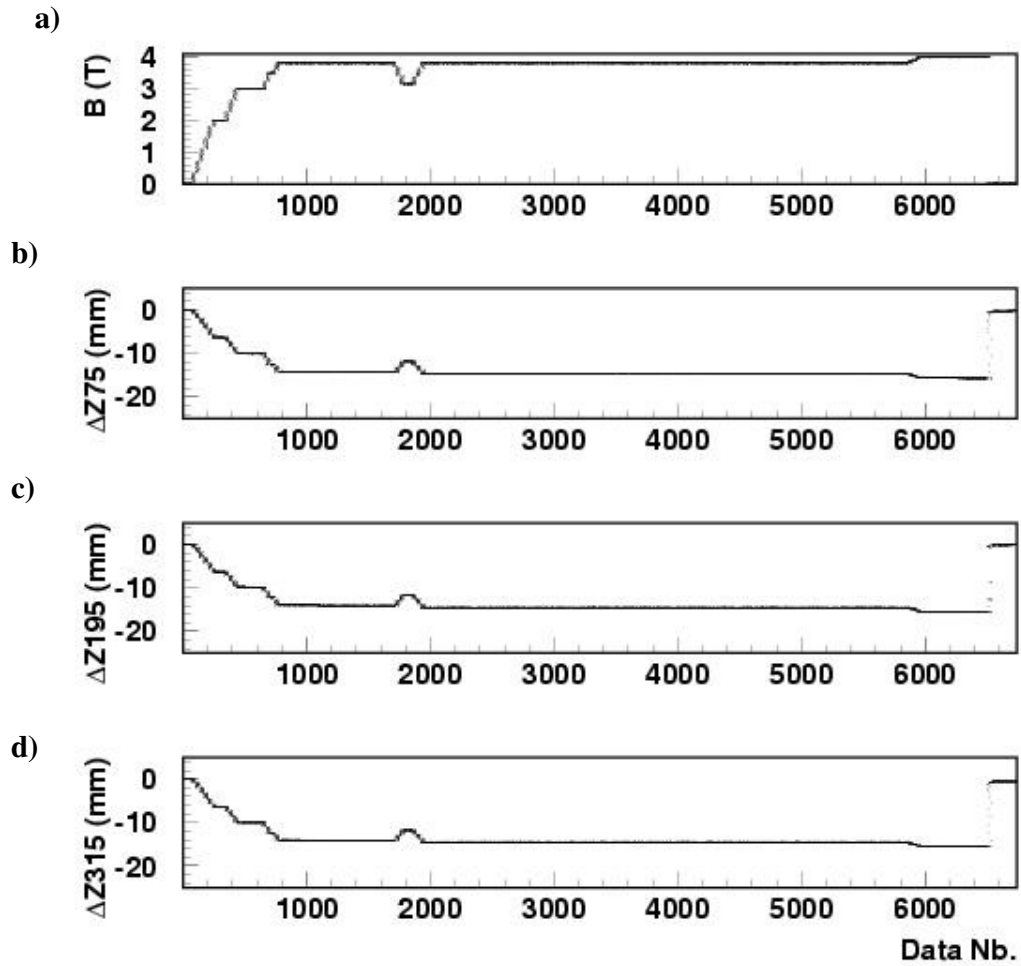


Fig. 24: From the last run in Phase I. a) Magnetic field intensity as a function of time (data number). b), c) and d) Relative distance between the LD and the AR in each of the three equipped quarters.

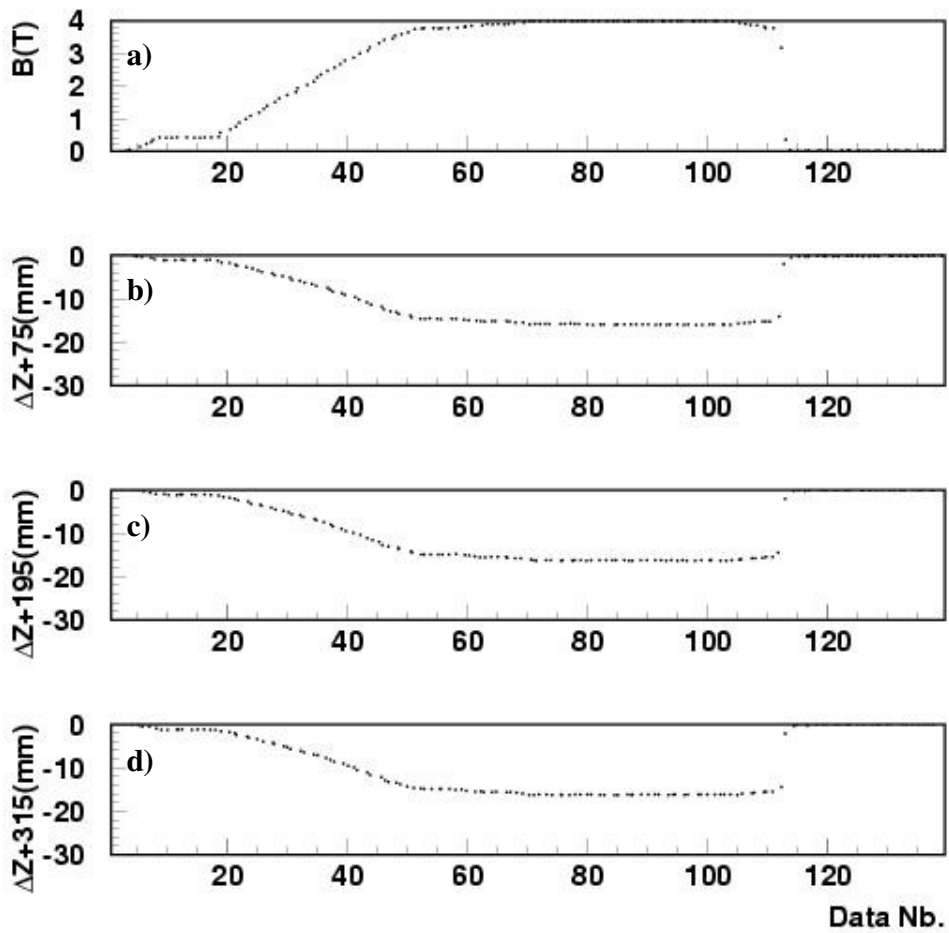


Fig. 25: From the CRAFT run. a) Magnetic field intensity as a function of time (data number). b), c) and d) Relative distance between the LD and the AR in each of the three +Z quarters.

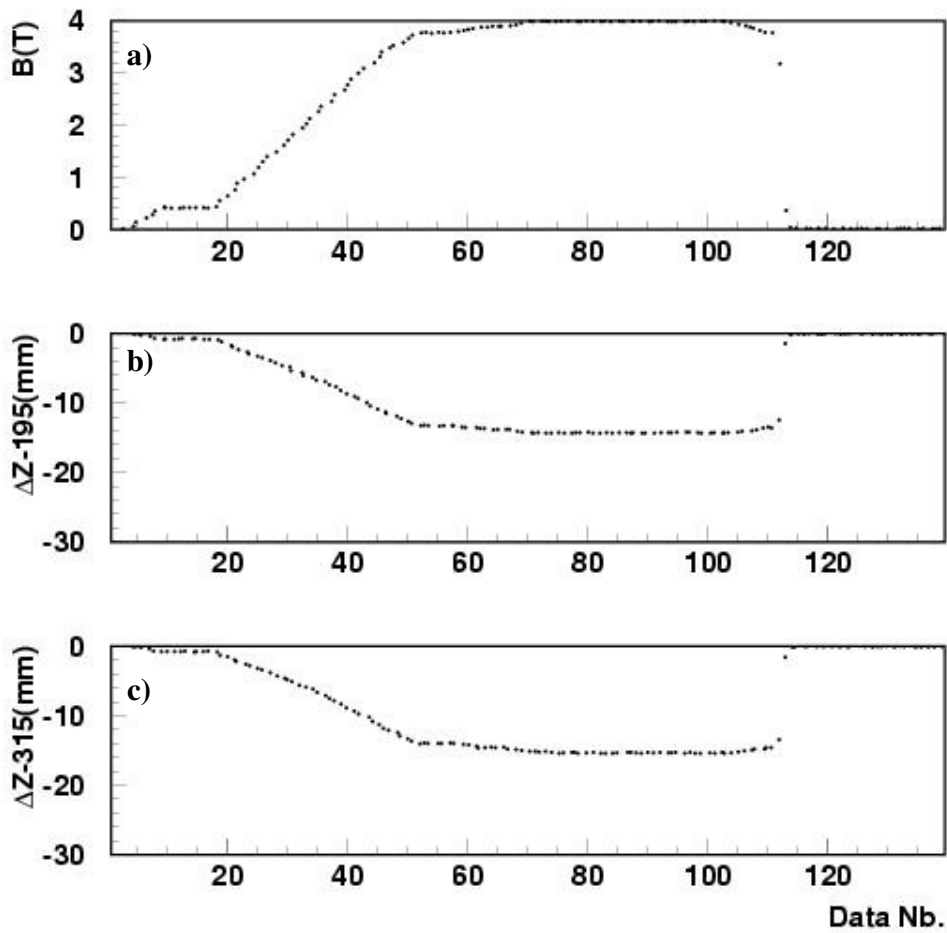


Fig. 26: From the CRAFT run. a) Magnetic field intensity as a function of time (data number), b) and c) Relative distance between the LD and the AR in each of the two working $-Z$ quarters.

Following the convention in Table 11, we display in Table 13 the values measured for the repositioning (ΔZ) and the maximum displacement (ΔZ_{04T}). Symbols + and – apply for the CMS sides.

Φ quarter	75°	195°	315°
$\Delta Z +$ (mm)	-0.205 ± 0.057	-0.168 ± 0.057	-0.171 ± 0.057
$\Delta Z -$ (mm)	----	-0.065 ± 0.057	-0.086 ± 0.057
$\Delta Z +$ (mm) in MT	-0.165 ± 0.057	-0.052 ± 0.057	-0.571 ± 0.057
$\Delta Z_{04T} +$ (mm)	-15.938 ± 0.057	-16.267 ± 0.057	-16.336 ± 0.057
$\Delta Z_{04T} -$ (mm)	----	-14.336 ± 0.057	-15.339 ± 0.057
$\Delta Z_{04T} +$ (mm) in MT	-15.741 ± 0.057	-15.540 ± 0.057	-15.599 ± 0.057

Table 13: *Measurement of the repositioning and maximum displacement between the LD (YNI) and the AR (TK) at the two CMS Z sides during the CRAFT run and at +Z in the MT run.*

As we discussed elsewhere [19] one should forget about elastic motions when operating with the CMS magnet. No position prior to a magnet on operation is retrieved when the magnet is switched of again. In addition, from observations in one particular run one can not make quantitative predictions about what is going to happen in the next one.

The values displayed in Table 13 for repositioning (ΔZ) are, in most of the cases, not compatible with zero, neither among them. Similarly, the measured maximum displacements between the LD and the AR (ΔZ_{04T}) show a difference of almost 1 mm when comparing the measurements done on ground and underground in the same Φ quarter as also happens (in more than 1 mm) when comparing displacements at +Z and –Z for the same CRAFT run.

The behaviour of the difference $\Delta Z = Z(B) - Z(0)$, in the +Z and –Z quadrants, as a function of the field intensity B, is shown in Fig. 27 and 28 respectively. Dots, circles and stars in figures correspond to sensors at 75° , 195° and 315° quarters, respectively. For clarity of the figure, only one data every 10 was plotted. The curves represent fits to each of the data sets. The behaviour is very similar for the three quadrants: data points and fitted curves are almost on top of each others.

The behaviour is quadratic in B and the three sets of data points accept fits to the form:

$$\Delta Z = a \times B^2 + b \times B + c$$

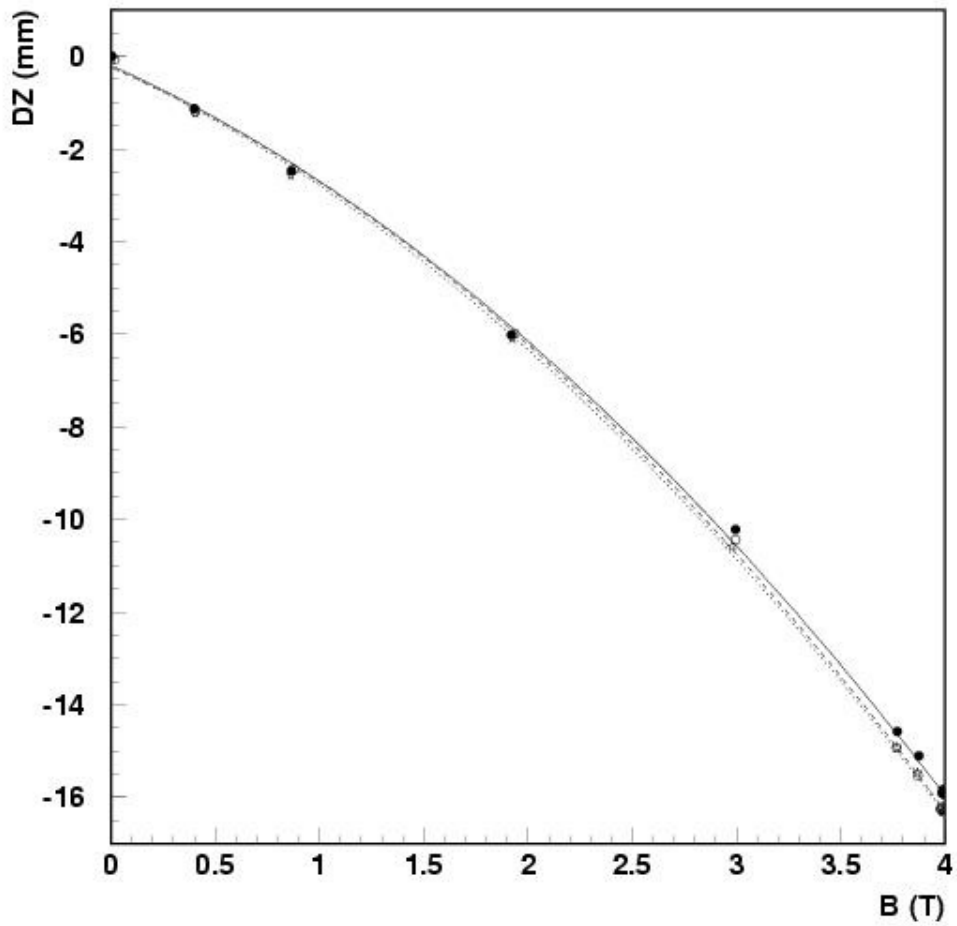


Fig. 27: Measured distance between the LD and the AR at +Z (with respect to the measured distance at the beginning of the phase) as a function of \mathbf{B} in the CRAFT run. Dots, circles and stars correspond to sensors at 75° , 195° and 315° , respectively. The curves represent the fits to each of the three data sets (see text).

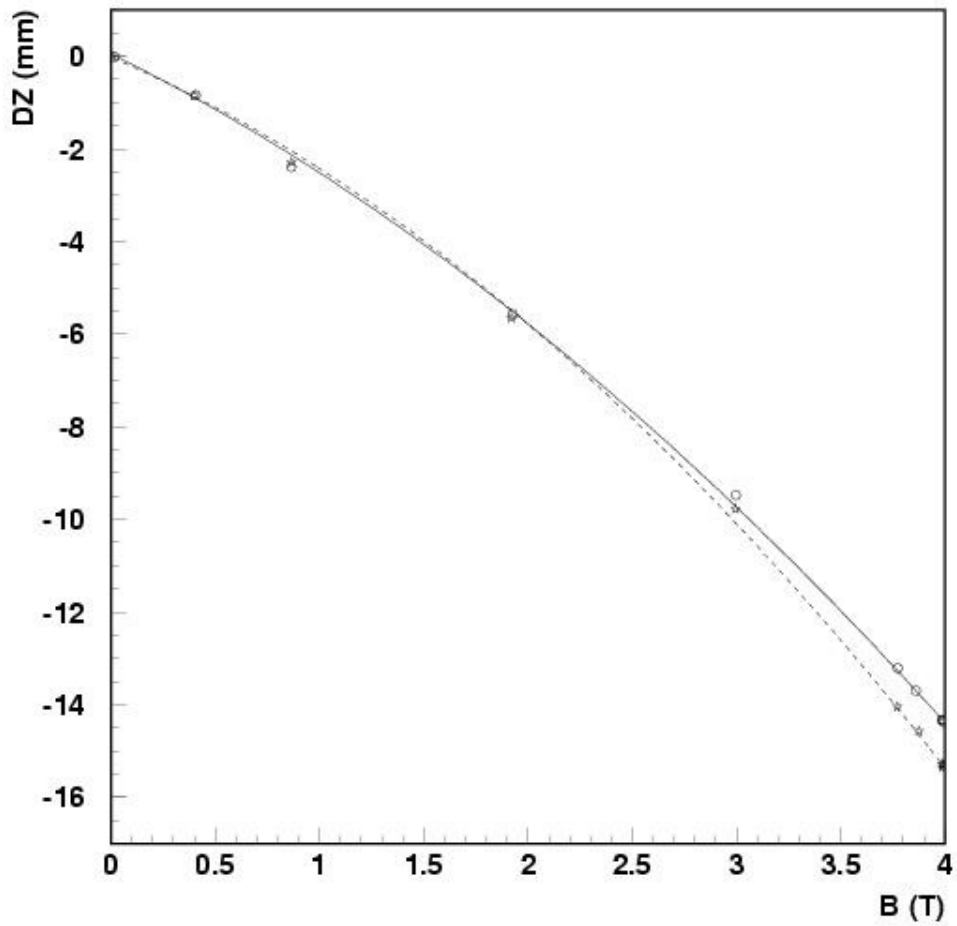


Fig. 28: Measured distance between the LD and the AR at $-Z$ (with respect to the measured distance at the beginning of the phase) as a function of \mathbf{B} in the CRAFT run. Circles and stars correspond to sensors at 195° and 315° , respectively. The curves represent the fits to each of the two data sets (see text).

The results of the fits are given in Table 14 for the underground (CRAFT) and the on ground (MT) runs. The imposed theoretical error for ΔZ in the X^2 fit was 0.057 mm.

	a (mm/T ²)	b (mm/T)	c (mm)	X ² /NDF	Residuals width (mm)
+75° (CRAFT)	-0.480 ± 0.010	-2.017 ± 0.047	-0.201 ± 0.038	98/98	0.118
+195° (CRAFT)	-0.510 ± 0.010	-1.974 ± 0.047	-0.242 ± 0.038	91/98	0.114
+315° (CRAFT)	-0.487 ± 0.010	-2.082 ± 0.047	-0.226 ± 0.038	91/98	0.113
-195° (CRAFT)	-0.347 ± 0.010	-2.222 ± 0.047	-0.051 ± 0.038	80/98	0.107
-315° (CRAFT)	-0.477 ± 0.010	-1.925 ± 0.047	-0.026 ± 0.038	101/98	0.120
+75° (MT)	-0.371 ± 0.006	-2.283 ± 0.024	-0.043 ± 0.022	2285/1048	0.177
+195° (MT)	-0.350 ± 0.006	-2.308 ± 0.024	-0.017 ± 0.022	2523/1048	0.186
+315° (MT)	-0.328 ± 0.006	-2.426 ± 0.024	-0.048 ± 0.022	2670/1048	0.191

Table 14: *Fitted parameters of the relative displacements between LD and AR as a function of B in all quarters for the CRAFT and the MT runs.*

The fitted parameters are of the same order of magnitude for the eight data sets analysed. The only observation is the need, as earlier mentioned, of a substantial linear term in B in the fitted function, both on and underground.

8.2 Monitoring the axial distance (along Z) between the Transfer Plate and the ME1/1 chamber

The monitoring of the relative distance between the TP (see sketch and photograph in Fig. 29) and the ME1/1 chamber is done with a Sakae potentiometer sensor (PS_TP) located at the transfer plate. The sensor is placed on a support 251.040 mm long and its rod contacts a target located on the ME1/1 chamber (see Fig. 8). In that manner, the distance between the TP and the ME1/1 will be given by the length of the potentiometer mechanical support plus the short distance measured by the potentiometer [12].

Let us call Z the measured relative distance at a given moment. The comparison between the repositioning ($\Delta Z(0)$) of the chamber with respect to the Transfer Plate after the cycle B = 0 T, B = 4 T and back to B = 0 T, measured by the proximity sensors in Phases I and II are displayed in the first three rows on Table 15 for the three Φ quadrants (75° , 255° and 315°).

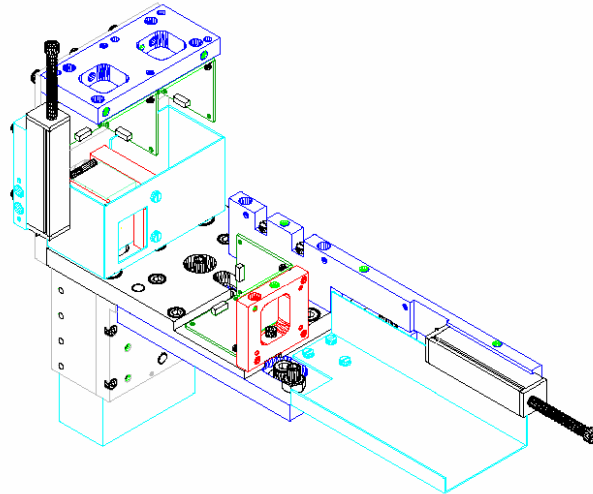
Also in Table 15, in the last three rows, we compare the total displacement (ΔZ_{04T}) suffered by the TP, with respect to the ME1/1 chamber, from the situation at B = 0 T, before starting the ramp up to 4 T, to the values when the magnet intensity reaches the 4 T, in both MT Phases. All quantities on Table 15 are given in millimetres.

The comparison between the repositioning and total displacements, due to the magnetic field forces, of the three Φ quarters, are compatible among them within the errors in both MT Phases.

Φ quarter	75°	255°	315°
$\Delta Z(0)$ Phase I	0.091 ± 0.057	0.070 ± 0.057	0.106 ± 0.057
$\Delta Z(0)$ Phase II	0.029 ± 0.057	0.258 ± 0.057	0.217 ± 0.057
$\Delta Z(0)$ (Ph.II – Ph.I)	-0.062 ± 0.080	0.188 ± 0.080	0.111 ± 0.080
ΔZ_{04T} Phase I	2.069 ± 0.057	2.789 ± 0.057	2.674 ± 0.057
ΔZ_{04T} Phase II	1.793 ± 0.057	2.734 ± 0.057	2.650 ± 0.057
ΔZ_{04T} (Ph.II – Ph.I)	-0.276 ± 0.080	-0.055 ± 0.080	-0.024 ± 0.080

Table 15: Relative displacements along Z between the TP and the ME1/1 chamber measured during both MT phases (see text).

a)



b)

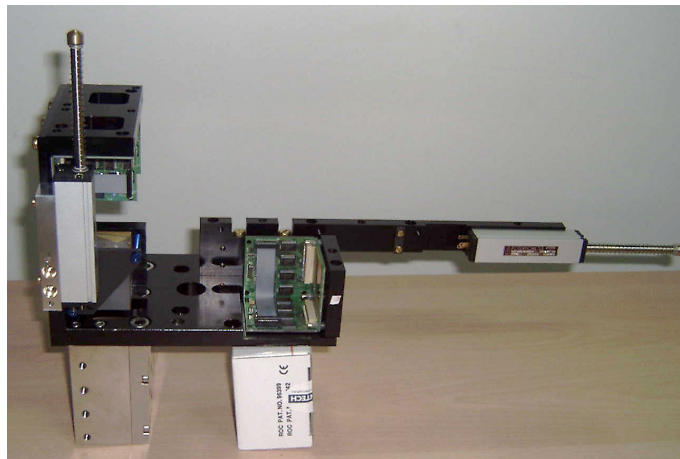


Fig. 29: a) Sketch and b) photograph of a Transfer Plate.

The behaviour of ΔZ , as a function of the magnetic field strength B , is shown in Figs. 30 a) and b) for the Phases I and II respectively. Dots, circles and stars in the plots correspond to the quarters at 75° , 255° and 315° , respectively. Only 1 data point every 100 is plotted in the figures. The curves over data points are fits to the function:

$$\Delta Z = a \times B^3 + b \times B^2 + c \times B + d$$

The fitted parameters are displayed in Table 16.

Observation of Figs. 30 a) and b), and the fitted parameters in Table 16 show that the motions along Z were far to be smooth in both MT Phases. TP and ME/1/1 move apart from each other such that a function of third degree in B is needed to describe the data.

In addition, it is very clear that the 75° quarter moves in a very different manner than quarters at 255° and 315° (in both Phases) denoting probably higher frictions between touching elements at the upper than at the lower CMS structures.

In both Phases, quarters at 255° and 315° behave in similar way and data points and fitted parameters are fairly compatible. However, the compatibility does not exist when comparing the results in both Phases: the motions are not reproduced.

Same incompatibility is observed between the 75° data points in the two MT Phases.

From above results we conclude that, in what the relative displacements between the Transfer Plate and the ME1/1 chamber are concerned, equal magnetic field intensity results in different motions between these two objects. In general, we would say that if a given motion is detected due to a given change of the magnetic field intensity in a given CMS run, the same change in the magnetic field, in a different CMS run, or even in the same run, will result in a non predictable different motion.

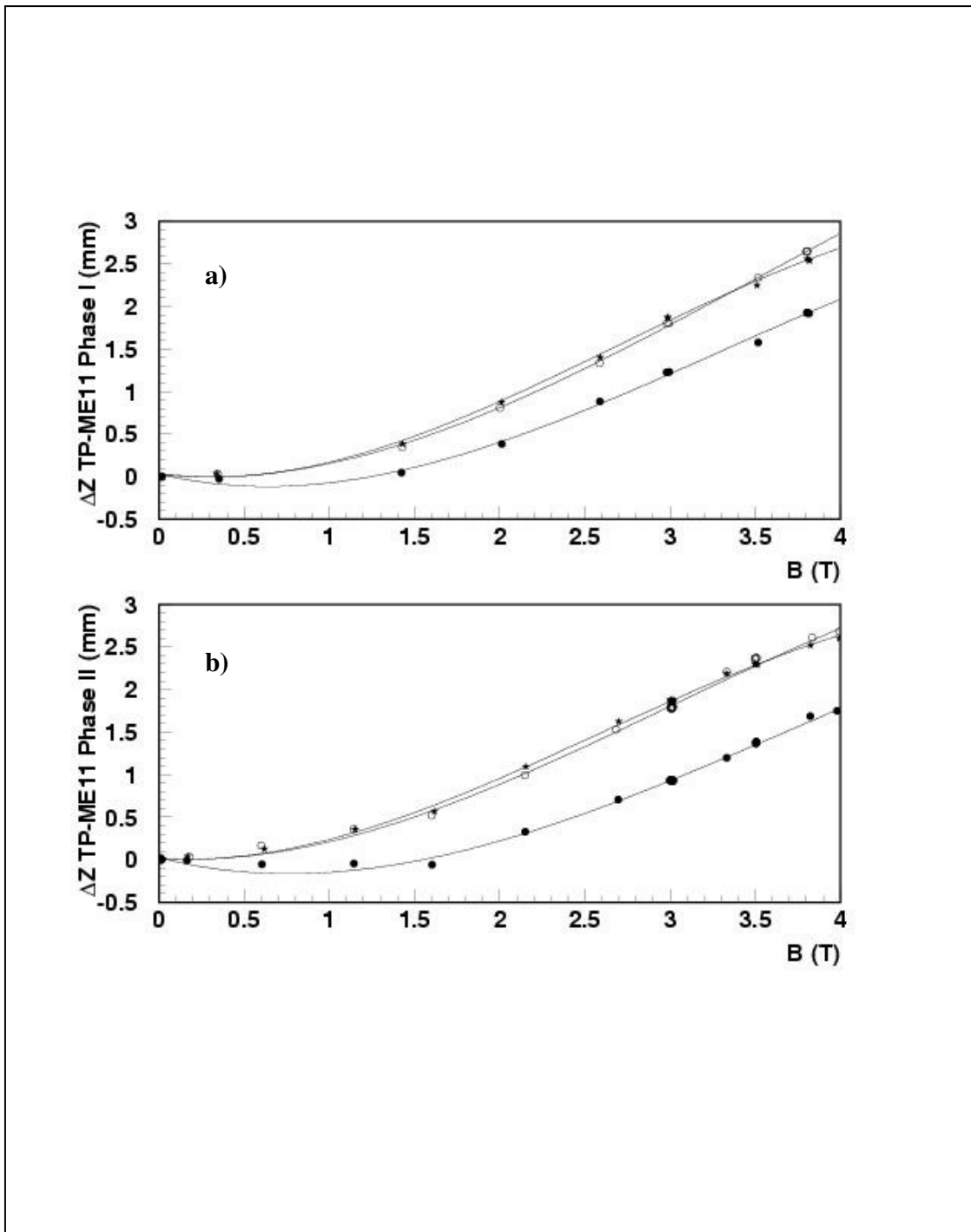


Fig. 30: Data points and fitted curves from the relative displacements between the TP and the ME/1/1 in each of the MT phases. Dots, circles and stars correspond to 75°, 255° and 315° quadrants, respectively.

	a (mm/T ³)	b (mm/T ²)	c (mm/T)	d (mm)	X ² /NDF	Residuals widths (mm)
Phase I 75°	-0.042 ± 0.001	0.417 ± 0.009	-0.479 ± 0.014	0.030 ± 0.006	304/1047	0.031
Phase I 255°	-0.036 ± 0.001	0.374 ± 0.009	-0.214 ± 0.014	0.028 ± 0.006	241/1047	0.027
Phase I 315°	-0.057 ± 0.001	0.463 ± 0.009	-0.275 ± 0.014	0.037 ± 0.006	308/1047	0.031
Phase II 75°	-0.033 ± 0.001	0.369 ± 0.004	-0.506 ± 0.008	0.021 ± 0.002	2303/13996	0.023
Phase II 255°	-0.040 ± 0.001	0.364 ± 0.004	-0.134 ± 0.008	0.019 ± 0.002	1937/13996	0.021
Phase II 315°	-0.052 ± 0.001	0.404 ± 0.004	-0.131 ± 0.008	0.014 ± 0.002	497/13996	0.011

Table 16: Fitted parameters of the relative displacements between the Transfer Plate and the ME/1/1 chamber to the function $\Delta Z = a \times B^3 + b \times B^2 + c \times B + d$ in both MT phases.

8.2.1 Monitoring the axial distance (along Z) between the Transfer Plate and the ME1/1 chamber at the underground and comparison with the MT results

We give in Table 17 the comparison between the measured repositioning, $\Delta Z(0)$, of the chamber with respect to the Transfer Plate after the cycle $B = 0$ T, $B = 4$ T and back to $B = 0$ T, measured by the proximity sensors at both CMS Z sides during the CRAFT run, for two Φ quadrants, 75° and 315° , that we use for illustration and for comparison with the data taken during the MT in the same two quadrants.

Also in Table 17 we display the total displacement ΔZ_{04T} suffered by the TP, with respect to the ME1/1 chamber, from the situation at $B = 0$ T, before starting the ramp up to 4 T, to the values when the magnet intensity reaches the 4 T and we compare the observations between +Z and -Z sides and with the values measured during the two Phases of the MT runs. All quantities are given in millimetres.

Φ quarter	75°	315°
Z- / $\Delta Z(0)$ / CRAFT	-0.011 ± 0.057	0.064 ± 0.057
Z+ / $\Delta Z(0)$ / CRAFT	0.019 ± 0.057	0.099 ± 0.057
Z+ / $\Delta Z(0)$ / MT Phase I	0.091 ± 0.057	0.106 ± 0.057
Z+ / $\Delta Z(0)$ / MT Phase II	0.029 ± 0.057	0.217 ± 0.057
Z- / ΔZ_{04T} / CRAFT	1.630 ± 0.057	2.198 ± 0.057
Z+ / ΔZ_{04T} / CRAFT	1.355 ± 0.057	2.307 ± 0.057
Z+ / ΔZ_{04T} / MT Phase I	2.069 ± 0.057	2.674 ± 0.057
Z+ / ΔZ_{04T} / MT Phase II	1.793 ± 0.057	2.650 ± 0.057

Table 17: Relative displacements along Z between the TP and the ME1/1 chamber, in two quarters at both CMS sides during the CRAFT run and the same relative distances measured during both MT phases.

The repositioning is achieved at $\Phi = 75^\circ$ everywhere. This is not the case for the quarter at 315° at the Z+ side, due, perhaps, to an up/down asymmetry, which is more evident by observing the ΔZ_{04T} values: maximum displacements are always larger (up to 1 mm) at $\Phi = 315^\circ$.

On the other hand the measurements of ΔZ_{04T} at $Z+$ show a more than 5σ disagreement between on and under ground motions.

The behaviour of ΔZ , as a function of the magnetic field strength B , is shown in Fig. 31 where we compare the data on and underground from the CRAFT and MT Phases I and II runs. Dots: CRAFT at $+75^\circ$. Circles: CRAFT at $+315^\circ$. Stars: MT Phase I at $+75^\circ$. Swiss crosses: MT Phase I at $+315^\circ$. White triangles: MT Phase II at $+75^\circ$. Black triangles: MT Phase II at $+315^\circ$. Rhombi: CRAFT at -75° . Squares: CRAFT at -315° .

Only 1 data point every 100 from the MT data and 1 every 10, from the CRAFT data, is plotted in the figure. The parameterization of the data points need in all cases a third degree function in the magnet field intensity B . The curves over data points are therefore fits to the expression:

$$\Delta Z = a \times B^3 + b \times B^2 + c \times B + d$$

The most significant observation from Fig. 31 is that the data at $\pm 315^\circ$ quarters are systematically above the ones belonging to the $\pm 75^\circ$ quarters and that, inside the same quarter, the motion on ground (MT data) are larger than the motions under ground (CRAFT data).

The fitted parameters are displayed in Table 18. Concerning the $\pm 75^\circ$ quarters in the CRAFT data, the fitted values are in complete disagreement between them, as one can also see by inspecting Fig. 31 (dots for $+75^\circ$ and rhombi for -75°). They are also in disagreement with the fitted values in the $+75^\circ$ MT data, Phases I and II, that, on the other hand, agree fairly well between them.

At the $\pm 315^\circ$ quarters, fitted parameters to the CRAFT data agree among them as also do the ones corresponding to the two Phases of the MT data in the $+315^\circ$ quarter. Here, the disagreement between the on and under ground data is not as striking as the one observed for the 75° quarters.

However, the main overall conclusion remains always the same: equal magnetic field intensities produce different motions between the same observed mechanical elements.

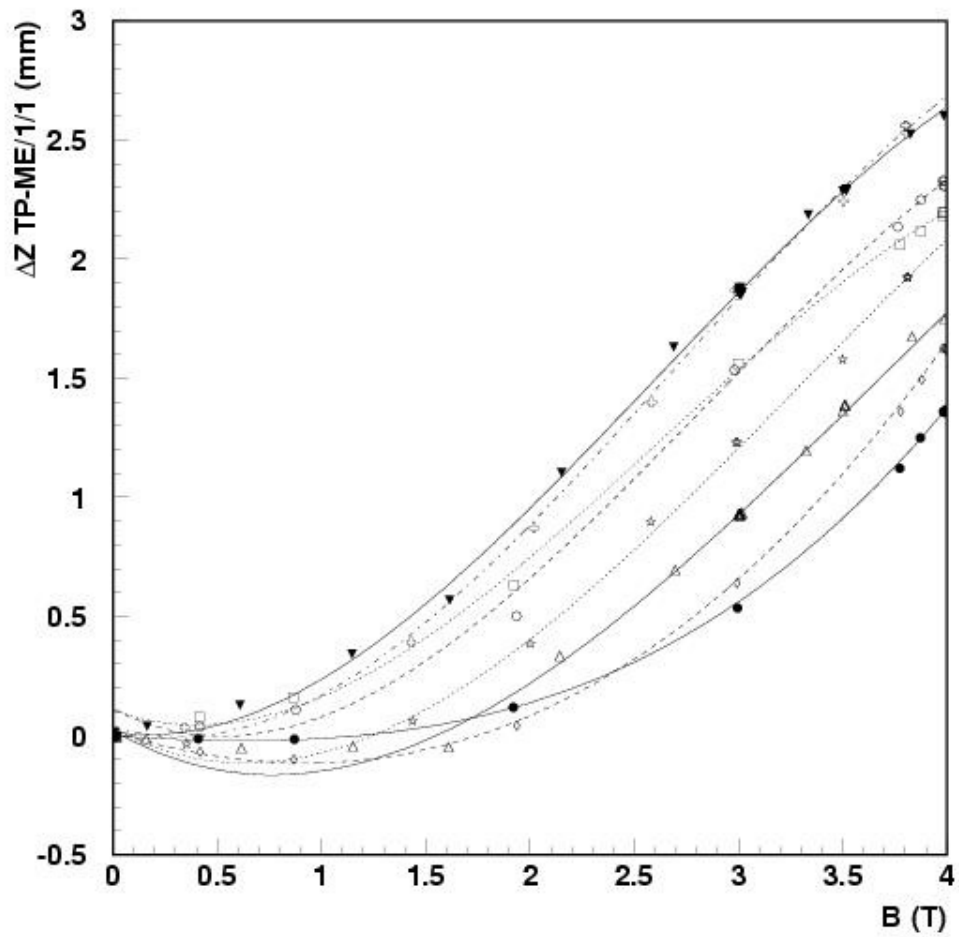


Fig. 31: ΔZ (TP to ME/1/1) as a function of the magnetic field intensity. Dots: CRAFT at $+75^\circ$. Circles: CRAFT at $+315^\circ$. Stars: MT Phase I at $+75^\circ$. Swiss crosses: MT Phase I at $+315^\circ$. White triangles: MT Phase II at $+75^\circ$. Black triangles: MT Phase II at $+315^\circ$. Rhombi: CRAFT at -75° . Squares: CRAFT at -315° .

	a (mm/T ³)	b (mm/T ²)	c (mm/T)	d (mm)	X ² /NDF	Residuals widths (mm)
CRAFT -75°	0.008 ± 0.005	0.141 ± 0.034	-0.280 ± 0.061	0.016 ± 0.025	3/97	0.009
CRAFT +75°	0.019 ± 0.005	0.023 ± 0.034	-0.052 ± 0.061	-0.003 ± 0.025	7/97	0.015
MT Ph. I +75°	-0.042 ± 0.001	0.417 ± 0.009	-0.479 ± 0.014	0.030 ± 0.006	304/1047	0.031
MT Ph.II +75°	-0.033 ± 0.001	0.369 ± 0.004	-0.506 ± 0.008	0.021 ± 0.002	2303/13996	0.023
CRAFT -315°	-0.054 ± 0.005	0.428 ± 0.034	-0.319 ± 0.061	0.106 ± 0.025	34/97	0.031
CRAFT +315°	-0.056 ± 0.005	0.475 ± 0.034	-0.454 ± 0.061	0.112 ± 0.025	44/97	0.038
MT Ph. I +315°	-0.057 ± 0.001	0.463 ± 0.009	-0.275 ± 0.014	0.037 ± 0.006	308/1047	0.031
MT Ph.II +315°	-0.052 ± 0.001	0.404 ± 0.004	-0.131 ± 0.008	0.014 ± 0.002	497/13996	0.011

Table 18: Fitted parameters of the relative displacements between the Transfer Plate and the ME/1/1 chamber to the function $\Delta Z = a \times B^3 + b \times B^2 + c \times B + d$ on and under ground (see text).

Before leaving this subsection we are going to present and compare the ΔZ relative motions between the TPs and their nearest ME/1/1 muon chamber in all twelve quarters during the under ground run.

Figs. 32 and 33 show the relative motions measured in the six quarters at the CMS +Z and -Z side, respectively, as a function of the data number (time). First row displays, in two identical figures, the value of the magnetic field strength at every data taken. All other plots correspond to the relative displacements, in mm, between the TP and the nearest ME/1/1 chamber in the indicated quarter.

As it can be seen, the observed displacements in the quarters 255° and 315° , at both Z CMS sides, are proportionally much larger than in the other three quarters. Therefore, the idea of an up/down asymmetry is again slightly reinforced.

But, it may well happen that the magnetic field and all other forces in presence make that any relative motions between two observed CMS mechanical elements, which is not physically impossible (i.e. two mechanical pieces cannot occupy the same place in the space), is allowed.

Let us now observe (see Table 19) the question of repositioning $\Delta Z(0)$ and maximum measured relative displacement ΔZ_{04T} between each TP and its corresponding ME/1/1 chamber in all the twelve quarters.

Zside and Φ quarter	$\Delta Z(0)$ (mm)	ΔZ_{04T} (mm)
+Z 15°	0.051 ± 0.057	1.741 ± 0.057
+Z 75°	0.019 ± 0.057	1.355 ± 0.057
+Z 135°	0.036 ± 0.057	1.326 ± 0.057
+Z 195°	0.078 ± 0.057	1.683 ± 0.057
+Z 255°	0.103 ± 0.057	2.132 ± 0.057
+Z 315°	0.099 ± 0.057	2.307 ± 0.057
-Z 15°	0.017 ± 0.057	1.681 ± 0.057
-Z 75°	-0.011 ± 0.057	1.630 ± 0.057
-Z 135°	-0.032 ± 0.057	1.777 ± 0.057
-Z 195°	0.039 ± 0.057	1.796 ± 0.057
-Z 255°	0.067 ± 0.057	2.263 ± 0.057
-Z 315°	0.064 ± 0.057	2.198 ± 0.057

Table 19: *Repositioning and maximum displacements measured from the observation of TP and ME/1/1 chamber CMS elements.*

Apart from the remarks already done when looking into Figs. 32 and 33, what we learn in addition is that the negative CMS side shows a better elasticity than the positive side, since initial positions are well retrieved in all six quarters.

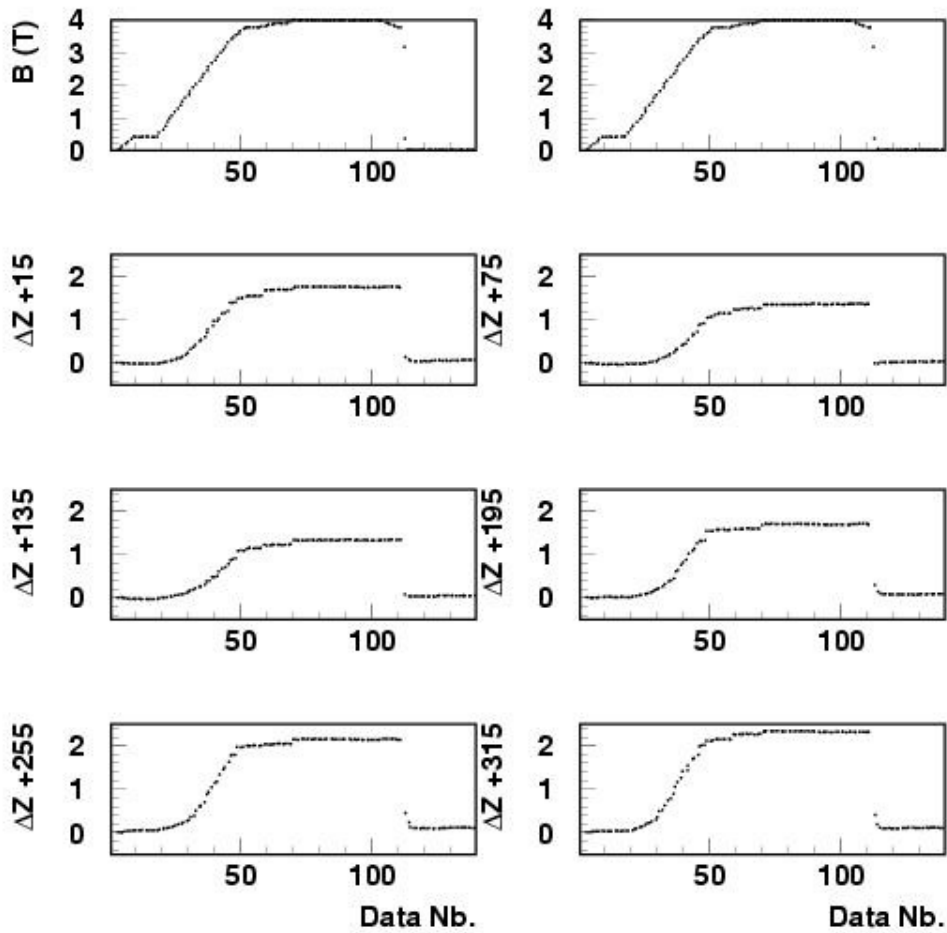


Fig. 32: ΔZ (mm) relative distance measured between the TP and its nearest ME/1/1 chamber, in each of the six quarters at CMS +Z side, as a function of the Data Number. On top two identical plots show the variation of the magnetic field intensity as a function of the Data Number. From CRAFT data.

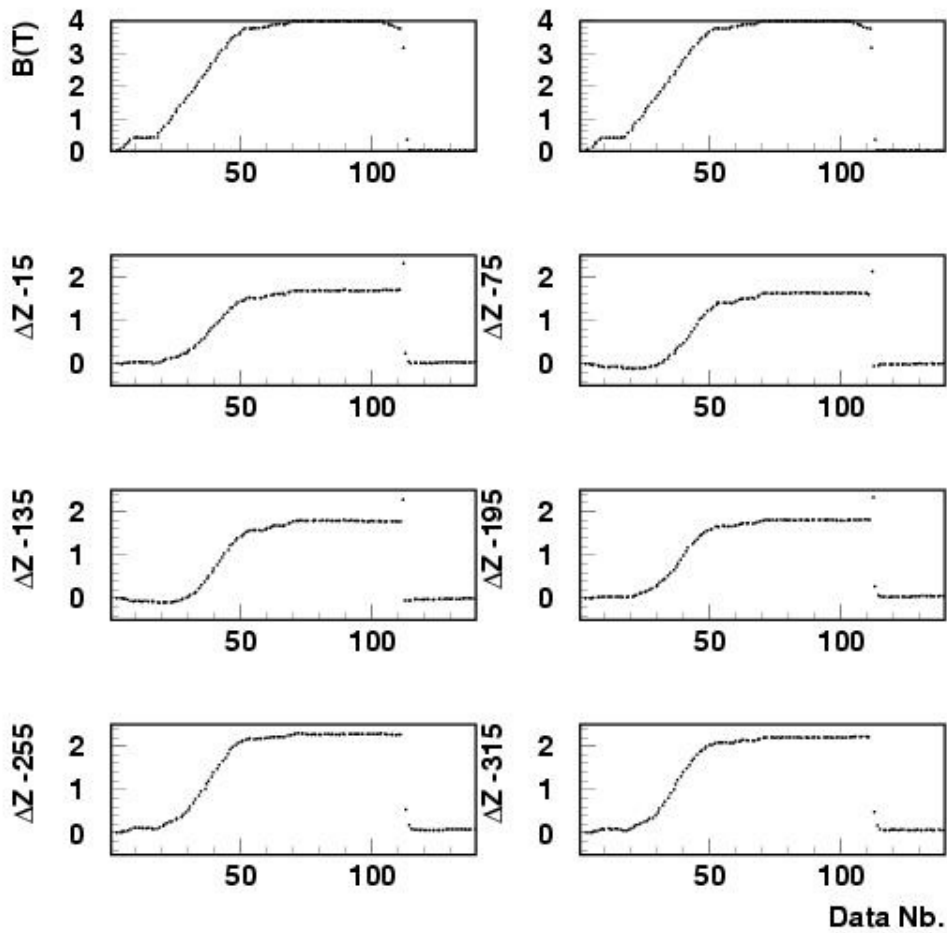


Fig. 33: ΔZ (mm) relative distance measured between the TP and its nearest ME/1/1 chamber, in each of the six quarters at CMS $-Z$ side, as a function of the Data Number. On top two identical plots show the variation of the magnetic field intensity as a function of the Data Number. From CRAFT data.

The behaviour of ΔZ (TP to ME/1/1), as a function of the magnetic field strength B , is shown in Fig. 34 for the CMS +Z side quarters and in Fig. 35 for the CMS -Z side quarters.

In the figures, the $\Phi = 15^\circ$ quarter data is represented by dots. Black squares are for 75° ; black triangles for 135° ; circles represent the 195° quarter data; stars are for 255° and finally, Swiss crosses represent the $\Phi = 315^\circ$ quarter. For clarity, only one data point over ten is plotted.

Inspection of Fig. 34 reveals that the bottom quarters (stars and Swiss crosses) show systematically larger displacements than the top quarters in the CMS +Z side.

Above observation is also true for the CMS -Z side (see Fig. 35), where all three bottom quarters show a systematic larger relative displacements between the TPs and their corresponding ME/1/1 chambers than the three top quarters.

In addition, in quarters $\Phi = 75^\circ$ and 135° (black squares and black triangles, respectively) one observes that prior to the expected motion apart of the two mechanical objects (TP and ME/1/1) they approach to each other up to a B value above 2 T. This behaviour may be due to larger frictions between mechanical elements in the top side of CMS compared with the ones at the bottom quarters. We do not know whether this is due to gravity effects or not.

In all cases the curves over data points are fits to the function:

$$\Delta Z = a \times B^3 + b \times B^2 + c \times B + d$$

The error given to the data points in the fit was 0.057 mm. The fitted parameters are displayed in Table 20. The remarks made from the observation of Figs. 34 and 35 can also be seen when comparing top/bottom and +Z/-Z fitted parameters.

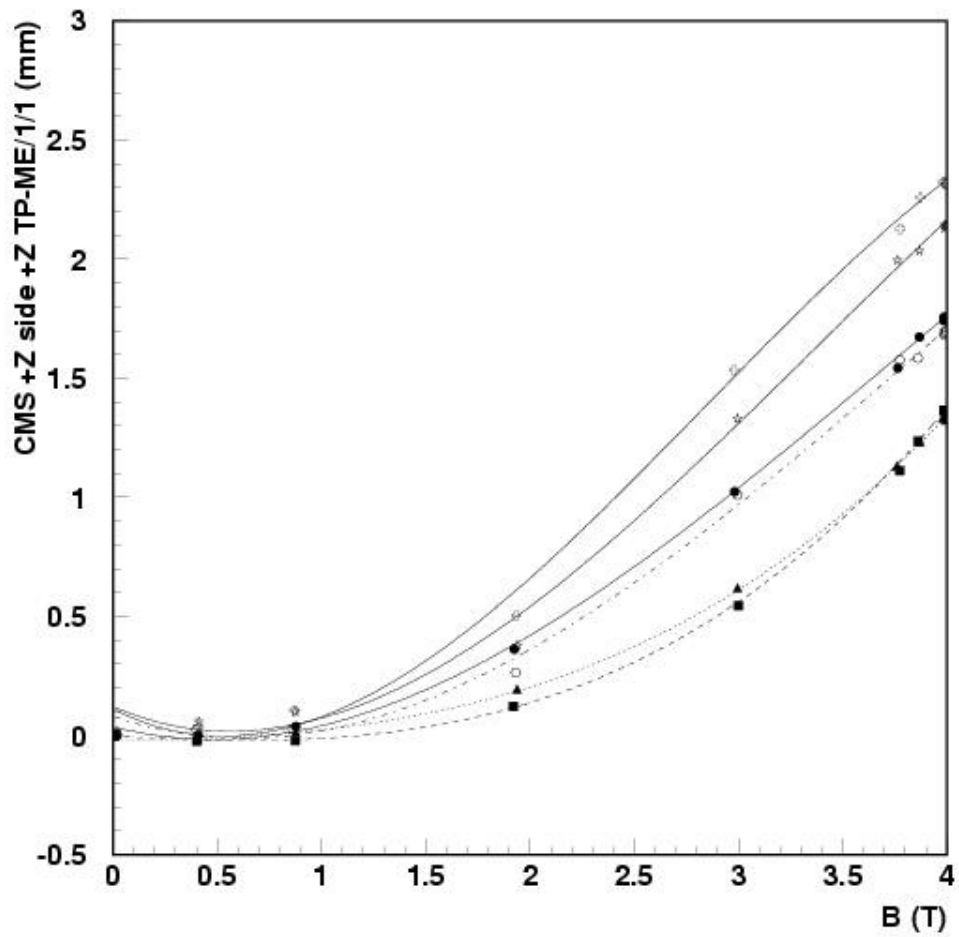


Fig. 34: For the six CMS +Z side quarters, monitored relative distance between the TP and the nearest ME/1/1 muon chamber. Dots: 15°; black squares: 75°; black triangles: 135°; circles: 195°; stars: 255° and Swiss crosses: 315°. From CRAFT data.

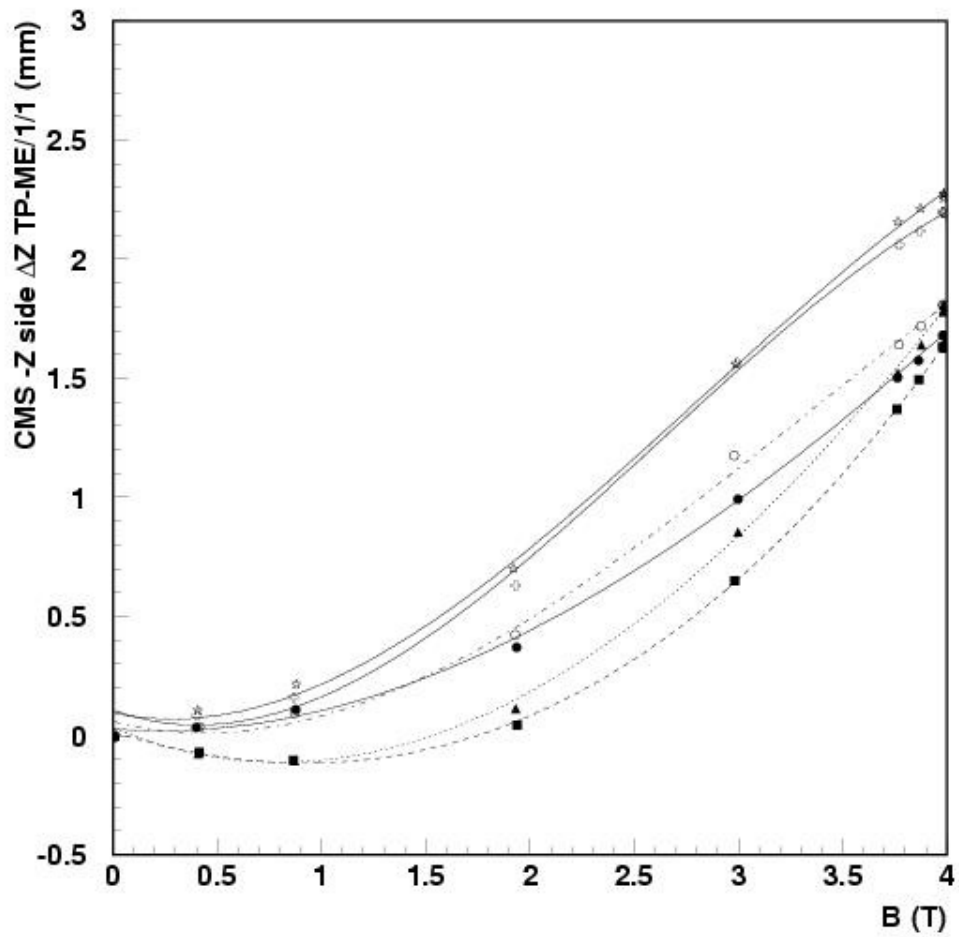


Fig. 35: For the six CMS $-Z$ side quarters, monitored relative distance between the TP and the nearest ME/1/1 muon chamber. Dots: 15° ; black squares: 75° ; black triangles: 135° ; circles: 195° ; stars: 255° and Swiss crosses: 315° . From CRAFT data.

Φ quarter	a (mm/T ³)	b (mm/T ²)	c (mm/T)	d (mm)	X2/NDF	Residuals (mm)
+ 15°	-0.023 ± 0.005	0.256 ± 0.034	-0.230 ± 0.061	0.036 ± 0.025	19/97	0.024
+ 75°	0.019 ± 0.005	0.022 ± 0.034	-0.052 ± 0.061	0.003 ± 0.025	7/97	0.015
+ 135°	0.016 ± 0.005	0.020 ± 0.034	0.009 ± 0.061	-0.021 ± 0.025	9/97	0.017
+ 195°	-0.023 ± 0.005	0.270 ± 0.034	-0.309 ± 0.061	0.081 ± 0.025	37/97	0.034
+ 255°	-0.036 ± 0.005	0.366 ± 0.034	-0.379 ± 0.061	0.121 ± 0.025	57/97	0.043
+ 315°	-0.056 ± 0.005	0.475 ± 0.034	-0.454 ± 0.061	0.112 ± 0.025	44/97	0.038
- 15°	-0.008 ± 0.005	0.155 ± 0.034	-0.070 ± 0.061	0.027 ± 0.025	7/97	0.015
- 75°	-0.008 ± 0.005	0.141 ± 0.034	-0.280 ± 0.061	0.016 ± 0.025	3/97	0.009
- 135°	-0.009 ± 0.005	0.239 ± 0.034	-0.366 ± 0.061	0.032 ± 0.025	7/97	0.015
- 195°	-0.0027 ± 0.005	0.275 ± 0.034	-0.226 ± 0.061	0.059 ± 0.025	15/97	0.022
- 255°	-0.041 ± 0.005	0.350 ± 0.034	-0.190 ± 0.061	0.095 ± 0.025	23/97	0.027
- 315°	-0.054 ± 0.005	0.428 ± 0.034	-0.319 ± 0.061	0.106 ± 0.025	30/97	0.031

Table 20: Fitted parameters of the relative displacements between the Transfer Plate and the ME/1/1 chamber to the function $\Delta Z = a \times B^3 + b \times B^2 + c \times B + d$ in all twelve quarters. From CRAFT data.

8.3 Monitoring the radial ($R\phi$ direction) distance between the Transfer Plate and the ME/1/2 chamber

The monitoring of the relative distance between the TP and the ME/1/2 chamber is done with a Sakae potentiometer sensor located in the transfer plate. The sensor is placed on a support 138.408 mm long and its rod contacts a target located on the bottom of the ME/1/2 chamber (see Fig. 8 for location and Fig. 36 for a view of the sensor support and attach to TP). In that manner, the radial relative distance between the TP and the ME/1/2 will be given by the length of the potentiometer mechanical support plus the short distance measured by the potentiometer [12].

Let us now call R the monitored distance, and let us observe the relative displacement between the two objects during the two MT Phase I and Phase II runs. The comparison between the repositioning ($\Delta R(0)$) of the chamber with respect to the Transfer Plate, measured in Phases I and II, are displayed in the first three rows on Table 21 for the 3 quadrants in Φ (75° , 255° and 315°).

In the last three rows of Table 21 we compare the total displacement (ΔR_{04T}) suffered by the chamber with respect to the TP during the ramp from 0 T to 4 T in each of the MT Phases. As usual, all quantities are given in millimetres.

Φ quadrant	75°	255°	315°
$\Delta R(0)$ Phase I	-0.034 ± 0.057	-0.028 ± 0.057	0.003 ± 0.057
$\Delta R(0)$ Phase II	-0.040 ± 0.057	0.039 ± 0.057	-0.004 ± 0.057
$\Delta R(0)$ (Ph.II – Ph.I)	-0.006 ± 0.080	0.011 ± 0.080	-0.001 ± 0.080
ΔR_{04T} Phase I	3.518 ± 0.057	3.851 ± 0.057	3.729 ± 0.057
ΔR_{04T} Phase II	3.468 ± 0.057	3.735 ± 0.057	3.659 ± 0.057
ΔR_{04T} (Ph.II – Ph.I)	-0.050 ± 0.080	-0.116 ± 0.080	-0.070 ± 0.080

Table 21: Relative displacements along R between the TP and the ME/1/2 chamber measured during both MT phases (see text).

The comparison between the repositioning and total displacements, due to the magnetic field forces, in the three Φ lines for the two MT Phases, are compatible among them within the errors. Repositioning is always compatible with zero in all cases.



Fig. 36: View of the sensor support and attach to the TP for the monitoring of the relative radial distance between the TP and the ME/1/2 chamber.

The behaviour of ΔR as a function of the magnetic field intensity B , is shown in Figs. 37 a) and b) for Phases I and II, respectively. Dots, circles and stars in the plots correspond to the data at quadrants 75° , 255° and 315° , respectively. Only 1 data point every 100 is plotted in the figures. The curves over the data points are fits to the function:

$$\Delta R = a \times B^2 + b \times B + c$$

The fitted parameters are displayed in Table 22.

TP-ME/1/2	a (mm/T ²)	b (mm/T)	c (mm)	χ^2 /NDF	Residuals widths (mm)
Phase I 75°	0.199 ± 0.001	0.090 ± 0.005	0.004 ± 0.005	61/1597	0.011
Phase I 255°	0.151 ± 0.001	0.354 ± 0.005	-0.008 ± 0.005	97/1597	0.014
Phase I 315°	0.163 ± 0.001	0.284 ± 0.005	-0.030 ± 0.005	115/1597	0.015
Phase II 75°	0.173 ± 0.001	0.178 ± 0.002	0.001 ± 0.002	1698/13997	0.020
Phase II 255°	0.141 ± 0.001	0.355 ± 0.002	0.026 ± 0.002	2117/13997	0.022
Phase II 315°	0.148 ± 0.001	0.311 ± 0.002	0.001 ± 0.002	1102/13997	0.016

Table 22: Fitted parameters of the relative displacements between the Transfer Plate and the ME/1/2 chamber to the function $\Delta Z = a \times B^2 + b \times B + c$ in both MT phases.

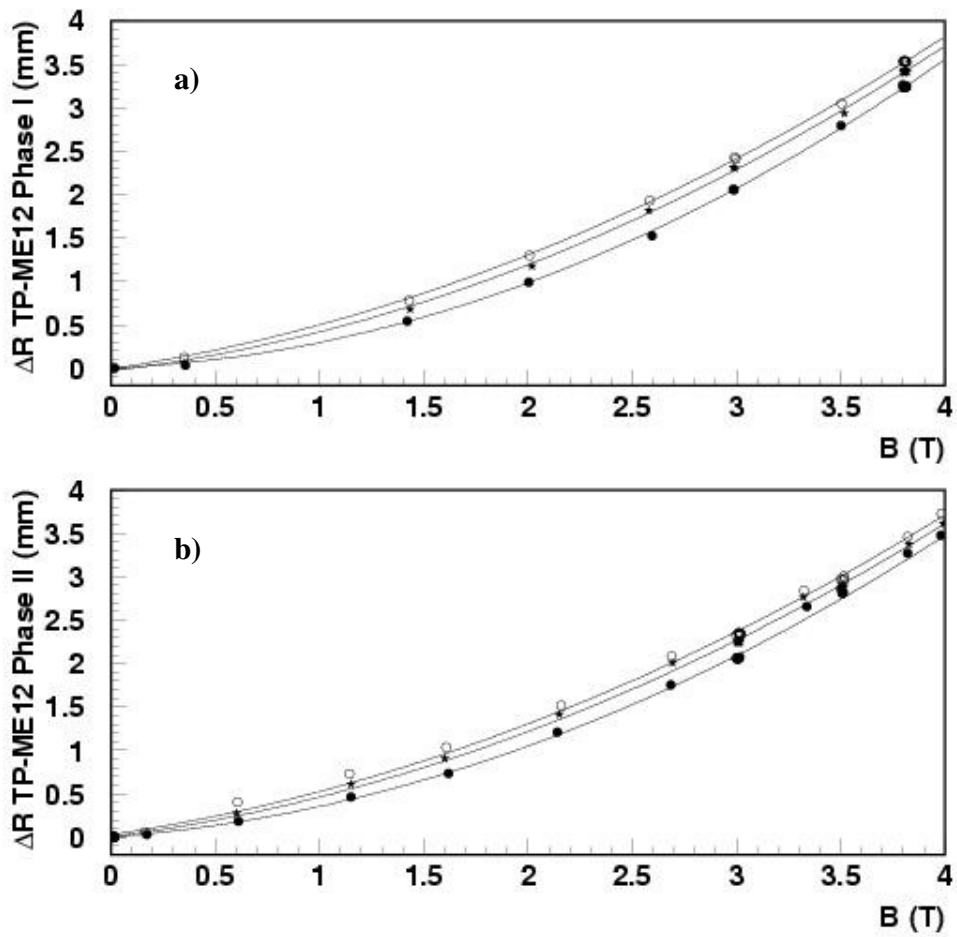


Fig. 37: Data points and fitted curves from the relative radial displacements between the TP and the ME/1/2 chamber in each of the MT phases. Dots, circles and stars correspond to 75°, 255° and 315° quadrants, respectively.

Observation of Table 22 and Figs. 37 a) and b) shows, for this relative displacement, similar behaviours in the three Φ quadrants in each Phase. TP and ME/1/2 move apart, as the magnetic field increases, in a quite smooth way.

However, in the monitoring of this radial relative distance, we also observe a difference in the behaviour of the quadrant at 75° with respect the other two, and this, in both MT Phases.

8.3.1 Monitoring the radial distance (along $R\Phi$) between the Transfer Plate and the ME/1/2 chamber at the underground and some comparisons with the on ground measurements

In Table 23 we give the comparison between the measured repositioning, $\Delta R(0)$, of the chamber with respect to the Transfer Plate, measured by the proximity sensors at both CMS Z sides during the CRAFT run, for two Φ quadrants, 75° and 315° , that we use for illustration and comparison with the data taken during the MT in the same two quadrants.

Also in Table 23 we display the total displacement ΔR_{04T} suffered by the TP, with respect to the ME1/2 chamber, and we compare the observations between +Z and -Z sides and with the values measured during the two Phases of the MT runs. All quantities on Table 23 are given in millimetres.

The repositioning is achieved everywhere, on and under ground. In addition, all ΔR_{04T} values on and under ground agree within 2σ (0.114 mm). However, a slight top/bottom asymmetry is observed: in both, on and under ground data: the total displacements observed are larger in the 315° quarter than in the 75° one.

The behaviour of ΔR , as a function of the magnetic field strength B, is shown in Fig. 38 where we compare the data on and under ground from the CRAFT and MT Phases I and II runs. Dots: CRAFT at $+75^\circ$. Circles: CRAFT at $+315^\circ$. Stars: MT Phase I at $+75^\circ$. Swiss crosses: MT Phase I at $+315^\circ$. White triangles: MT Phase II at $+75^\circ$. Black triangles: MT Phase II at $+315^\circ$. Rhombi: CRAFT at -75° . Squares: CRAFT at -315° . As said the sign given to the Φ quadrants only refers to the CMS Z side.

Only 1 data point every 100 from the MT data and 1 every 10, from the CRAFT data, is plotted in the figure. The curves over data points are fits to the function:

$$\Delta R = a \times B^2 + b \times B + c$$

Φ quarter	75°	315°
$Z- / \Delta R(0) / \text{CRAFT}$	-0.045 ± 0.057	0.030 ± 0.057
$Z+ / \Delta R(0) / \text{CRAFT}$	0.020 ± 0.057	0.046 ± 0.057
$Z+ / \Delta R(0) / \text{MT Phase I}$	-0.034 ± 0.057	0.003 ± 0.057
$Z+ / \Delta R(0) / \text{MT Phase II}$	-0.040 ± 0.057	-0.004 ± 0.057
$Z- / \Delta R_{04T} / \text{CRAFT}$	3.351 ± 0.057	3.562 ± 0.057
$Z+ / \Delta R_{04T} / \text{CRAFT}$	3.318 ± 0.057	3.525 ± 0.057
$Z+ / \Delta R_{04T} / \text{MT Phase I}$	3.518 ± 0.057	3.729 ± 0.057
$Z+ / \Delta R_{04T} / \text{MT Phase II}$	3.468 ± 0.057	3.659 ± 0.057

Table 23: *Relative displacements along R between the TP and the ME1/2 chamber, in two quarters at both CMS sides during the CRAFT run and the same relative distances measured during both MT phases.*

The most significant observation from Fig. 38 is that the data at $\pm 315^\circ$ quarters are systematically above the ones belonging to the $\pm 75^\circ$ quarters and that, inside the same quarter, the motion on ground (MT data) are larger than the motions under ground (CRAFT data).

The fitted parameters are displayed in Table 24. Concerning the $\pm 75^\circ$ quarters in the CRAFT data, the fitted values are in complete disagreement between them, as one can also see by inspecting Fig. 36 (dots for $+75^\circ$ and rhombi for -75°). They are also in disagreement with the fitted values in the $+75^\circ$ MT data, Phases I and II, that, on the other hand, agree fairly well between them.

At the $\pm 315^\circ$ quarters, fitted parameters to the CRAFT data agree among them as also do the ones corresponding to the two Phases of the MT data in the $+315^\circ$ quarter. Here, again, the disagreement between the on and under ground data is not as striking as the one observed for the 75° quarters.

However, the main overall conclusion remains always the same: equal magnetic field intensities produce different motions between the same observed mechanical elements.

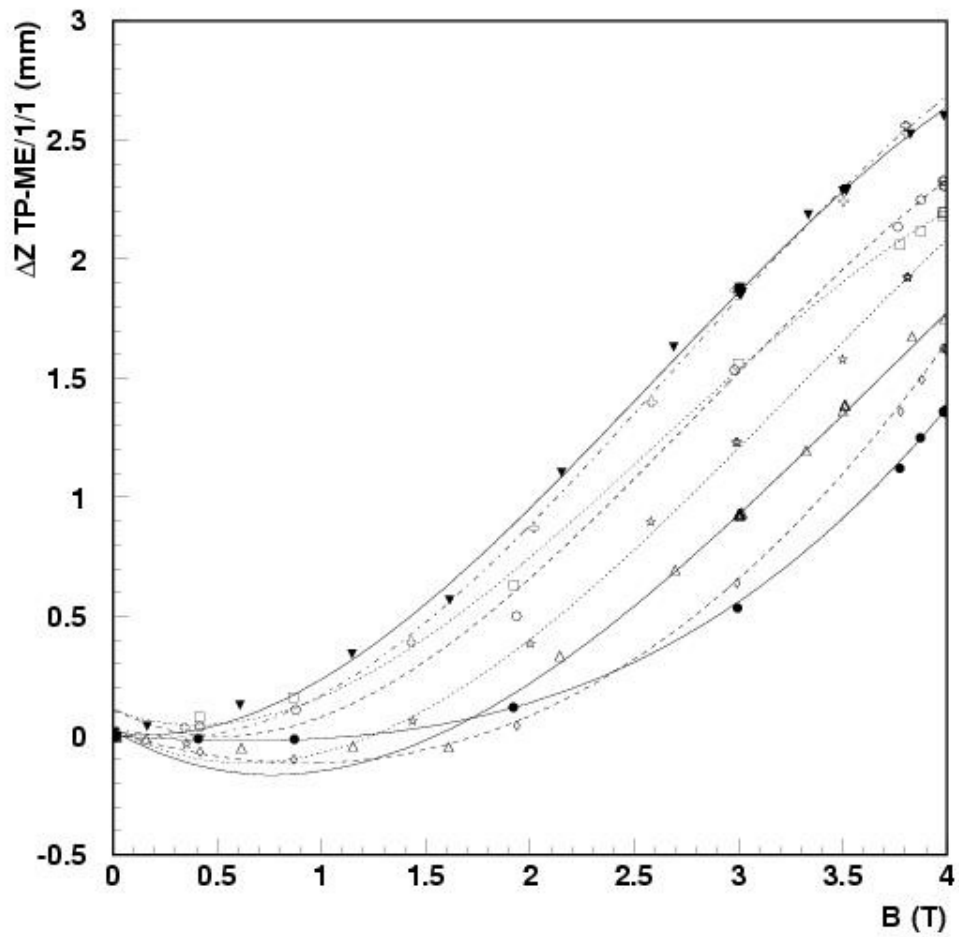


Fig. 38: ΔR (TP to ME/1/2) as a function of the magnetic field intensity. Dots: CRAFT at $+75^\circ$. Circles: CRAFT at $+315^\circ$. Stars: MT Phase I at $+75^\circ$. Swiss crosses: MT Phase I at $+315^\circ$. White triangles: MT Phase II at $+75^\circ$. Black triangles: MT Phase II at $+315^\circ$. Rhombi: CRAFT at -75° . Squares: CRAFT at -315° .

	a (mm/T ²)	b (mm/T)	c (mm)	X ² /NDF	Residuals widths (mm)
CRAFT -75°	0.008 ± 0.005	0.141 ± 0.034	-0.280 ± 0.061	3/97	0.009
CRAFT +75°	0.019 ± 0.005	0.023 ± 0.034	-0.052 ± 0.061	7/97	0.015
MT Ph. I +75°	-0.042 ± 0.001	0.417 ± 0.009	-0.479 ± 0.014	304/1047	0.031
MT Ph.II +75°	-0.033 ± 0.001	0.369 ± 0.004	-0.506 ± 0.008	2303/13996	0.023
CRAFT -315°	-0.054 ± 0.005	0.428 ± 0.034	-0.319 ± 0.061	34/97	0.031
CRAFT +315°	-0.056 ± 0.005	0.475 ± 0.034	-0.454 ± 0.061	44/97	0.038
MT Ph. I +315°	-0.057 ± 0.001	0.463 ± 0.009	-0.275 ± 0.014	308/1047	0.031
MT Ph.II +315°	-0.052 ± 0.001	0.404 ± 0.004	-0.131 ± 0.008	497/13996	0.011

Table 24: *Fitted parameters of the relative displacements between the Transfer Plate and the ME/12 chamber to the function $\Delta Z = a \times B^2 + b \times B + c$ on and under ground (see text).*

Before leaving this subsection we are going to present and compare the ΔR relative motions between the TPs and their nearest ME/1/2 muon chamber in all twelve quarters during the under ground run.

Figs. 39 and 40 show the relative motions measured in the six quarters at the CMS +Z and -Z sides, respectively, as a function of the data number (time). First row displays, in two identical figures, the value of the magnetic field strength at every data taken. All other plots correspond to the relative displacements, in mm, between the TP and the nearest ME/1/2 chamber in the indicated Φ quarter and Z side.

All measured displacements are fairly the same in all six quarters at both Z sides.

Let us now observe (see Table 25) the question of repositioning $\Delta R(0)$ and maximum measured relative displacement ΔR_{04T} between each TP and its corresponding ME/1/2 chamber in all the twelve quarters.

Zside and Φ quarter	$\Delta R(0)$ (mm)	ΔR_{04T} (mm)
+Z 15°	0.027 ± 0.057	3.254 ± 0.057
+Z 75°	0.020 ± 0.057	3.318 ± 0.057
+Z 135°	0.032 ± 0.057	3.278 ± 0.057
+Z 195°	0.032 ± 0.057	3.194 ± 0.057
+Z 255°	0.037 ± 0.057	3.617 ± 0.057
+Z 315°	0.046 ± 0.057	3.525 ± 0.057
-Z 15°	0.026 ± 0.057	3.571 ± 0.057
-Z 75°	-0.045 ± 0.057	3.351 ± 0.057
-Z 135°	-0.029 ± 0.057	3.318 ± 0.057
-Z 195°	0.011 ± 0.057	3.237 ± 0.057
-Z 255°	0.007 ± 0.057	3.289 ± 0.057
-Z 315°	0.020 ± 0.057	3.562 ± 0.057

Table 25: *Repositioning and maximum displacements measured from the observation of TP and ME/1/2 chamber CMS elements. From CRAFT data.*

The first observation from the table is that the two elements retrieve the initial positions, within one standard deviation in all twelve quarters. Maximum measured displacement, ΔR_{04T} are also in good agreement between Φ quarters and CMS Z sides.

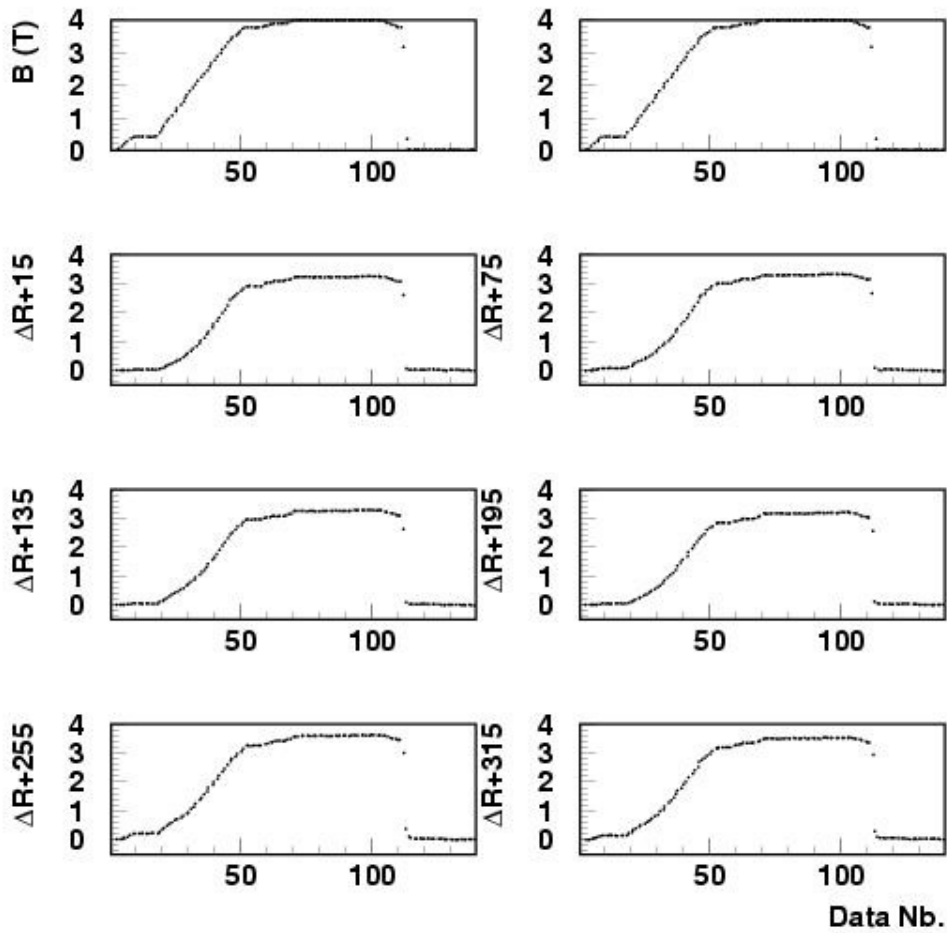


Fig. 39: ΔR (mm) relative distance measured between the TP and its nearest ME/1/2 chamber, in each of the six quarters at CMS +Z side, as a function of the Data Number. On top two identical plots show the variation of the magnetic field intensity as a function of the Data Number. From CRAFT data.

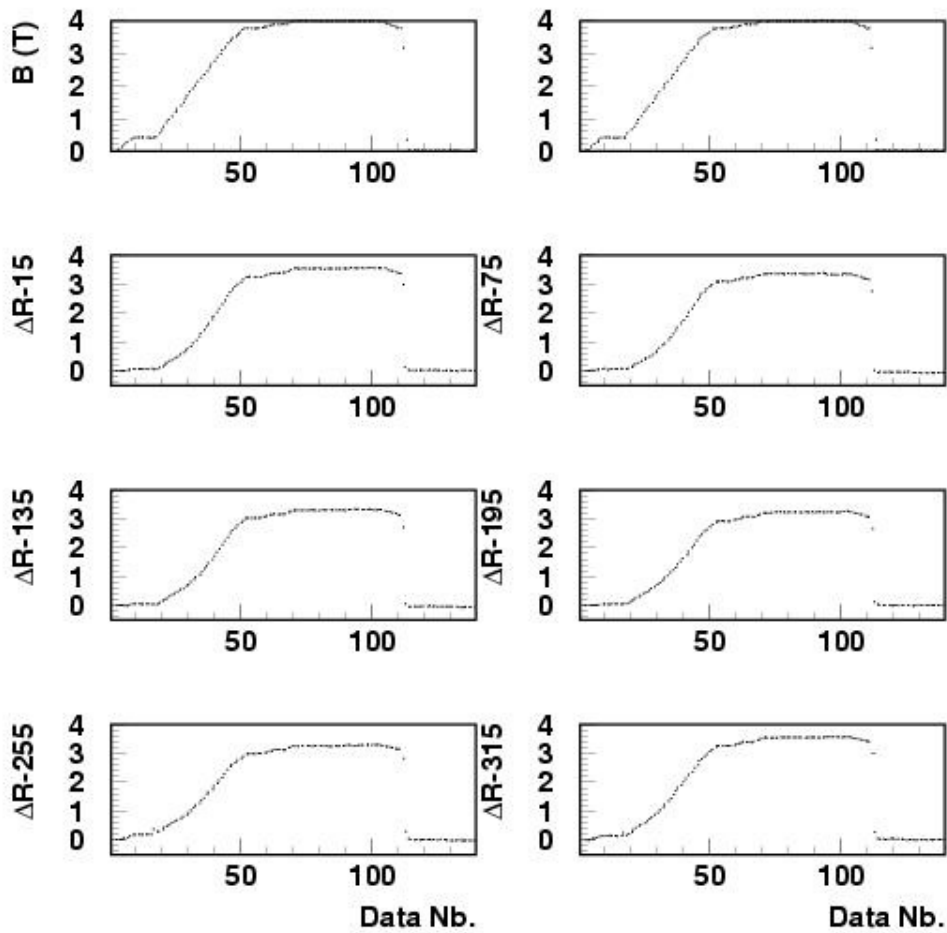


Fig. 40: ΔR (mm) relative distance measured between the TP and its nearest ME/1/2 chamber, in each of the six quarters at CMS $-Z$ side, as a function of the Data Number. On top two identical plots show the variation of the magnetic field intensity as a function of the Data Number. From CRAFT data.

The behaviour of ΔR (TP to ME/1/2), as a function of the magnetic field strength B , is shown in Fig. 41 for the CMS +Z side quarters and in Fig. 42 for the CMS -Z side quarters.

In the figures, the 15° quarter data is represented by dots. Black squares are for $\Phi = 75^\circ$; black triangles for 135° ; circles represent the 195° quarter data; stars are for 255° and finally, Swiss crosses represent the $\Phi = 315^\circ$ quarter. For clarity, only one data point over ten is plotted.

Inspection of Fig. 41 reveals that the bottom quarters (stars and Swiss crosses) show systematically larger displacements than the top quarters in the CMS +Z side. This observation was also seen when analysing of the ΔZ (TP - ME/1/1) data.

At the CMS -Z side (see Fig. 42), the quarter at $\Phi = -255^\circ$ (stars in the figure) does not follow the general trend.

In all cases the curves over data points are fits to the function:

$$\Delta R = a \times B^2 + b \times B + c$$

The error given to the data points in the fit was 0.057 mm. The fitted parameters are displayed in Table 26. The remarks made from the observation of Figs. 41 and 42 can also be seen when comparing the fitted parameters.

It is interesting to note that, on both CMS sides, the fits are very good and reveal an strong quadratic behaviour with the magnetic field intensity, a negligible constant term (good repositioning) and residuals smaller than 50 μm .

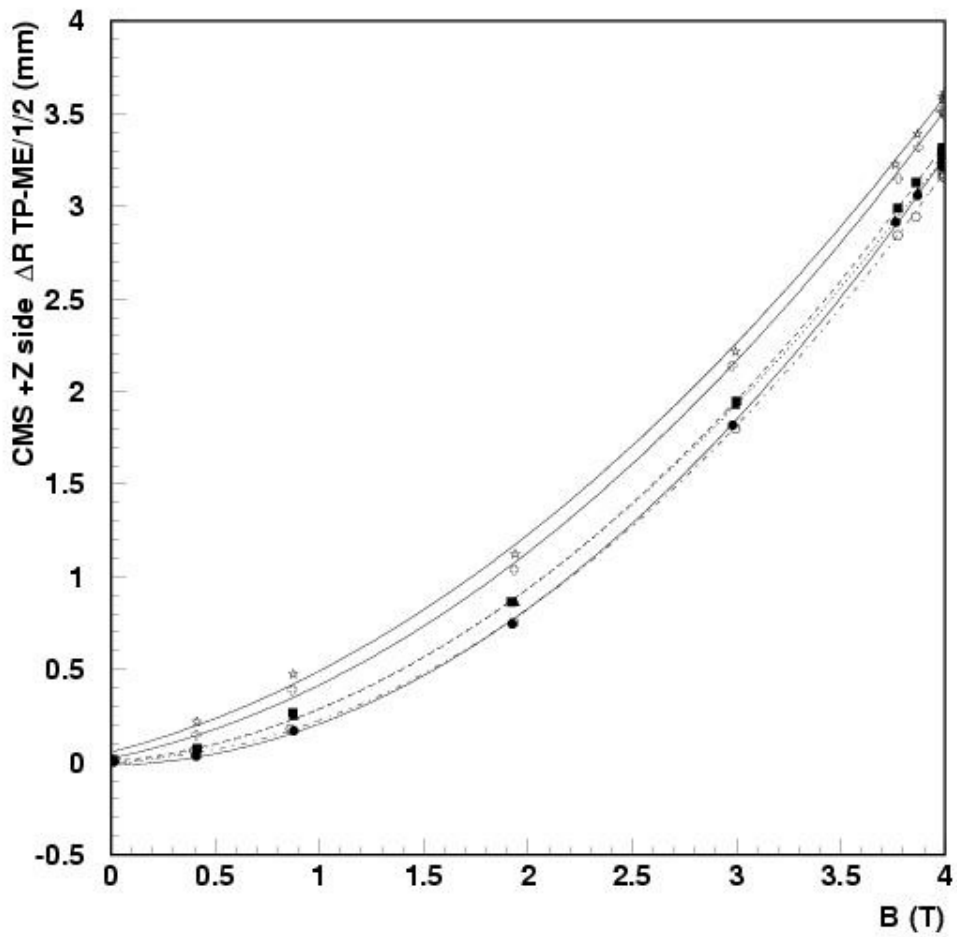


Fig. 41: For the six CMS +Z side quarters, monitored relative distance between the TP and the nearest ME/1/2 muon chamber. Dots: 15°; black squares: 75°; black triangles: 135°; circles: 195°; stars: 255° and Swiss crosses: 315°.

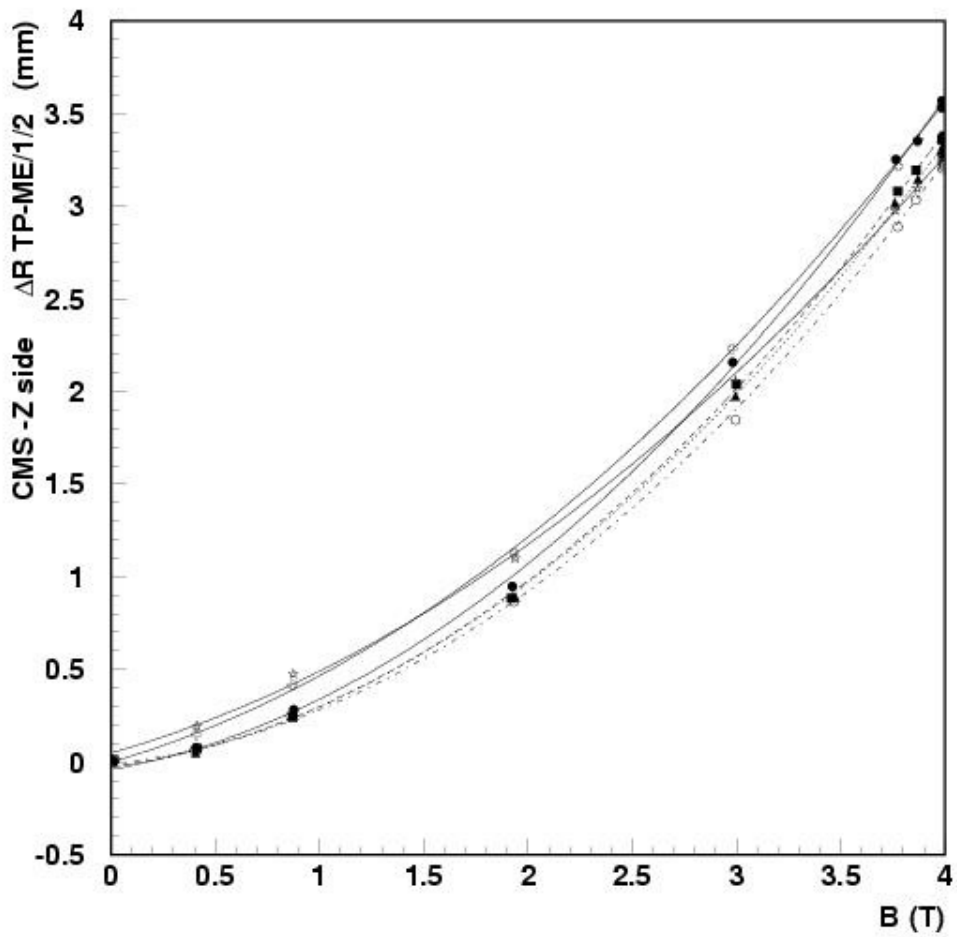


Fig. 42: For the six CMS $-Z$ side quarters, monitored relative distance between the TP and the nearest ME/1/2 muon chamber. Dots: 15° ; black squares: 75° ; black triangles: 135° ; circles: 195° ; stars: 255° and Swiss crosses: 315° .

Φ quarter	a (mm/T ²)	b (mm/T)	c (mm)	χ^2 /NDF	Residuals (mm)
+ 15°	0.199 ± 0.005	0.025 ± 0.022	-0.019 ± 0.018	7/98	0.015
+ 75°	0.184 ± 0.005	0.098 ± 0.022	0.003 ± 0.018	8/98	0.016
+ 135°	0.174 ± 0.005	0.127 ± 0.022	-0.015 ± 0.018	8/98	0.016
+ 195°	0.192 ± 0.005	0.026 ± 0.022	0.004 ± 0.018	10/98	0.018
+ 255°	0.149 ± 0.005	0.289 ± 0.022	0.052 ± 0.018	32/98	0.032
+ 315°	0.159 ± 0.005	0.237 ± 0.022	0.018 ± 0.018	11/98	0.019
- 15°	0.176 ± 0.005	0.204 ± 0.022	-0.043 ± 0.018	12/98	0.019
- 75°	0.178 ± 0.005	0.147 ± 0.022	-0.028 ± 0.018	14/98	0.021
- 135°	0.172 ± 0.005	0.156 ± 0.022	-0.030 ± 0.018	7/98	0.015
- 195°	0.173 ± 0.005	0.118 ± 0.022	-0.011 ± 0.018	8/98	0.016
- 255°	0.122 ± 0.005	0.320 ± 0.022	0.047 ± 0.018	31/98	0.032
- 315°	0.142 ± 0.005	0.325 ± 0.022	-0.002 ± 0.018	9/98	0.017

Table 26: Fitted parameters of the relative displacements between the Transfer Plate and the ME/1/2 chamber to the function $\Delta Z = a \times B^2 + b \times B + c$ in all twelve quarters.

8.4 Monitoring the radial distance between the MAB structure and the ME1/2 chamber during the MT runs

The monitoring of the relative distance ($R\phi$ direction) between the external muon barrel MAB and the ME1/2 chamber is done with a non contact Omron [13] sensor located at the bottom place of each MAB structure. The sensor is placed on a support 125.972 mm long and its emitting/receiving head directs a laser light and receives the reflected light to/from a target located on the top region of the ME1/2 chamber (see Fig. 8 for location). In that manner, the radial relative distance, in a given Φ quadrant, between the MAB and its nearest ME1/2 chamber will be given by the length of the Omron mechanical support plus the short distance measured by the non contact optical sensor [13].

During the Phase I of the Magnet Test, the sensor located in the MAB at 75° was not pointing properly to its target and we will not use that data.

Being R the monitored distance, let us first observe the relative displacement between the two objects, MAB and ME1/2 during the MT. The comparison between the repositioning ($\Delta R(0)$) of the chamber with respect to the Transfer Plate, measured with the corresponding optical sensors, in Phases I and II, are displayed in the first three rows on Table 27, for the three Φ quadrants (75° , 255° and 315°).

On the same Table 27 (last three rows) we compare the total displacement (ΔR_{04T}) suffered by the chamber with respect to the TP during the ramp from 0 T to 4 T in both MT Phases. As usual, all quantities in the Table are given in millimetres.

The comparisons between the computed values for repositioning show a quite elastic behaviour in both MT Phases. The total displacements, due to the magnetic field forces, in the two Φ regions we can compare, are absolutely compatible among them.

Concerning the analysis of displacements as a function of the magnetic field intensity, we show in Figs. 43 a) and b) the values of $\Delta R(B)$ as a function of B for the two working Φ quadrants in Phases I and the three of Phase II, respectively. Data points are fitted to a function of the type:

$$\Delta R = a \times B^2 + b \times B + c$$

The fitted parameters are given in Table 28. The imposed theoretical error for DR in the X^2 fit was 0.057 mm.

Data points and fitted curves are represented in Fig. 43. Dots, circles and stars, in the figure, correspond to the Φ quarters at 75° , 255° and 315° data, respectively.

Φ quadrant	75°	255°	315°
$\Delta R(0)$ Phase I	---	0.0022 ± 0.057	0.000 ± 0.057
$\Delta R(0)$ Phase II	-0.0073 ± 0.057	-0.057 ± 0.057	-0.198 ± 0.057
$\Delta R(0)$ (Ph.II – Ph.I)	---	-0.079 ± 0.080	-0.198 ± 0.080
ΔR_{04T} Phase I	---	-2.757 ± 0.057	-2.820 ± 0.057
ΔR_{04T} Phase II	-3.464 ± 0.057	-2.806 ± 0.057	-2.865 ± 0.057
ΔR_{04T} (Ph.II – Ph.I)	---	-0.049 ± 0.080	-0.045 ± 0.080

Table 27: Relative displacements along R between the MAB and the ME/1/2 chamber measured during both MT phases (see text).

	a (mm/T ²)	b (mm/T)	c (mm)	χ^2/NDF	Residuals widths (mm)
Phase I 255°	-0.107 ± 0.001	-0.273 ± 0.006	0.004 ± 0.053	44/1048	0.012
Phase I 315°	-0.118 ± 0.001	-0.247 ± 0.006	0.003 ± 0.053	20/1048	0.008
Phase II 75°	-0.155 ± 0.001	-0.233 ± 0.002	-0.003 ± 0.002	1654/13997	0.020
Phase II 255°	-0.121 ± 0.001	-0.216 ± 0.002	0.001 ± 0.002	1226/13997	0.017
Phase II 315°	-0.124 ± 0.001	-0.209 ± 0.002	-0.022 ± 0.002	1007/13997	0.015

Table 28: Fitted parameters of the relative displacements between the MAB and the ME/1/2 chamber to the function $\Delta R = a \times B^2 + b \times B + c$ in both MT phases.

The observation of Figs. 43 a) and b) and the fitted parameters in Table 28 show that, in both phases of the magnet test, the behaviour of the relative radial displacement between each MAB and its corresponding ME/1/2 chamber, from the two working lines was quite similar.

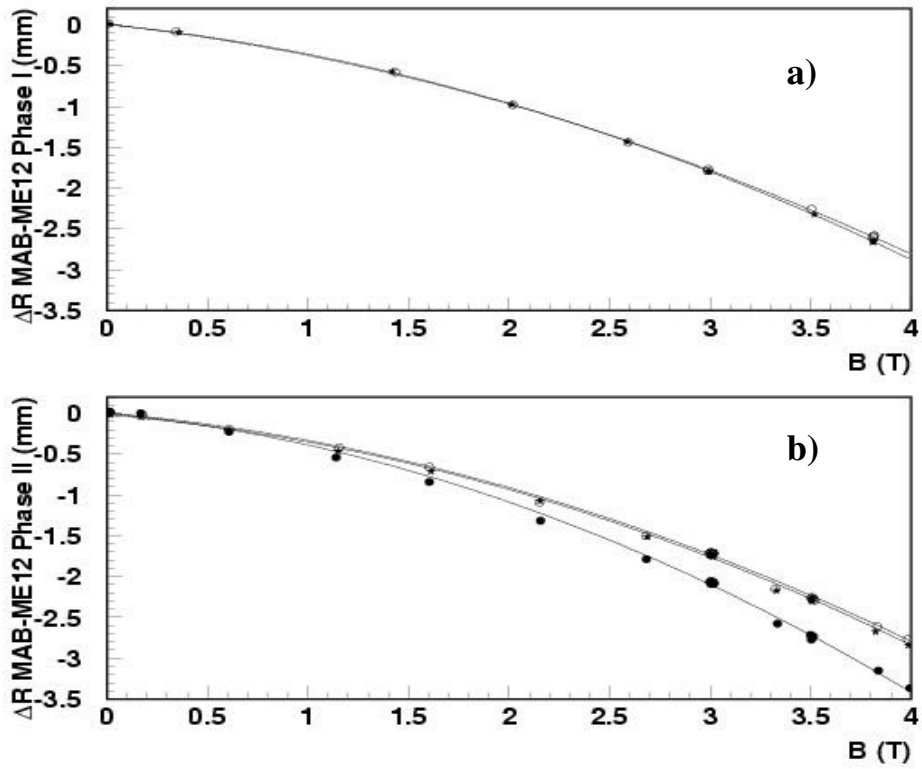


Fig. 43: Data points and fitted curves from the relative radial displacements between the MAB and the ME/1/2 chamber in each of the MT phases. Dots, circles and stars correspond to 75° , 255° and 315° quadrants, respectively.

However, as already seen when analysing previous distances monitoring, we observe that equal magnetic field intensity results in different motions between the observed objects, when Phase I and Phase II results are compared.

8.4.1 Monitoring the radial distance (along $R\Phi$) between the MAB and the ME1/2 chamber at the underground and some comparisons with the on ground measurements

During the CRAFT run all six Omrons were badly positioned at $-Z$ side and all the six signals were saturating. In addition, at the $\Phi = 75^\circ$ quarter at $+Z$ side, the sensor was giving no signal.

Following the conventions in Table 27, we give in Table 29 the comparison between the measured repositioning, $\Delta R(0)$, of the chamber with respect to the corresponding MAB, measured by the proximity sensors during the CRAFT run and the MT runs, for the two $+Z$ CMS side Φ quadrants 255° and 315° .

Also in Table 29 we display the total displacement ΔR_{04T} suffered by the MAB, with respect to the ME1/2 chamber, from $B = 0$ T and $B = 4$ T and we compare the observations between $+Z$ and $-Z$ sides and with the values measured during the two Phases of the MT runs. All quantities on Table 29 are given in millimetres.

The repositioning is achieved everywhere, on and under ground, within 3σ . All ΔR_{04T} values on and under ground also agree within 3σ (± 0.171 mm).

The behaviour of ΔR , as a function of the magnetic field strength B , is shown in Fig. 44 where we compare the data on and under ground from the CRAFT and MT Phases I and II runs. Dots: CRAFT at $+255^\circ$. Circles: CRAFT at $+315^\circ$. Stars: MT Phase I at $+255^\circ$. Swiss crosses: MT Phase I at $+315^\circ$. White triangles: MT Phase II at $+255^\circ$. Black triangles: MT Phase II at $+315^\circ$.

Only 1 data point every 100 from the MT data and 1 every 10, from the CRAFT data, is plotted in the figure. The curves over data points are fits to the function:

$$\Delta R = a \times B^2 + b \times B + c$$

Φ quarter	255°	315°
$\Delta R(0) / \text{CRAFT}$	0.127 ± 0.057	0.025 ± 0.057
$\Delta R(0) / \text{MT Phase I}$	-0.002 ± 0.057	0.000 ± 0.057
$\Delta R(0) / \text{MT Phase II}$	-0.057 ± 0.057	-0.198 ± 0.057
$\Delta R_{04T} / \text{CRAFT}$	-2.563 ± 0.057	-3.043 ± 0.057
$\Delta R_{04T} / \text{MT Phase I}$	-2.757 ± 0.057	-2.820 ± 0.057
$\Delta R_{04T} / \text{MT Phase II}$	-2.806 ± 0.057	-2.865 ± 0.057

Table 27: *Relative displacements along R between the MAB and the ME1/2 chamber, in two quarters at the +Z CMS side during the CRAFT run and the same relative distances measured during both MT phases.*

The most significant observation from Fig. 44 is that the CRAFT data (dots and circles) show displacement values that are systematically lower (dots, 255°) or larger (circles, 315°) than any MT value.

The fitted parameters are displayed in Table 30. The table does not add any relevant extra information.

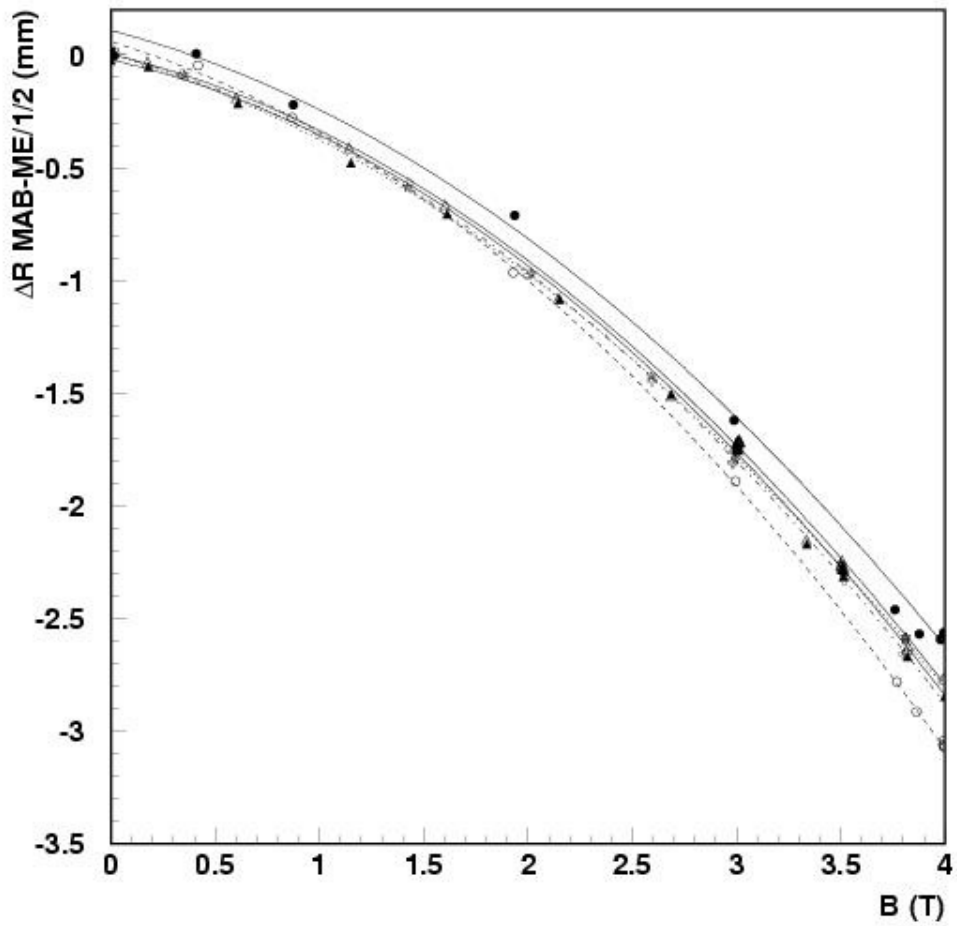


Fig. 44: ΔR (MAB to ME/1/2) as a function of the magnetic field intensity. Dots: CRAFT at $+255^\circ$. Circles: CRAFT at $+315^\circ$. Stars: MT Phase I at $+255^\circ$. Swiss crosses: MT Phase I at $+315^\circ$. White triangles: MT Phase II at $+255^\circ$. Black triangles: MT Phase II at $+315^\circ$.

	a (mm/T ²)	b (mm/T)	c (mm)	X ² /NDF	Residuals widths (mm)
CRAFT +255°	-0.110 ± 0.005	-0.241 ± 0.022	0.108 ± 0.018	129/98	0.064
MT Ph. I +255°	-0.107 ± 0.001	-0.273 ± 0.006	0.004 ± 0.053	44/1048	0.012
MT Ph.II +255°	-0.121 ± 0.001	-0.216 ± 0.002	0.001 ± 0.002	1226/13997	0.017
CRAFT +315°	-0.127 ± 0.005	-0.275 ± 0.022	0.058 ± 0.018	10/98	0.018
MT Ph. I +315°	-0.118 ± 0.001	-0.247 ± 0.006	0.003 ± 0.053	20/1048	0.008
MT Ph.II +315°	-0.124 ± 0.001	-0.209± 0.002	-0.022 ± 0.002	1007/13997	0.015

Table 30: Fitted parameters of the relative displacements between the MAB and the ME/12 chamber to the function $\Delta Z = a \times B^2 + b \times B + c$ on and under ground (see text).

Before leaving this subsection we are going to present and compare the ΔR relative motions between the MABs and their nearest ME/1/2 muon chamber in the five working quarters at the +Z CMS side, during the under ground run.

Fig. 45 shows the relative motions measured in the five quarters at the CMS +Z side as a function of the data number (time). First row displays, in two identical figures, the value of the magnetic field strength at every data taken. All other plots correspond to the relative displacements, in mm, between the MAB and the nearest ME/1/2 chamber in the indicated quarter. As said, the 75° quarter was not giving signal.

The only observation from Fig. 45 is the smaller relative motion in the $+255^\circ$ quarter when compared with the other four working sectors.

Let us now observe (see Table 31) the question of repositioning $\Delta R(0)$ and maximum measured relative displacement ΔR_{04T} between each MAB and its corresponding ME/1/2 chamber in the five working quarters.

Zside and Φ quarter	$\Delta R(0)$ (mm)	ΔR_{04T} (mm)
+Z 15°	0.080 ± 0.057	-3.373 ± 0.057
+Z 135°	0.105 ± 0.057	-3.117 ± 0.057
+Z 195°	0.107 ± 0.057	-2.971 ± 0.057
+Z 255°	0.127 ± 0.057	-2.563 ± 0.057
+Z 315°	0.025 ± 0.057	-3.043 ± 0.057

Table 31: *Repositioning and maximum displacements measured from the observation of MAB and ME/1/2 chamber CMS elements at under ground.*

The first observation from the table is that the two elements retrieve the initial positions, within three standard deviations in the five quarters. In addition the approaching between the observed elements vary from 2.5 mm measured at $\Phi = 255^\circ$ and 3.4 mm measured at $\Phi = 15^\circ$, almost 1 mm difference.

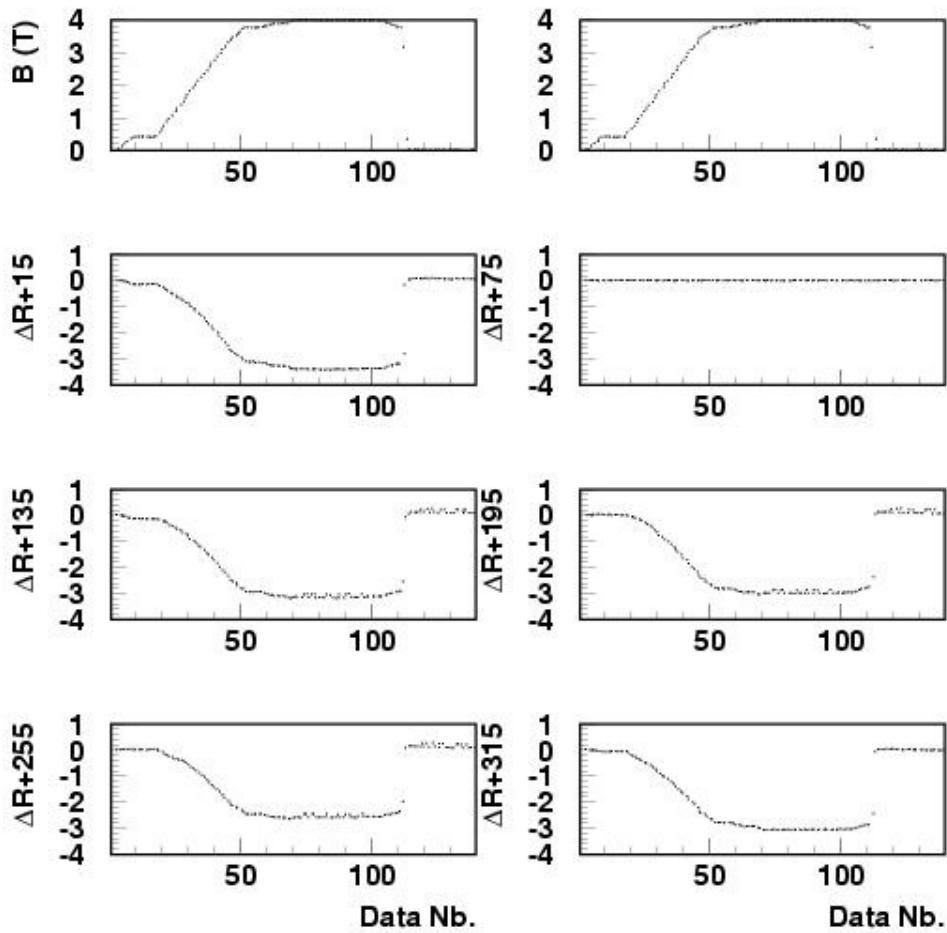


Fig. 45: ΔR (mm) relative distance measured between the MAB and its nearest ME/1/2 chamber, in each of the six quarters at CMS +Z side, as a function of the Data Number. On top two identical plots show the variation of the magnetic field intensity as a function of the Data Number. From CRAFT data.

The behaviour of ΔR between the MAB and its corresponding to ME/1/2 muon chamber, as a function of the magnetic field strength B , is shown in Fig. 46 for the five CMS +Z side working quarters.

In the figure, the 15° quarter data is represented by dots. Black triangles for 135° ; circles represent the 195° quarter data; stars are for 255° and finally, Swiss crosses represent the $\Phi = 315^\circ$ quarter. For clarity, only one data point over ten is plotted.

Inspection of Fig. 46 reveals that the bottom quarters (stars and Swiss crosses) show systematically larger displacements than the top quarters. This observation was also seen when analysing of the ΔR (TP – ME/1/1) data.

In all cases the curves over data points are fits to the function:

$$\Delta R = a \times B^2 + b \times B + c$$

The error given to the data points in the fit was 0.057 mm. The fitted parameters are displayed in Table 32, which does not add any further information.

Φ quarter	a (mm/T ²)	b (mm/T)	c (mm)	X ² /NDF	Residuals (mm)
+ 15°	-0.139 ± 0.005	-0.301 ± 0.022	0.012 ± 0.018	8/98	0.016
+ 135°	-0.132 ± 0.005	-0.267 ± 0.022	0.016 ± 0.018	78/98	0.050
+ 195°	-0.137 ± 0.005	-0.241 ± 0.022	0.135 ± 0.018	119/98	0.062
+ 255°	-0.110 ± 0.005	-0.241 ± 0.022	0.108 ± 0.018	129/98	0.064
+ 315°	-0.127 ± 0.005	-0.275 ± 0.022	0.058 ± 0.018	10/98	0.018

Table 32: Fitted parameters of the relative displacements between the MAB and the ME/1/2 chamber to the function $\Delta Z = a \times B^2 + b \times B + c$ in the five +Z side working quarters. From CRAFT data.

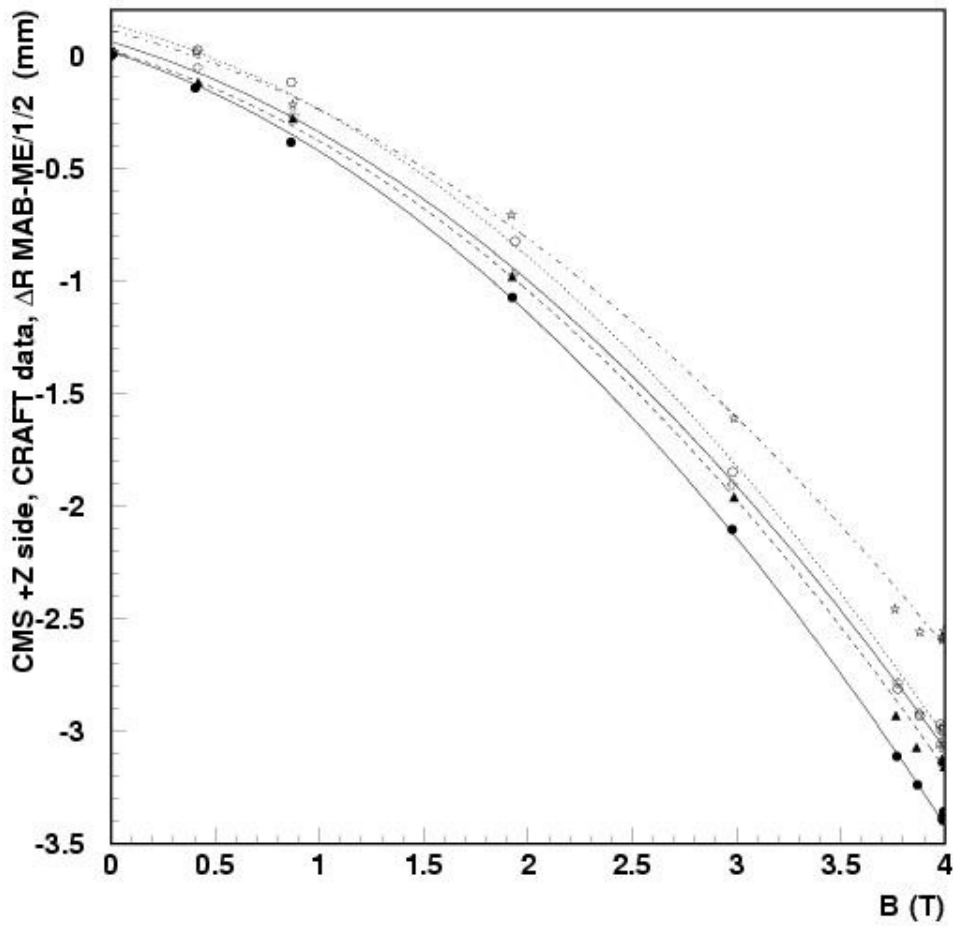


Fig. 46: For the five CMS +Z side working quarters, monitored relative distance between the MAB and the nearest ME/1/2 muon chamber. Dots: 15°; black triangles: 135°; circles: 195°; stars: 255° and Swiss crosses: 315°.

8.5 Monitoring the radial distance between the Link Disk and the Transfer Plate: on and under ground comparisons

The monitoring of the radial distance between the LD and the TP is done via an aluminium tube (RP, radial profile in the vertical direction in Fig. 8), attached to the TP, ~1977 mm long, to which, on its closest end to the LD, is installed a Sakae potentiometer sensor. The rod of the potentiometer contacts a target located on the LD, near the Laser Box (LB) as sketched in Fig. 8. In that manner, the long distance between the LD and the TP will be given by the RP length plus the length of the potentiometer mechanical support (92.444 ± 0.173 mm) plus the short distance measured by the potentiometer [12].

The large error in the measurement of the sensor mechanical support length is due to the fact that the measurement was done, in this case, by photogrammetry instead of using the 3D measuring machine as for the rest of the mechanics associated to the Link Alignment System. Three measuring devices were installed for the MT at Φ angles of 75° , 255° and 315° .

Being R the monitored distance (the one given by the potentiometer plus the length of its mechanical support), let us observe the relative displacement between the two objects, LD and TP on ground (during MT) and under ground (during the CRAFT run). The comparison between the repositioning ($\Delta R(0)$) of the Link Disk with respect to the Transfer Plate, in Phases I and II of the MT and the CRAFT run, are displayed on Table 33 for three Φ CMS +Z side quadrants ($+75^\circ$, $+255^\circ$ and $+315^\circ$) and for the same quadrants at -Z side from the CRAFT data, chosen for illustration.

Also in Table 33, we compare the total displacement (ΔR_{04T}) suffered by the LD with respect to the TP during the ramp from 0 to 4 T in each of the MT Phases and in the CRAFT run. All quantities on Table 31 are given in millimetres.

The comparisons between the computed values for repositioning show elastic behaviour in both MT Phases and in the CRAFT data. Concerning the total displacements, due to the magnetic field forces, in all Φ sectors, the results are compatible with no displacement of the objects under study but in sector 255° .

We were expecting no displacements everywhere because of the TP-RP-LD construction constraint. In view there are, we show in Table 34 the full set of ΔR values recorded during the CRAFT run.

At both Z sides and in all sectors, LD and TP elements retrieve the original positions when the field is switched off. Concerning ΔR_{04T} we observe that TP and LD approach to each other, in two of the Φ quarters, at both Z sides, by more than 3σ over absence of motions.

Although the measured displacements are always below $300 \mu\text{m}$, we show in Fig. 47 the twelve ΔR (LD-TP) set of measurements as a function of the magnetic field intensity, recorded during the under ground CRAFT run, that will allow us to make a further observation.

Z side/Quadrant	75°	255°	315°
+Z/ $\Delta R(0)$ MT Ph. I	-0.005 ± 0.057	0.035 ± 0.057	0.044 ± 0.057
+Z/ $\Delta R(0)$ MT Ph. II	-0.010 ± 0.057	0.139 ± 0.057	-0.009 ± 0.057
+Z/ ΔR_{04T} MT Ph. I	0.004 ± 0.057	-0.338 ± 0.057	-0.001 ± 0.057
+Z/ ΔR_{04T} MT Ph. II	-0.003 ± 0.057	-0.220 ± 0.057	0.052 ± 0.057
+Z/ $\Delta R(0)$ CRAFT	-0.001 ± 0.057	-0.003 ± 0.057	0.002 ± 0.057
+Z/ ΔR_{04T} CRAFT	-0.003 ± 0.057	-0.178 ± 0.057	-0.012 ± 0.057
-Z/ $\Delta R(0)$ CRAFT	0.001 ± 0.057	-0.012 ± 0.057	0.000 ± 0.057
-Z/ ΔR_{04T} CRAFT	0.012 ± 0.057	-0.089 ± 0.057	0.020 ± 0.057

Table 33: Relative displacements along R between the Link Disc and the Transfer Plate measured during both MT phases and the CRAFT run (see text).

Zside and Φ quarter	$\Delta R(0)$ (mm)	ΔR_{04T} (mm)
+Z 15°	-0.001 ± 0.057	0.145 ± 0.057
+Z 75°	-0.001 ± 0.057	-0.003 ± 0.057
+Z 135°	-0.003 ± 0.057	-0.200 ± 0.057
+Z 195°	-0.014 ± 0.057	-0.267 ± 0.057
+Z 255°	-0.003 ± 0.057	-0.178 ± 0.057
+Z 315°	0.002 ± 0.057	0.012 ± 0.057
-Z 15°	0.001 ± 0.057	0.085 ± 0.057
-Z 75°	0.001 ± 0.057	0.012 ± 0.057
-Z 135°	0.001 ± 0.057	-0.181 ± 0.057
-Z 195°	-0.007 ± 0.057	-0.193 ± 0.057
-Z 255°	-0.012 ± 0.057	-0.089 ± 0.057
-Z 315°	0.000 ± 0.057	0.020 ± 0.057

Table 34: Relative displacements along R between the Link Disc and the Transfer Plate measured during the CRAFT run in the 12 Φ quarters (see text).

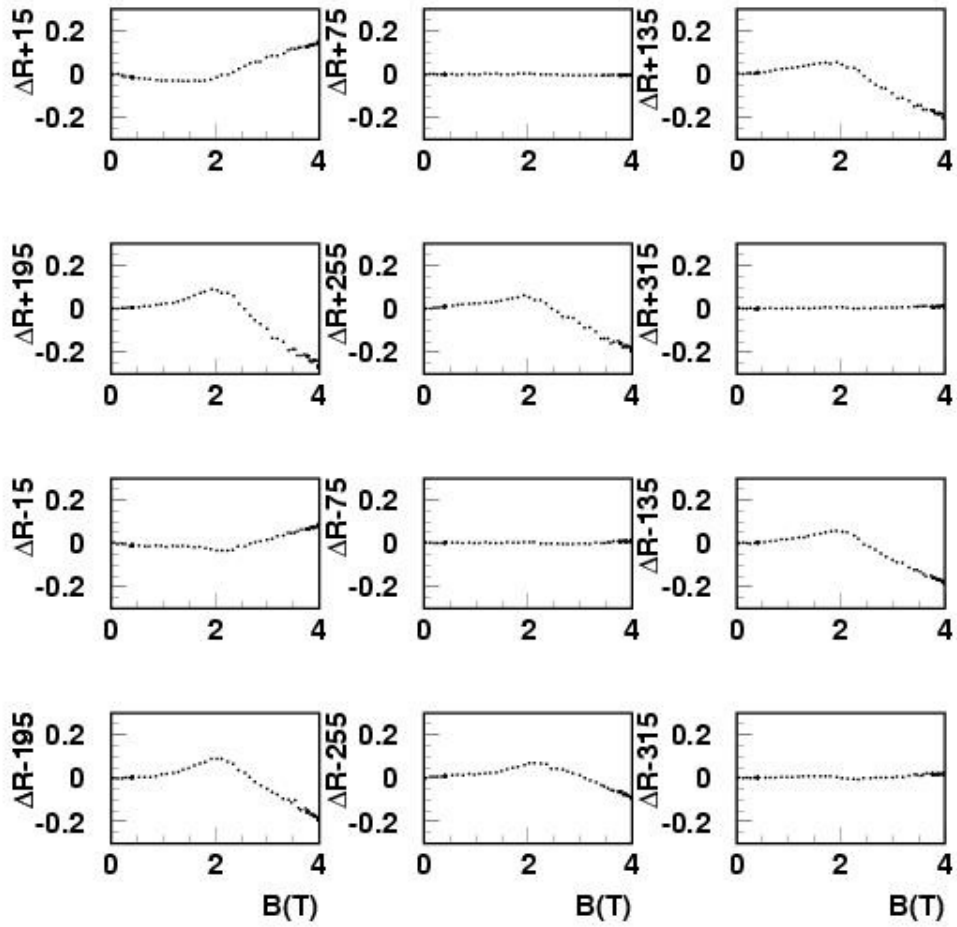


Fig. 47: For the twelve Φ link alignment quarters, monitored relative distance in $R\Phi$ between the LD and its corresponding TP, as a function of the magnetic field intensity.

In most of the observed axial and radial relative displacements between CMS mechanical structures analysed along this document it was almost always present a common effect: the behaviour of the relative motions changes its tendency just after $B = 2\text{T}$ (see Fig. 47 for the particular case of ΔR (LD-TP)). It seems like if the magnetic forces at that level of magnetic field intensity were capable to overcome an existent resistance to the “naturally expected” motion (approaching or getting apart) between structures, most probably due to friction effects between touching elements.

In the particular case of the Transfer plates structures, that are probably the most unstable elements of the detector due to their almost floating position, we will see in the next Section how all these effects originated by the magnetic field and friction forces (among others) induce continuous changes in orientations.

8.6 General remarks from the analysis of the monitoring of displacements on and under ground

Four general observations derive from the analysis of the monitoring of distances between mechanical objects that are common to on and underground tests.

First: equal ramps in magnetic field intensity results in different motions between observed objects. No displacement observed during one run allows predicting the behaviour in the next one. More over: whatever motion mechanically possible may occur. However, discrepancies among measured displacement values between two given mechanical elements will always stay below the $300\ \mu\text{m}$, which seems to us a remarkably good stability from run to run.

Second: it might exist a small asymmetry between motions (in size and in the followed function in the B strength) observed in the half-up and the half-down of the detector when switching on the CMS magnet: displacements are, in general, larger at the half-down.

Third: the displacements due to the magnetic forces do not depend merely on the square of the magnetic field intensity (current in the coils). This is presumably due to the fact that other forces enter also in the play, mainly gravity and frictions between touching elements.

Fourth: the frictions between mechanical elements in contact, that offer resistance to a given motion, are overcome by the magnetic field forces as soon as the magnetic field intensity takes a value above 2T .

9. Angular monitoring with electrolytic clinometers

For the monitoring of the angular motions (small rotations/tilts) of some relevant CMS mechanical structures we use, in the Link Alignment System, electrolytic clinometers (or tiltmeter sensors) manufactured by AGI [15] and calibrated either at AGI or at the laboratory of CIEMAT. Tiltmeters measure the angle, with respect to the gravity vector, of the elements to which they are attached.

The sensor operation is based on the principle that an enclosed bubble of gas, suspended in a liquid, will always orient itself perpendicular to the gravity vector. The bubble is located in a liquid filled glass case (the liquid is a conductive fluid) with three electrodes. When an AC voltage is applied across the two excitation electrodes, the AC output voltage measured at the central pick-up electrode depends on the tilt angle [21].

The precision (measurement error) of these sensors is of the order of 30 – 40 μrad . Fig. 48 reminds the reader the CMS coordinates and angles definitions.

Two types of tiltmeters were used during the Magnet Test, 1D and 2D sensors. 1D sensors measure tilts in one direction, while 2D sensors (two 1D on the same mechanical arrangement, and perpendicular to each other) measures tilts in two perpendicular directions. Figs. 49 a) and b) show both designs.

In the final under ground CMS Link System configuration, a third type of clinometer is used: the 900-H model, also from AGI [21]. This model is called biaxial. In the electrolytic liquid there are four excitation and one pickup electrodes. The position of the gas bubble allows measuring simultaneously the inclinations of the X and Y axis of the sensor. Biaxial sensors are placed on the TPs.

For the Magnet Test and under ground runs, dual tiltmeters were installed at the top and bottom regions of the Alignment Ring. Fig. 50 shows the locations and the monitored angles. The duals appearing attached to the Back Disk in Fig. 50 were not installed for the MT, but they were at under ground. A dual tiltmeter was also installed at the top of the Link Disk (see Fig. 51), in both on and under ground situations.

Monitoring of the Φ and Θ angles in the AR and BD will detect eventual rotation and/or bends of the Tracker Body. In the case of the one installed in the LD, it will give, in principle, notice of eventual rotations and/or bends of the YN/1 iron wheel.

1D sensors were installed in the three MT and the twelve CRAFT MABs. As already said, the MAB structures are 60° apart in Φ , starting at $\Phi = 15^\circ$. Fig. 52 shows a sketch of a MAB with the position of the tiltmeter attached to it. The sensor is placed in an X – Y plane in order to register the eventual rotation of the structure in that plane. Rotations will be small variations (μrads) around the nominal Φ value of the particular MAB structure. Those angular variations are precisely the angle we try to monitor since they would correspond to eventual rotations of the muon barrel iron wheels. Remember that one of the purposes of the Link System is to measure the relative Φ position of the Muon Chambers and the Tracker body.

The readout from a tiltmeter is a voltage signal that translates into angular measurement in a roughly linear way trough a scale factor (S) which value is $\sim 3.5 \mu\text{rad/mV}$ [21].

9.1 Monitoring Φ and Θ angular motions at the Alignment Ring on and under ground

At the AR, top and bottom dual sensors are placed such that the called X-tilt (TX) of each dual sensor lies in a CMS X-Y plane (for Φ monitoring) and the called Y-tilt (TY) is placed in a Y-Z plane (for Θ monitoring).

For the positive Z side, the one equipped during the MT, the meaning of the eventual changes in voltage is the following [21]:

- if $\Delta V(TX) > 0$, then $\Delta\Phi < 0$ (Φ decreases, clockwise rotation around +Z or tilt towards the CMS +X axis),
- if $\Delta V(TX) < 0$, then $\Delta\Phi > 0$ (Φ increases, anticlockwise rotation around +Z or tilt towards the CMS -X axis),
- if $\Delta V(TY) > 0$, then $\Delta\Theta < 0$ (Θ decreases, clockwise rotation around +X or tilt towards the CMS -Z axis) and
- if $\Delta V(TY) < 0$, then $\Delta\Theta > 0$ (Θ increases, anticlockwise rotation around +X or tilt towards the CMS +Z axis).

In the under ground both Z sides are equipped and the meaning of the voltages changes at the -Z side is just the opposite to the one given above.

In the analysis of the AR angular motions we will use the following labeling: TXTAR for the X-tilt of the top dual sensor, TYTAR for the Y-tilt of the top dual sensor, TXBAR for the X-tilt of the bottom dual sensor and TYBAR for the Y-tilt of the bottom dual sensor. Locations of the dual sensors on the Alignment Ring were shown in Fig. 50.

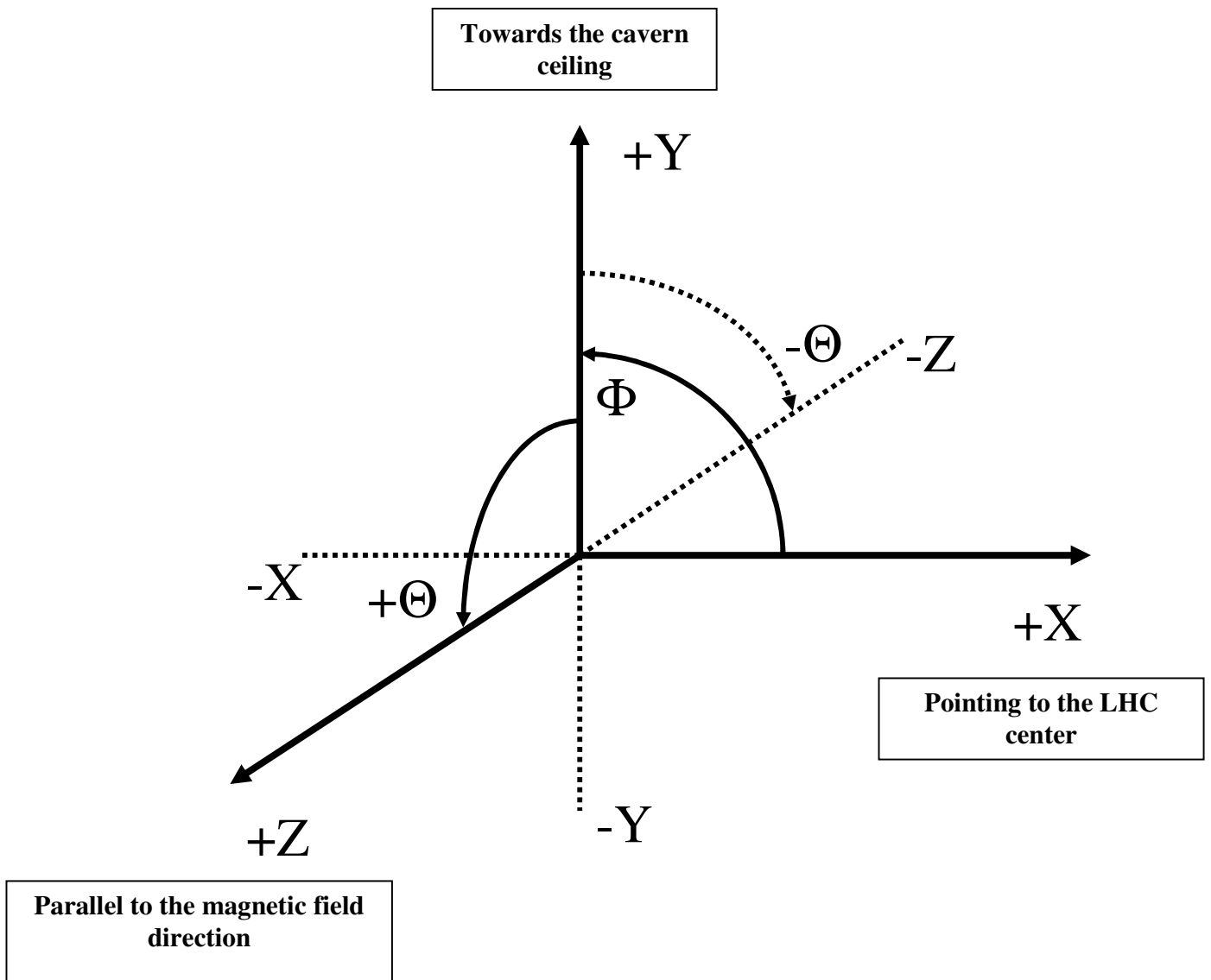
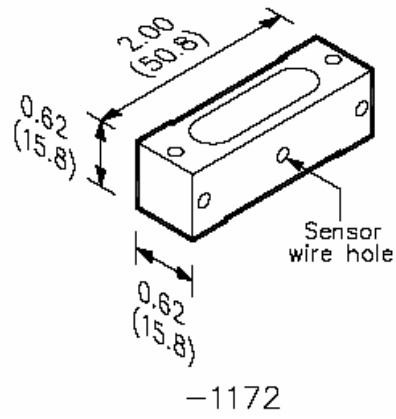


Fig. 48: The CMS coordinate axis system and the definition of angles.

a)



b)

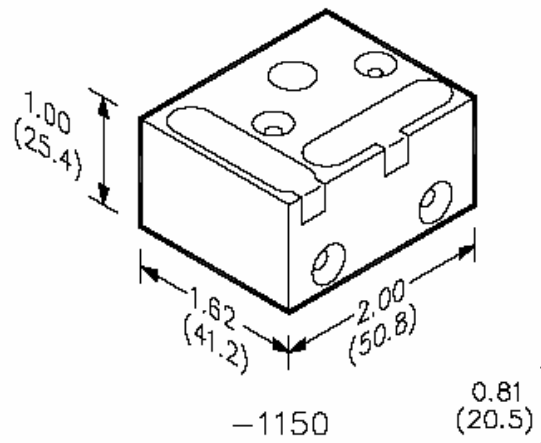


Fig. 49: Sketch and dimensions of the 1D (a) and the 2D (b) tiltmeters used in the monitoring of tilts.

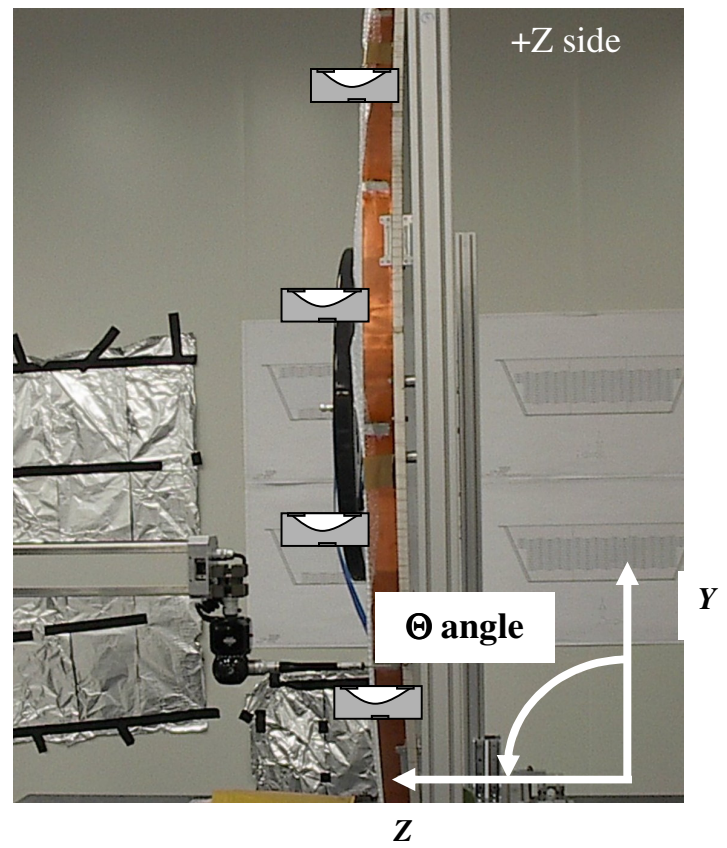
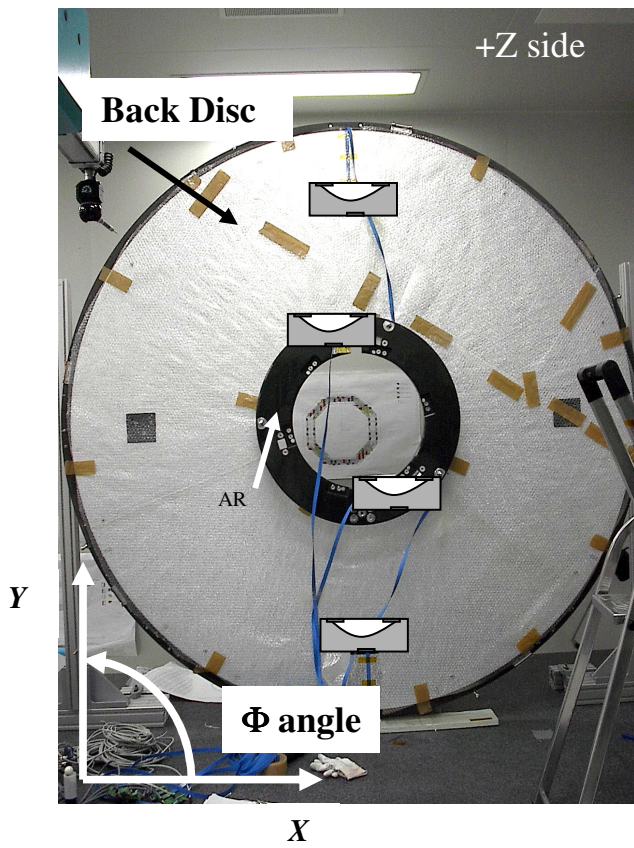


Fig. 50: Photographs of the AR (in black) and BD (in white) with the positions of the tiltmeters during the MT, for the monitoring of tilts in Φ and Θ .

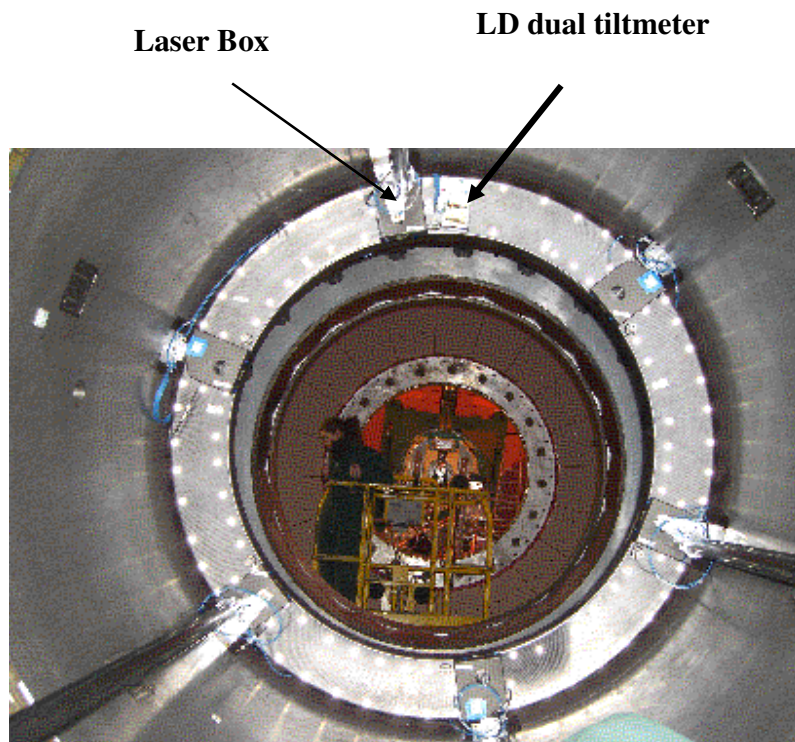


Fig. 51: Photograph of the +Z Link Disc showing the position of the dual tiltmeter and the Laser Box.

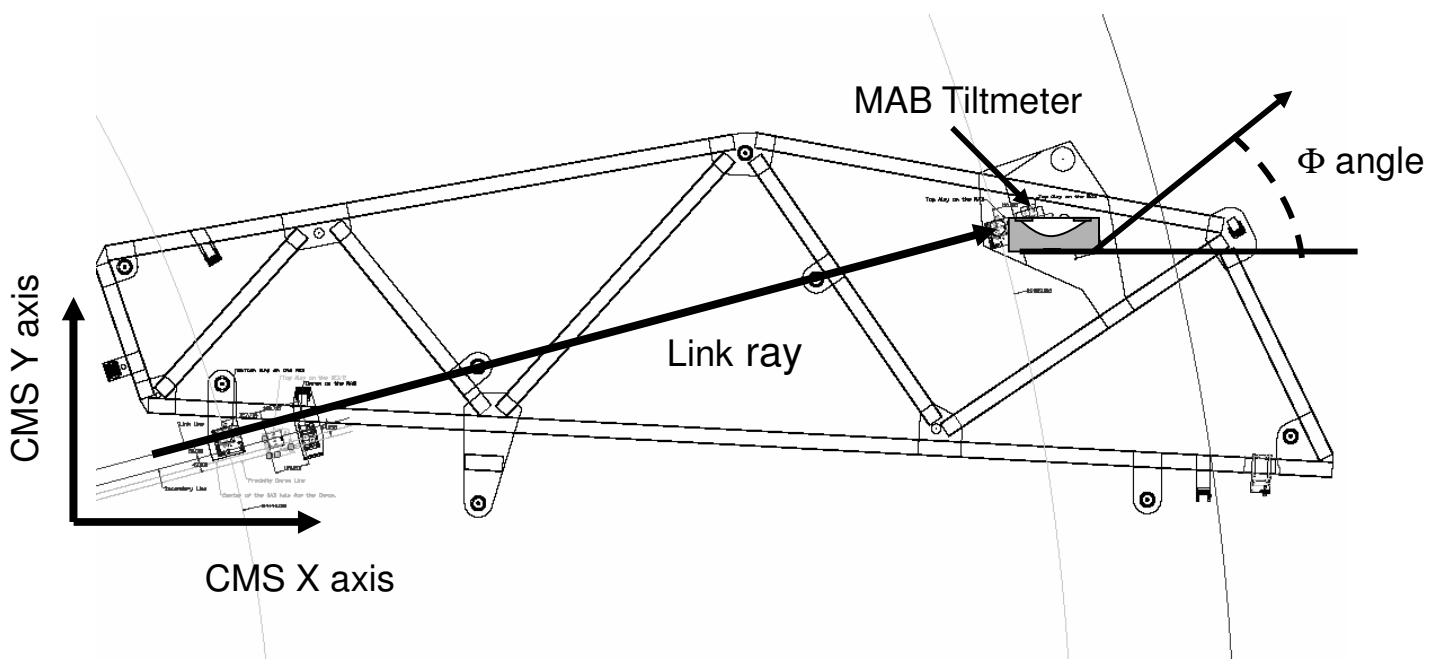


Fig. 52: Sketch of a MAB structure showing the position of the 1D tiltmeter for Φ monitoring.

Let us start by comparing the repositioning of the AR, in Φ and Θ , after eventual tilts originated by the magnetic field forces during the cycle from $B = 0T$ to $B= 4T$ and back to $B = 0T$, as observed from the MT Phase I, on ground, and the CRAFT under ground recorded data.

Let V_i and V_f the initial and final measured voltages, respectively, both at $B = 0T$. The repositioning (difference between the initial and final orientation) is given by: $\Delta\alpha = (V_f - V_i) \times S$, where S is the scale factor of the analyzed sensor and α corresponds to the angle in question, Φ or Θ . The results ($\Delta\alpha$ (μrad) [f-i]) are given in Table 35. The ring ends the cycle with the same orientations (within 1σ) in Φ and Θ as it started.

The measured change in orientations of the AR, when the magnetic field intensity ramps from 0 T to 4 T, $\Delta\alpha_{04T}$ (μrad), are also displayed in Table 35.

Note that, because of the high magnetic field in the area, the values of TYTAR and TYBAR have physical sense only before switching on and after switched off the magnet, so at $B = 0T$ [22].

Observation of Table 35 reveals that the AR retrieves, within 2σ , its initial position ($\Delta\alpha$ [f-i]) after the cycle $0T - 4T - 0T$ in both angles and in both situations, on and under ground.

Concerning the maximum observed rotation in Φ , on and underground measured values are in agreement and compatible with zero at 2σ . The angle Θ follows in both cases the expected exponential change as a function of the magnetic field intensity.

Run Tilted angle	TXTAR (Φ)	TXBAR (Φ)	TYTAR (Θ)	TYBAR (Θ)
MT $\Delta\alpha$ [f-i] (μrad)	-12.5 ± 42.4	33.0 ± 56.6	17.1 ± 42.4	5.6 ± 56.6
CRAFT $\Delta\alpha$ [f-i] (μrad)	91.5 ± 56.6	12.9 ± 56.6	46.9 ± 56.6	21.30 ± 56.6
MT/ $\Delta\alpha_{04T}$ (μrad)	-0.3 ± 42.4	60.0 ± 56.6	369.2 ± 42.4	364.2 ± 56.6
CRAFT $\Delta\alpha_{04T}$ (μrad)	91.5 ± 56.6	49.4 ± 56.6	446.0 ± 56.6	396.0 ± 56.6

Table 35: Monitoring of tilts in Φ and Θ of the AR on (MT) and under (CRAFT) ground, at +Z CMS side.

9.1.1 Monitoring Φ and Θ angular motions at the Alignment Rings and Back Disks in the under ground

The measured recovery of initial orientations $\Delta\alpha$ [f-i], at both Z CMS sides, during the cycle 0T – 4T – 0T are displayed in Table 36. Remember that the BDs close the Tracker Body on both Z sides and that the ARs are “screwed” to the corresponding BDs and therefore we expect to observe, if any, similar tilts in the pair of elements.

Tiltmeter Angular variation	+ Z	- Z
AR Top $\Delta\Phi$ [f-i] (μrad)	91.5 ± 56.6	-3.2 ± 56.6
BD Top $\Delta\Phi$ [f-i] (μrad)	5.33 ± 56.6	17.1 ± 56.6
AR Bottom $\Delta\Phi$ [f-i] (μrad)	12.9 ± 56.6	-23.6 ± 56.6
BD Bottom $\Delta\Phi$ [f-i] (μrad)	-73.5 ± 56.6	1.1 ± 56.6
AR Top $\Delta\Theta$ [f-i] (μrad)	46.9 ± 56.6	-33.3 ± 56.6
BD Top $\Delta\Theta$ [f-i] (μrad)	-3.2 ± 56.6	24.6 ± 56.6
AR Bottom $\Delta\Theta$ [f-i] (μrad)	21.3 ± 56.6	-16.0 ± 56.6
BD Bottom $\Delta\Theta$ [f-i] (μrad)	97.8 ± 56.6	-138.6 ± 56.6

Table 36: Recovery measured in the Alignment Rings and the Back Disks under ground at both Z sides.

The sign assigned to the tilts is the real one: we have included the interpretation of the observed increase/decrease of the voltage. The two elements retrieve the initial orientations within 1σ when averaging Top and Bottom values (see Table 37) in a given element. By doing that we are assuming that neither the Tracker body nor their “backs” nor the ARs can be deformed.

Tiltmeter Angular variation	+ Z	- Z
<AR Top + AR Bottom> < $\Delta\Phi$ [f-i] (μrad)>	52.2 ± 80.0	-13.4 ± 80.0
<BD Top + BD Bottom> < $\Delta\Phi$ [f-i] (μrad)>	-34.1 ± 80.0	9.1 ± 80.0
<AR Top + AR Bottom> < $\Delta\Theta$ [f-i] (μrad)>	34.1 ± 80.0	-24.7 ± 80.0
<BD Top + BD Bottom> < $\Delta\Theta$ [f-i] (μrad)>	47.3 ± 80.0	-57.0 ± 80.0

Table 37: Recovery measured in the Alignment Rings and the Back Disks under ground at both Z sides: averaging Top and Bottom information in a given element.

The maximum observed rotations, differences between the readout values when B reaches 4 T and the readout before switching on the magnet, $\Delta\alpha_{04T}$, are shown in Table 38 for each of the tiltmeters. Remember that the Θ tilts are only the result of the Lorentz forces on the electrolytic solution inside the clinometers.

The X components of the dual tilts that monitor the Φ rotations (receiving the magnetic field lines perpendicular to its major axis) show maximum expected tilts compatible with zero within one standard deviation.

The Y components, that should follow the magnetic field influence, show an opposite sign when comparing +Z and -Z observations. The $\Delta\Theta_{04T}$ value measured in BD Top, 2.1 μrad , seems to be too small. It may well happen that the tiltmeter was not working properly.

The result of averaging Top and Bottom information in a given element is shown in Table 39.

Tiltmeter Angular variation	+ Z	- Z
AR Top $\Delta\Phi_{04T}$ (μrad)	91.5 ± 56.6	0.0 ± 56.6
BD Top $\Delta\Phi_{04T}$ (μrad)	18.1 ± 56.6	26.7 ± 56.6
AR Bottom $\Delta\Phi_{04T}$ (μrad)	49.4 ± 56.6	4.3 ± 56.6
BD Bottom $\Delta\Phi_{04T}$ (μrad)	-54.3 ± 56.6	11.7 ± 56.6
AR Top $\Delta\Theta_{04T}$ (μrad)	446.0 ± 56.6	-477.0 ± 56.6
BD Top $\Delta\Theta_{04T}$ (μrad)	2.1 ± 56.6	-398.5 ± 56.6
AR Bottom $\Delta\Theta_{04T}$ (μrad)	396.0 ± 56.6	-446.2 ± 56.6
BD Bottom $\Delta\Theta_{04T}$ (μrad)	441.0 ± 56.6	-550.2 ± 56.6

Table 38: *Maximum observed tilts in the Alignment Rings and the Back Disks under ground at both Z sides.*

Tiltmeter Angular variation	+ Z	- Z
<AR Top + AR Bottom> < $\Delta\Phi_{04T}$ (μrad)>	70.5 ± 80.0	2.2 ± 80.0
<BD Top + BD Bottom> < $\Delta\Phi_{04T}$ (μrad)>	-18.1 ± 80.0	19.2 ± 80.0
<AR Top + AR Bottom> < $\Delta\Theta_{04T}$ (μrad)>	421.0 ± 80.0	-461.5 ± 80.0
<BD Top + BD Bottom> < $\Delta\Theta_{04T}$ (μrad)>	221.6 ± 80.0	-474.4 ± 80.0

Table 39: Maximum observed tilts in the Alignment Rings and the Back Disks under ground at both Z sides: averaging Top and Bottom information in a given element.

The observation of Table 39 confirms the information: the Tracker body does not show any significant tilt in Φ . Concerning the different sign for the tilt in Θ , when comparing measurements in the both Z sides, the most probable reason for this is that the incoming field lines, at +Z Y-tilts, go from the negative to the positive tilt-poles, while in the -Z Y-tilts they income in the opposite direction.

Measured tilts with respect to the first value (at $B = 0T$) as a function of the magnetic field intensity are shown in Fig. 53. The average of Top and Bottom values in a given element are used in the figure. BD tilts values are represented in black and AR in red dots. For black&white reproductions AR dots happen to be always above BD dots.

The only inconsistency (although minor because points in the figure have an error of $\pm 80 \mu\text{rad}$) is found for the +Z $\Delta\Phi$ where there is an apparent different behavior between the tilts measured for the BD and the AR.

The exponential behavior of $\Delta\Theta$ with B, in both Z sides, is clearly seen in Fig. 53.

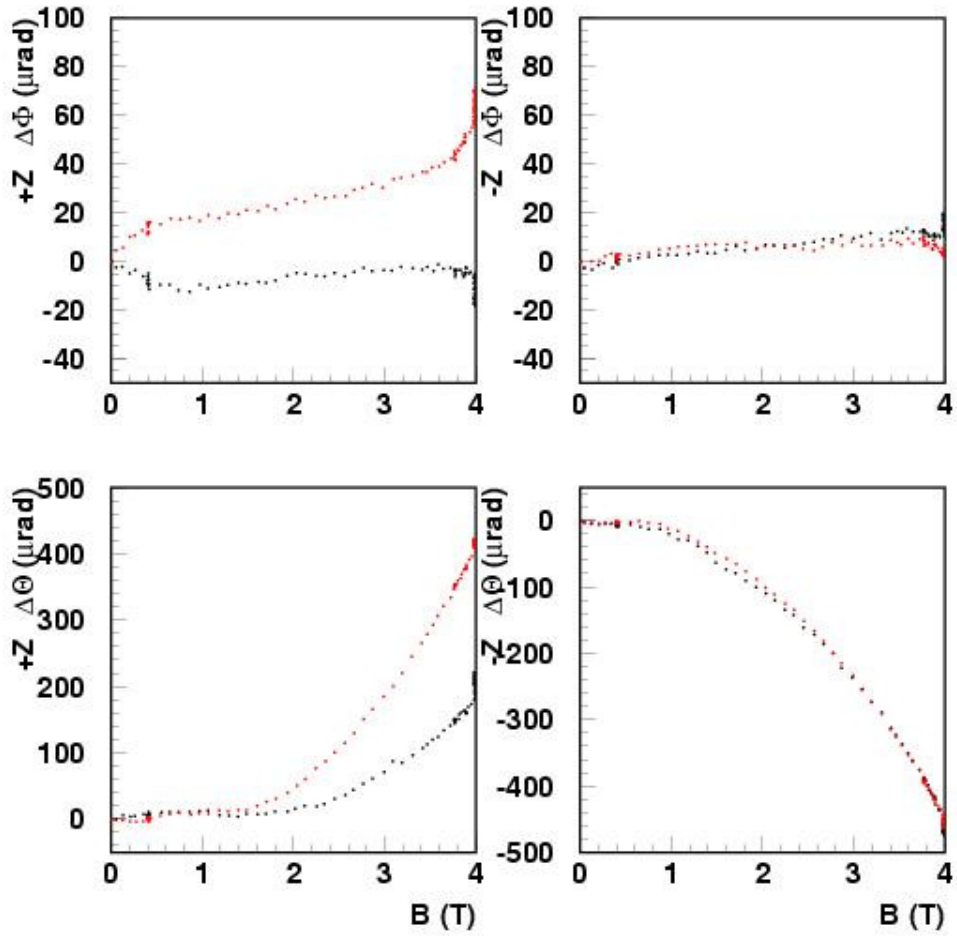


Fig. 53: Observed tilts in the Alignment Rings (in red, lower dots) and the Back Disks (in black, upper set of dots) under ground at both Z sides, as a function of the magnetic field intensity after averaging Top and Bottom information in a given element.

8.2 Monitoring Φ and Θ angular motions at the Link Disk on and under ground

A dual clinometer is located at the top position of the LD, as showed in Fig. 51. The two 1D tilt sensors that compose the unit will be called TXLD (the one monitoring Φ , oriented perpendicular to the magnetic field lines direction) and TYLD (the one measuring eventual tilts in Θ , oriented parallel to the magnetic field direction). The dual sensor was working in both Phases of the Magnet Test and in the CRAFT run.

Proceeding as for the duals in the AR, we will start by comparing the repositioning of the LD, in Φ and Θ , after eventual tilts originated by the magnetic field forces during the cycle from 0T to 4 T and back to 0 T in both MT Phases and in both Z sides at the under ground run. As we did before, data at the first and last $B = 0T$ situations will be called V_i and V_f , respectively. The repositioning (difference between initial and final orientations is given by: $\Delta\alpha = (V_f - V_i) \times S$, where S is the scale factor of the analyzed sensor and α refer to the angle in question, Φ or Θ .

Results from repositioning, $\Delta\alpha$ [f-i], and from the maximum observed angular variations, $\Delta\alpha_{04T}$, are given Table 40.

Z side and Tilt Sensor	$\Delta\alpha$ [f-i] (μrad)	$\Delta\alpha_{04T}$ (μrad)
+Z TXLD Phase I (Φ)	-55.8 ± 42.4	-120.5 ± 42.4
+Z TXLD Phase II (Φ)	-33.0 ± 42.4	-108.4 ± 42.4
+Z TXLD CRAFT (Φ)	16.1 ± 42.4	-87.8 ± 42.4
-Z TXLD CRAFT (Φ)	-3.2 ± 56.6	-90.1 ± 56.6
+Z TYLD Phase I (Θ)	343.9 ± 42.4	1502.7 ± 42.4
+Z TYLD Phase II (Θ)	-46.4 ± 42.4	2259.4 ± 42.4
+Z TYLD CRAFT (Θ)	-9.6 ± 42.4	2283.3 ± 42.4
-Z TYLD CRAFT (Θ)	$+2.1 \pm 56.6$	-1909.2 ± 56.6

Table 40: Monitoring Φ and Θ tilts at the Link Disk on and under ground

The changes observed in the angle Θ are too large to have the Lorentz forces acting on the conductive liquid, as the only reason. We think that real tilts are also playing a role. More studies will be undertaken on this issue in a near future.

However, as earlier mentioned, the measurements done at zero fields are reliable. The $\Delta\Theta$ [f-i] values indicate that the LD finishes the field cycle bent, towards the + Z axis, in $343.9 \pm 42.4 \mu\text{rad}$ in MT Phase I while no appreciable change is observed in MT Phase II, nor in the underground CRAFT run (any Z side). We have no explanation for the above unexpected value.

The change observed in the TXLD tiltmeter output voltage ($\Delta V > 0$, in MT both phases and CRAFT under ground run) implies a $\Delta\Phi < 0$ (see Table 40), which is real: a clockwise rotation around the +Z axis of $120.5 \pm 42.4 \mu\text{rad}$ in MT Phase I, $108.4 \pm 42.4 \mu\text{rad}$ in MT Phase II, $87.8 \pm 42.4 \mu\text{rad}$ in CRAFT +Z side and $90.1 \pm 56.6 \mu\text{rad}$ in CRAFT -Z side, with respect to the nominal 90° starting value.

The Φ and Θ angular variation, with respect to the beginning of the run (at $B = 0T$), are shown in Fig. 54 for both Z sides, as a function of the magnetic field intensity, from the underground CRAFT data.

The Φ variation seems to indicate a rotation of negative sign of both LDs of difficult explanation. Of course, any point in the graphic has an error that makes them compatible with zero within 3σ , but, the tendency is there.

The Θ variation is, as said above, difficult to explain only in terms of the magnetic field influence.

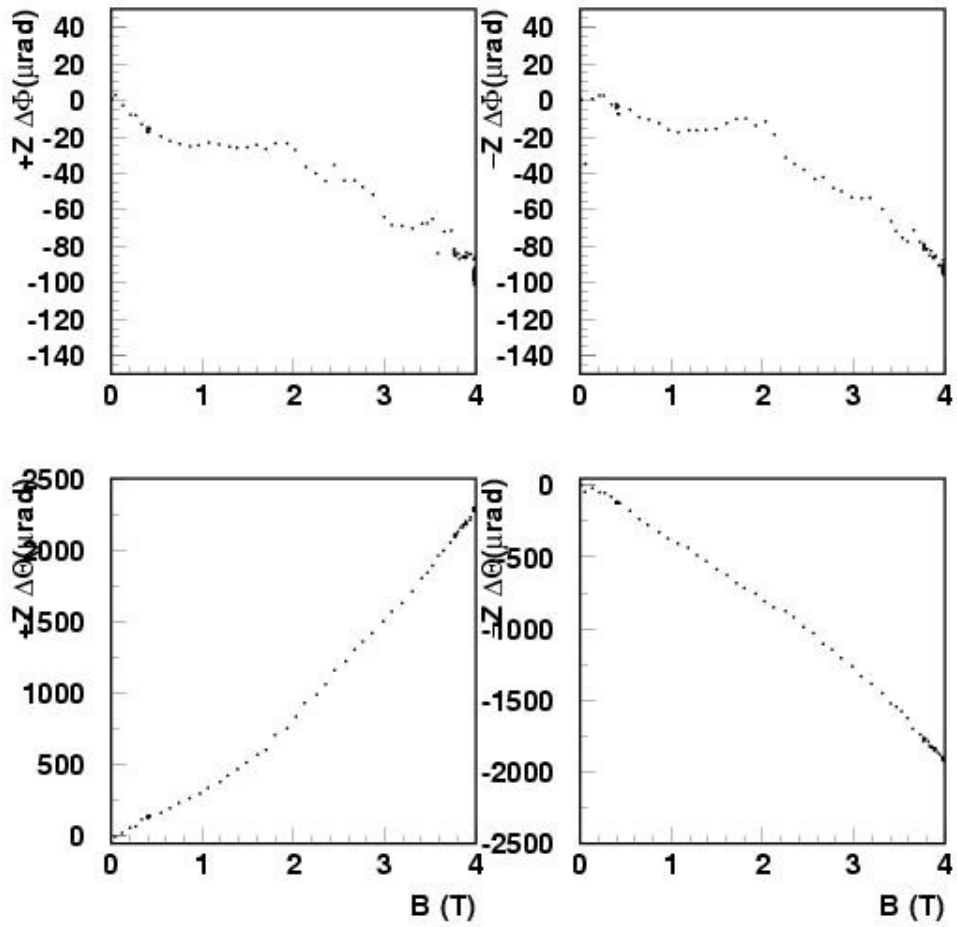


Fig. 54: Monitoring Φ and Θ tilts of the LD at the two Z sides during the underground CRAFT run.

9.3 Monitoring Φ angular motions at the MABs: on and under ground observations

As said, 1D tiltmeter sensors are mounted on the MABs as indicated in Fig. 52. They will monitor eventual rotations of the Barrel iron disk to which they are attached. During both Phases of the MT, tiltmeters are located, before operation, at the nominal Φ values of 75° , 255° and 315° . In the CMS pit, all six MABs at each Z sides are equipped.

At +Z side, and according to the sensors orientations with respect to the returning magnetic field lines, a change in the output voltage $\Delta V > 0$ corresponds to a tilt $\Delta\Phi > 0$, so, an anticlockwise rotation of the iron wheel around the +Z axis. If the observation corresponds to $\Delta V < 0$ is just indication of the opposite rotation. Remember that Φ is positive defined. The uniformity of the field lines when crossing perpendicularly the sensor makes that the readout voltages are reliable.

The observations are summarized in Table 41, where repositioning, $\Delta\Phi$ [f-i], and maximum rotations, $\Delta\Phi_{04T}$, are shown.

MAB and Run	$\Delta\Phi$ [f-i] (μrad)	$\Delta\Phi_{04T}$ (μrad)
MAB-75 MT Phase I	23.0 ± 50.6	-59.2 ± 50.6
MAB-255 MT Phase I	19.1 ± 59.0	-5.2 ± 59.0
MAB-315 MT Phase I	16.3 ± 46.4	-128.7 ± 46.4
MAB-75 MT Phase II	48.8 ± 50.6	-32.0 ± 50.6
MAB-255 MT Phase II	46.5 ± 59.0	-32.0 ± 59.0
MAB-315 MT Phase II	96.2 ± 46.4	-85.8 ± 46.4
MAB-75 MT CRAFT	-11.7 ± 50.6	-82.1 ± 50.6
MAB-255 MT CRAFT	-7.43 ± 59.0	-65.9 ± 59.0
MAB-315 MT CRAFT	16.9 ± 46.4	-93.2 ± 46.4

Table 41: Monitoring tilts in Φ at the MABs: on and under ground comparisons at +Z side.

All observed MABs, on and under ground, retrieve the starting orientation within 2σ and seem to suffer a small clockwise rotations (less than 3σ significance, as for LDs) when the field increases from 0T to 4T.

The $\Delta\Phi$ tilt monitoring of the three equipped MABs along the runs under analysis in both on ground MT Phases, is shown in Figs. 55 a) to d), for Phase I and in e) to h), for Phase II. First row in Fig. 55, display the magnetic field intensity as a function of the data number, already commented. The next three rows of plots show the monitored $\Delta\Phi$ tilts in the three MABs, as a function of the data number in both MT phases.

The extra information, to that of Table 41, which can be extracted from Fig. 55, is that MABs at $\Phi = 75^\circ$ and 255° keep more or less stable and without tilts, within 1σ ($\pm 56.6 \mu\text{rad}$), in both MT Phases, while the MAB at 315° reveal 3σ tilts (or vibrations), that in Phase I increases smoothly along the run (Fig. 55 d)) and in an almost random manner in Phase II, specially during the very long step at $B = 4\text{T}$.

Same information is extracted when looking $\Delta\Phi$ as a function of B , in both MT Phases, shown in Figs. 56 a) to f). The oscillations observed along the long $B = 4\text{T}$ step in Phase II appear in plots d) to f) as a vertical line of dots. We also observe a similarity of behaviors of MABs at 75° and 315° , opposites of that at 255° in both Phases of the MT.

At underground the behavior of $\Delta\Phi$ as function of B , for the three MABs in comparison, is compatible with the observations on ground (see Figs. 57). There is, even, the small difference of measured tilts in the 255° MAB with respect to the other two.

We can not conclude, from Table 41 and Figs. 55, 56 and 57 that the magnetic field implies sizable tilts of the MABs and therefore of the barrel iron disks. However, as pointed out earlier, we have to admit a kind of tendency to very small rotation-like effect, always in the clockwise direction around +Z CMS axis, when the field intensity ramps towards its maximum value.

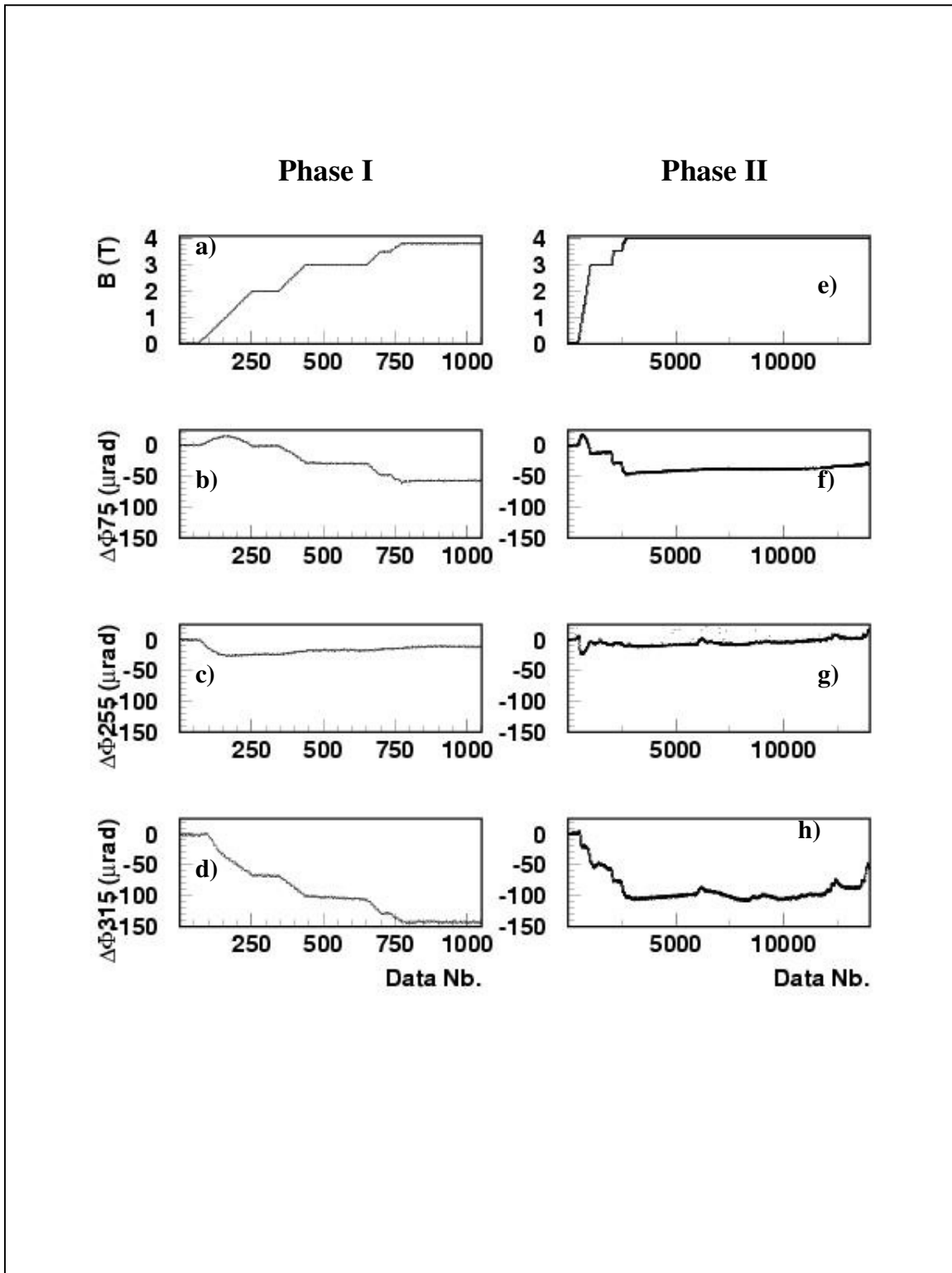


Fig. 55: $\Delta\Phi$ monitoring at three +Z MABs on ground.

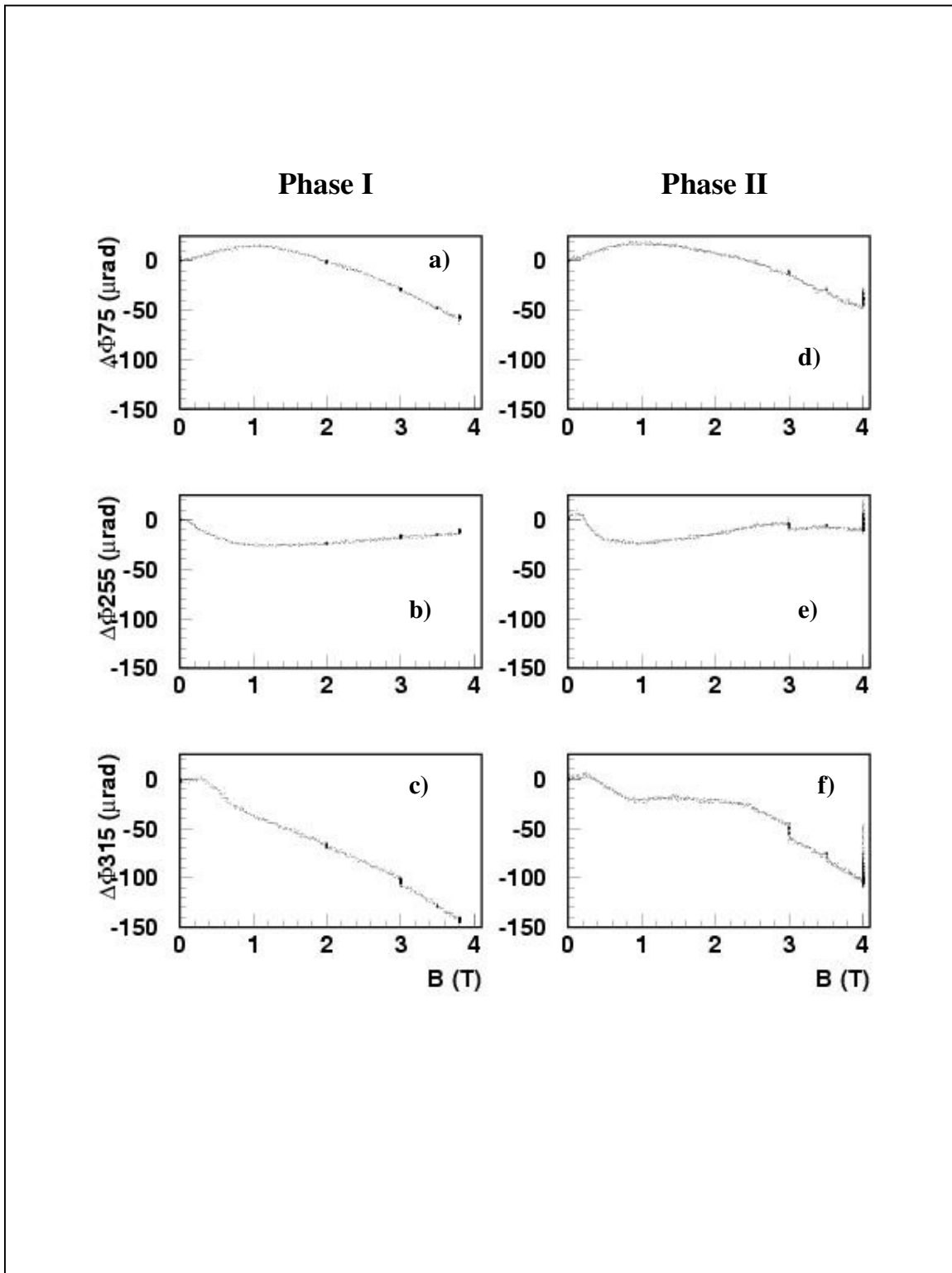


Fig. 56: $\Delta\Phi$ monitoring at three +Z MABs on ground.

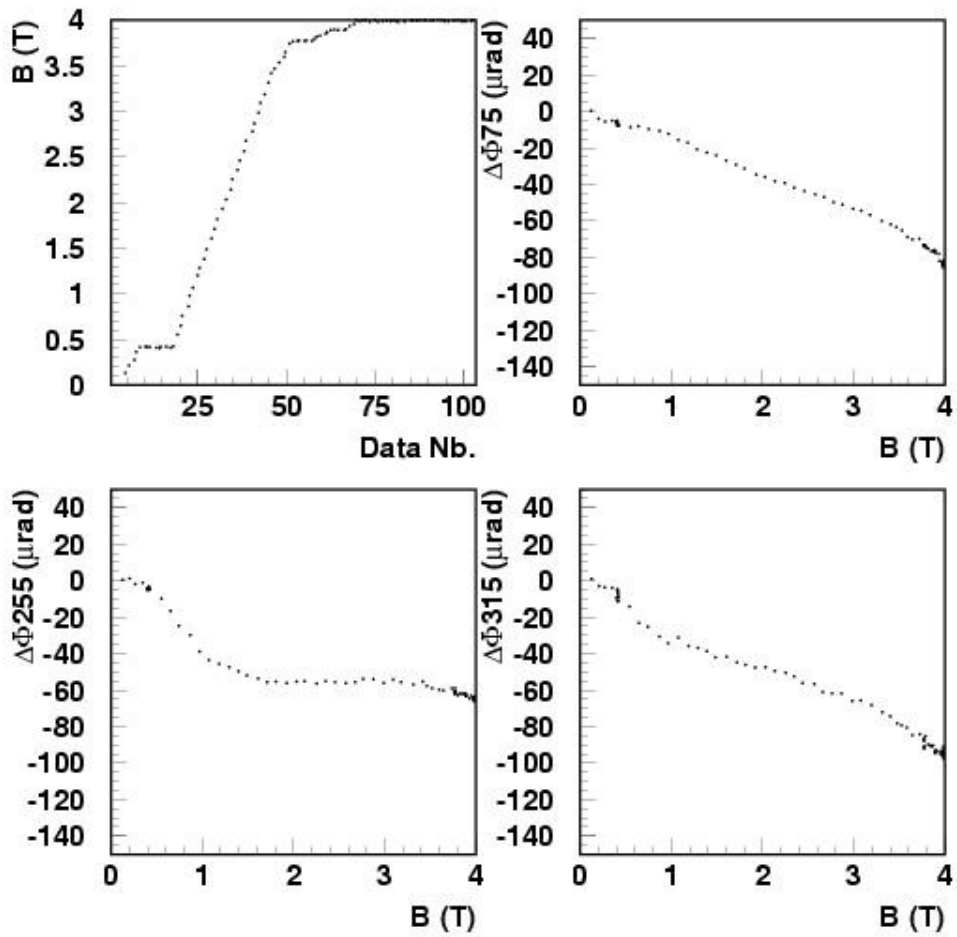


Fig. 57: $\Delta\Phi$ monitoring at three +Z MABs at underground.

9.3.1 Monitoring Φ angular motions at the MABs at the under ground: +Z/-Z comparisons

As said, at the under ground all the Link Alignment elements were in place and therefore the twelve MABs were equipped with 1 D tiltmeters to monitor eventual Φ rotations.

Accordingly with the clinometer disposition on the MABs, for an observed looking from the +Z endcap, an increase in the voltage value at +Z corresponds to a tilt in the sense of $\Phi > 0$. At -Z the correspondence (always looking from the +Z encap) is just de opposite: if the output voltage increases, the tilt is in the sense of $\Phi < 0$.

The observations are summarized in Table 42, where repositioning, $\Delta\Phi$ [f-i], and maximum rotations, $\Delta\Phi_{04T}$, are shown and comparison can be made between measurements at both CMS Z sides. The sign in the $\Delta\Phi$ values corresponds to the direction of the rotation: an observer sitting at the +Z encap will see anticlockwise ($\Delta\Phi > 0$) or clockwise rotations ($\Delta\Phi < 0$).

MAB	+Z $\Delta\Phi$ [f-i] (μrad)	-Z $\Delta\Phi$ [f-i] (μrad)	+Z $\Delta\Phi_{04T}$ (μrad)	-Z $\Delta\Phi_{04T}$ (μrad)
15°	1.1 \pm 52.9	-21.2 \pm 15.3	-32.1 \pm 52.9	-57.3 \pm 15.3
75°	-11.8 \pm 50.6	-25.3 \pm 15.0	-82.1 \pm 50.6	-68.2 \pm 15.0
135°	-10.7 \pm 53.3	-1.1 \pm 24.9	-145.2 \pm 53.3	-1.1 \pm 24.9
195°	14.9 \pm 60.0	-174.8 \pm 17.0	-101.9 \pm 60.0	-197.4 \pm 17.0
255°	-7.4 \pm 59.0	-31.3 \pm 17.0	-65.9 \pm 59.0	-65.8 \pm 17.0
315°	16.9 \pm 46.4	12.8 \pm 35.5	-93.2 \pm 46.4	26.6 \pm 35.5

Table 42: Monitoring tilts in Φ at the MABs in the underground: comparisons between +Z and -Z sides.

Concerning repositioning all MABs recover the initial orientation, within one or two standard deviations, but the one at $\Phi = 195^\circ$ at -Z side that seems to finish the cycle 0T - 4T - 0T with an orientation of $\Phi = 195^\circ - (174.8 \pm 17.0) \mu\text{rad}$. The tilt, being insignificant in comparison with the phtogrammetry uncertainties in the nominal orientation, deviates from zero in more than ten standard deviations.

Observation of the maximum measured tilts ($\Delta\Phi_{04T}$) several MABs at both sides show small indications of clockwise tilts.

For completeness, we show in Fig. 58 and 59 the measured tilts as a function of the magnetic field strength.

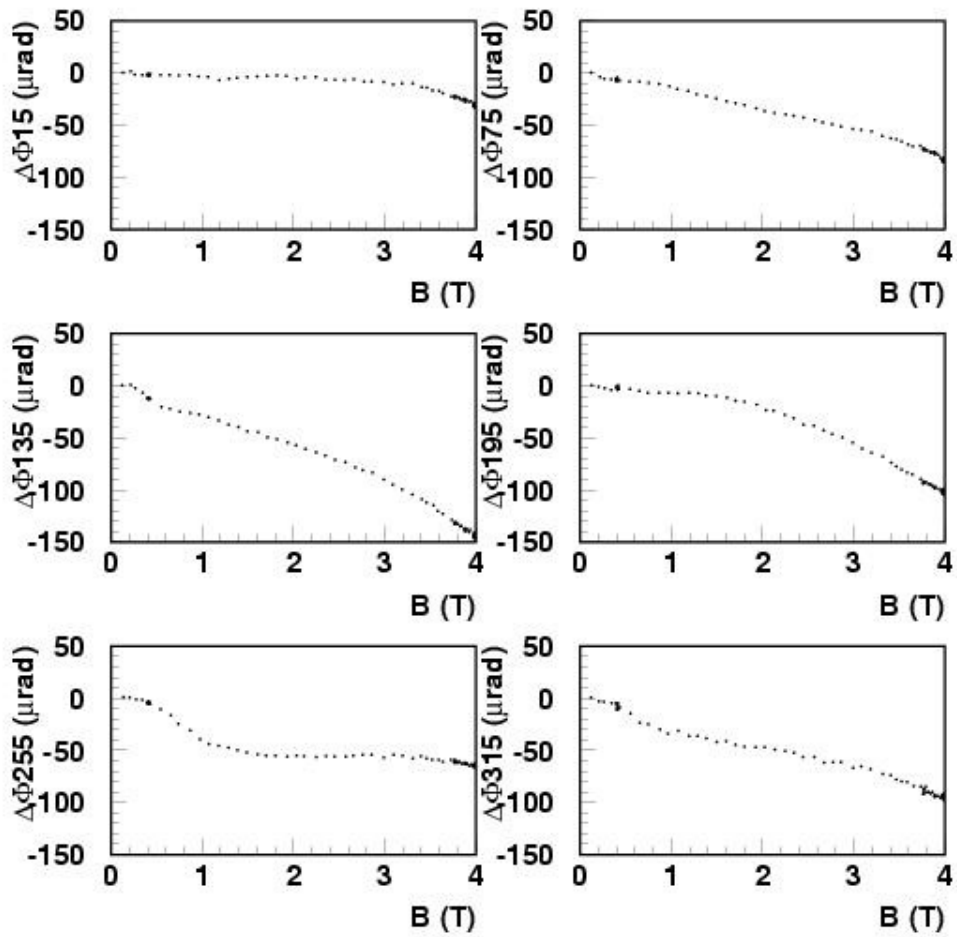


Fig 58: Φ monitoring of the six +Z MABs.

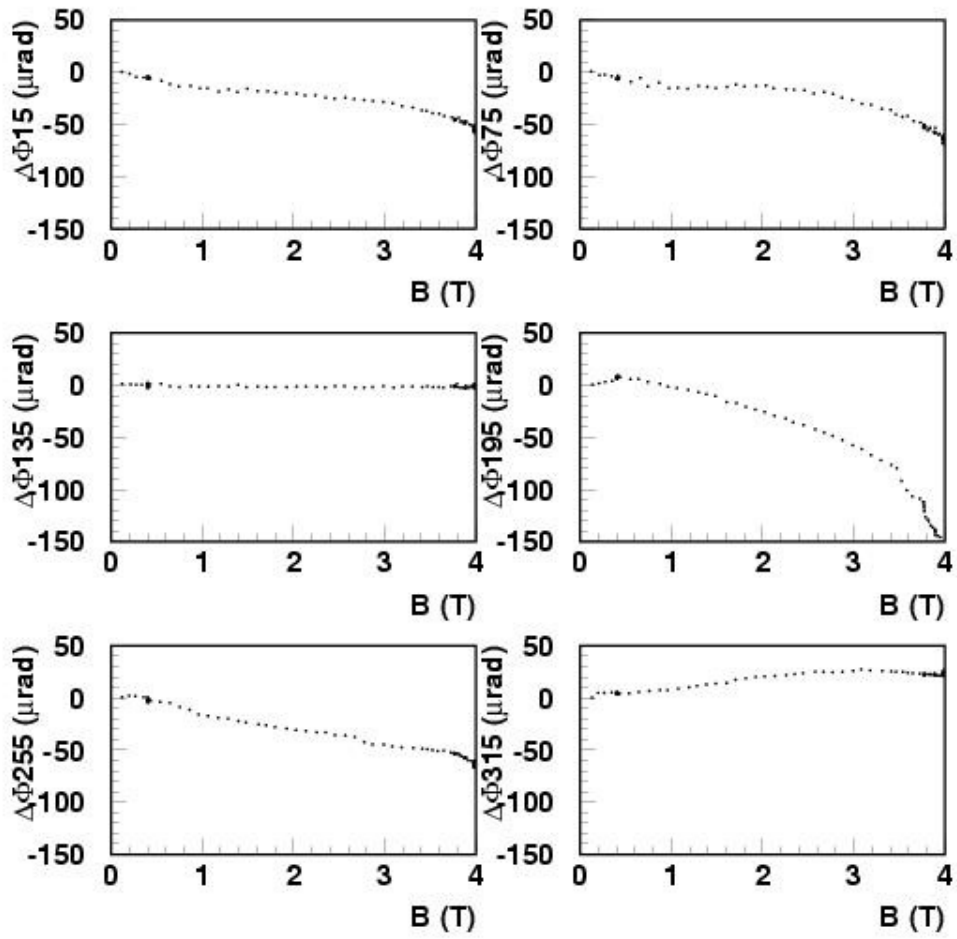


Fig 59: Φ monitoring of the six $-Z$ MABs.

9.4 Monitoring Φ and Θ angular motions at the TPs from the under ground CRAFT run:
+Z/-Z comparisons

Tiltmeters on the Transfer Plates are biaxial 900-H sensors. They measure TP tilts in Φ and Θ , components Y and X, respectively, similar to a dual tiltmeter, but, in the biaxial, all the four excitation electrodes as well as the pick-up one are placed in the same volume and the gas bubble is common for both coordinates. In Fig. 60 we show a sketch of the sensor and a photograph of two biaxial clinometers on top of the calibration mounting.

The interpretation of the readout voltages is the following: at +Z side if $\Delta V(Y) > 0$ then $\Delta\Phi > 0$ indicating that the TP rotates in anticlockwise around the CMS +Z axis. If $\Delta V(X) > 0$ then $\Delta\Theta < 0$ indicating that the TP gets inclined towards the CMS -Z axis, towards the IP.

At -Z side, if $\Delta V(Y) > 0$ then $\Delta\Phi < 0$ indicating that the TP rotates in clockwise around the CMS +Z axis. If $\Delta V(X) > 0$ then $\Delta\Theta > 0$ indicating that the TP gets inclined towards the CMS +Z axis, towards the IP too.

The results concerning repositioning and maximum rotations are shown in Table 43 for Φ tilts and in Table 44 for Θ tilts.

TP	+Z $\Delta\Phi$ [f-i] (μrad)	-Z $\Delta\Phi$ [f-i] (μrad)	+Z $\Delta\Phi_{04T}$ (μrad)	-Z $\Delta\Phi_{04T}$ (μrad)
15°	+1028 \pm 65	-201 \pm 47	+3841 \pm 65	+3021 \pm 47
75°	+378 \pm 65	-1912 \pm 15.0	+1528 \pm 65	-733 \pm 40
135°	+768 \pm 129	-560 \pm 83	-2283 \pm 129	-2409 \pm 83
195°	+318 \pm 65	-500 \pm 71	-2599 \pm 65	-3375 \pm 71
255°	-379 \pm 44	+519 \pm 40	-1819 \pm 44	-752 \pm 40
315°	-477 \pm 55	-648 \pm 45	+1579 \pm 55	+1281 \pm 45

Table 43: Monitoring tilts in Φ at the TPs in the underground: comparisons between +Z and -Z sides.

It was said, when studying displacements, the TP areas were very unstable. A first look into Tables 43 and 44 leads to the conclusion that they suffer continuous rotations in both Φ and Θ angles which can exceed the mrad, without any apparent logic.

The repositioning is inexistent neither in Φ nor in Θ . There are cases in which the difference from the original orientation is larger at the end of the run ($B = 0T$) than at the moment in which the magnetic field intensity arrives to its maximum ($B = 4T$).

TP	+Z $\Delta\Theta$ [f-i] (μrad)	-Z $\Delta\Theta$ [f-i] (μrad)	+Z $\Delta\Theta_{04T}$ (μrad)	-Z $\Delta\Theta_{04T}$ (μrad)
15°	+1574 \pm 88	-1072 \pm 28	+2941 \pm 88	-2246 \pm 28
75°	+1550 \pm 75	-3 \pm 21	+3415 \pm 75	-1714 \pm 21
135°	+1550 \pm 58	-2135 \pm 98	+3419 \pm 58	-3756 \pm 98
195°	+1074 \pm 69	-1477 \pm 83	+1062 \pm 69	-2045 \pm 83
255°	+843 \pm 81	-492 \pm 64	+191 \pm 81	-626 \pm 64
315°	-305 \pm 37	+297 \pm 83	-426 \pm 37	+240 \pm 83

Table 44: Monitoring tilts in Θ at the TPs in the underground: comparisons between +Z and -Z sides.

Let us now look into the tilts variations as a function of the magnetic field strength. Note that the electrodes in the 900-H biaxial sensors are so close to each other (couple of millimetres between poles) that we do not expect any B gradient between them and therefore the electrolytic solution cannot made motions affecting the output voltage.

Figs. 61 and 62 show $\Delta\Phi$ as a function of the B intensity for the 6 Φ quarters at +Z and -Z CMS sides, respectively. Note that the tilts are given in mrad and that the first row of plots, in both columns at both figures, show the B field intensity as a function of the data number.

It seems clear that, in spite of the difficult understanding of Table 41, at both CMS Z sides, in the corresponding Φ quarters, the TP make similar tilts.

The behaviour of $\Delta\Theta$ as a function of B at the 6 Φ quarters at +Z and -Z CMS sides are shown in Figs. 63 and 64, respectively. Also for this angle, the TP rotations show a correspondence: asymmetric in this case.

The overall “elegant” tilts of the Transfer Plates are shown, in “compact” drawings, in Figs. 65 and 66 for $\Delta\Phi$ and $\Delta\Theta$, respectively.

Note that, as mentioned in 9.5, a clear change of tendency is seen in all plots in the summary Figs. 65 and 66 when the magnet field strength crosses the 2T level.

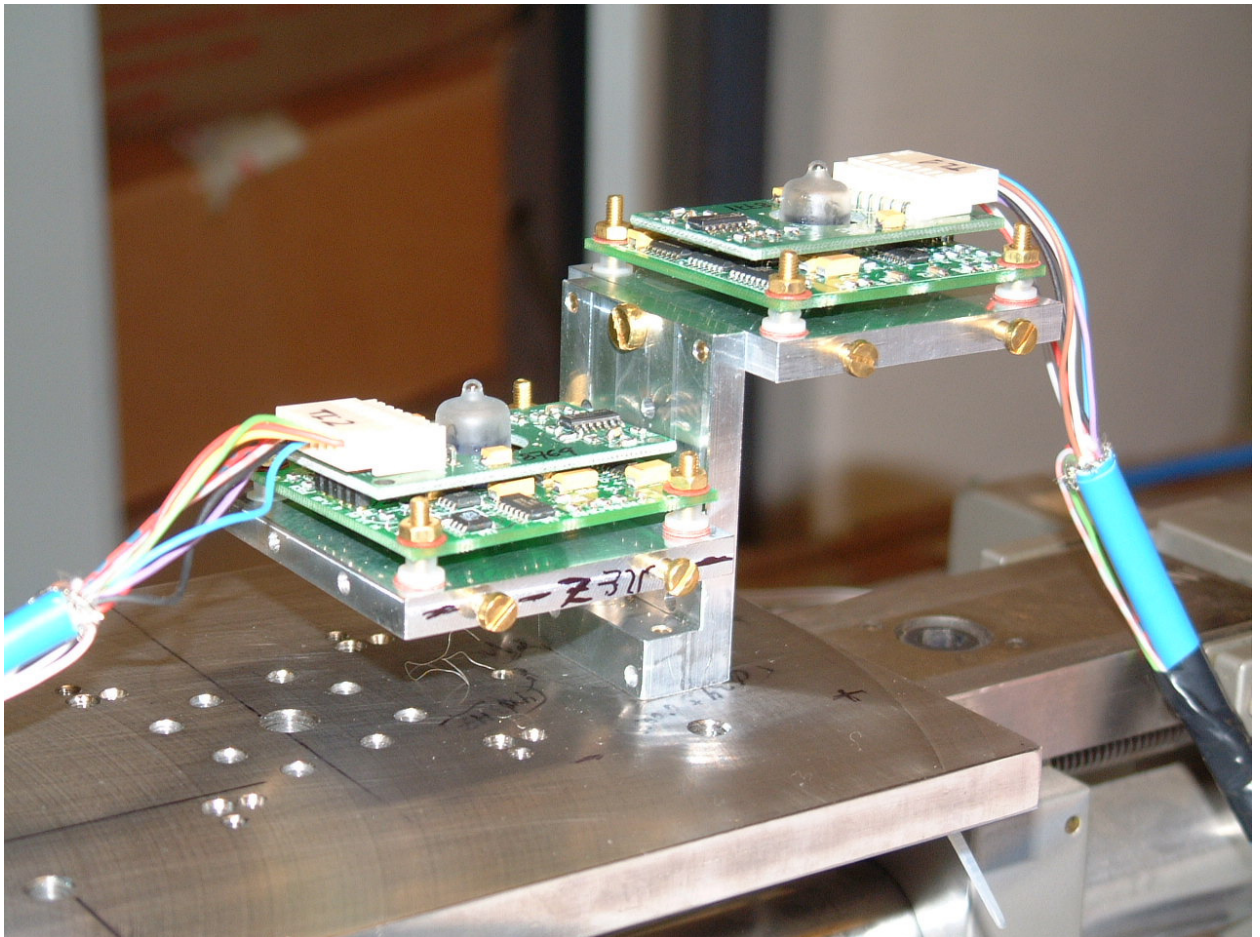
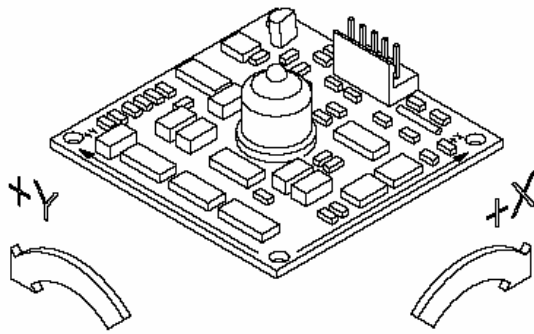


Fig 60: Sketch and photograph of 900-H biaxial clinometers

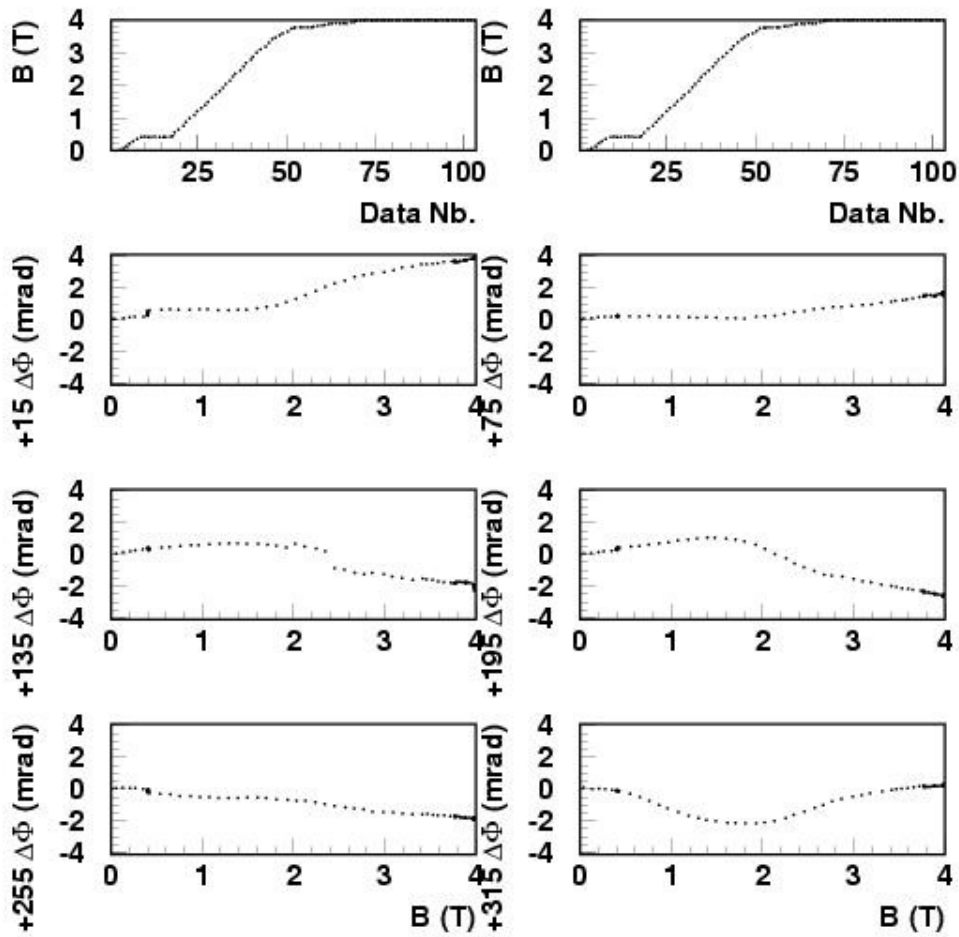


Fig. 61: Monitoring of Φ as a function of the magnet field intensity at +Z side from the recorded underground run data.

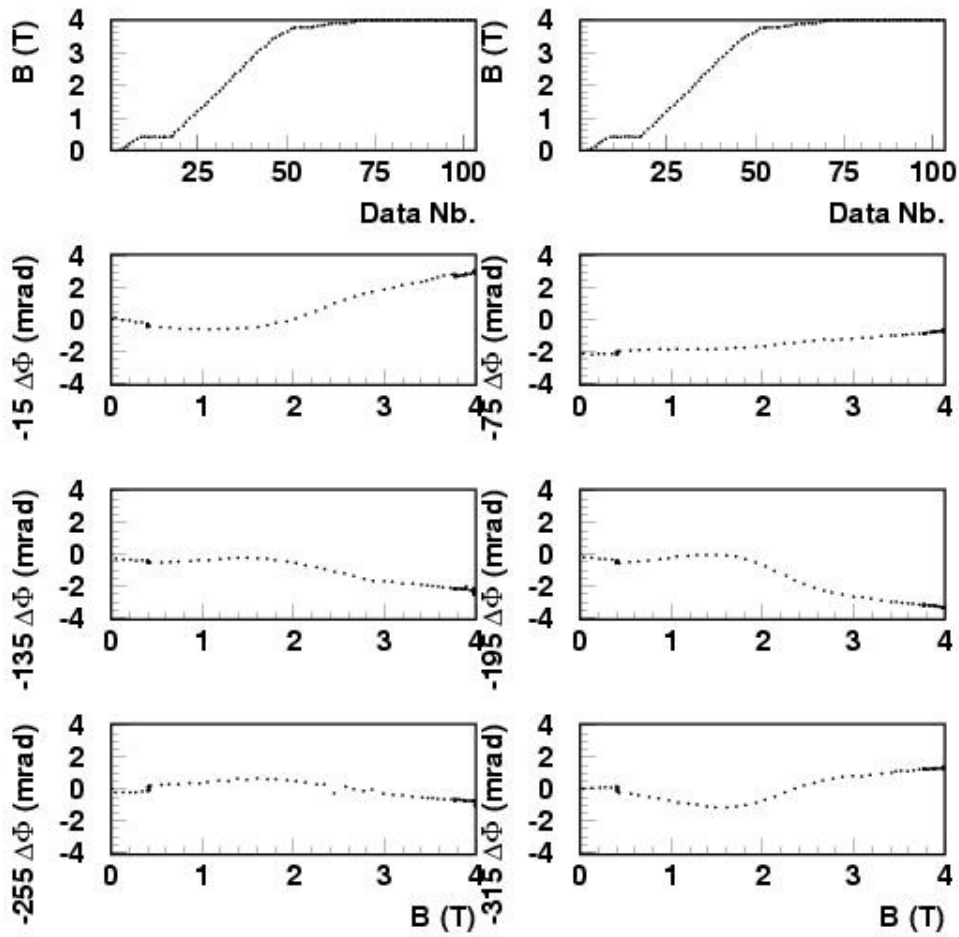


Fig. 62: Monitoring of Φ as a function of the magnet field intensity at -Z side from the recorded underground run data.

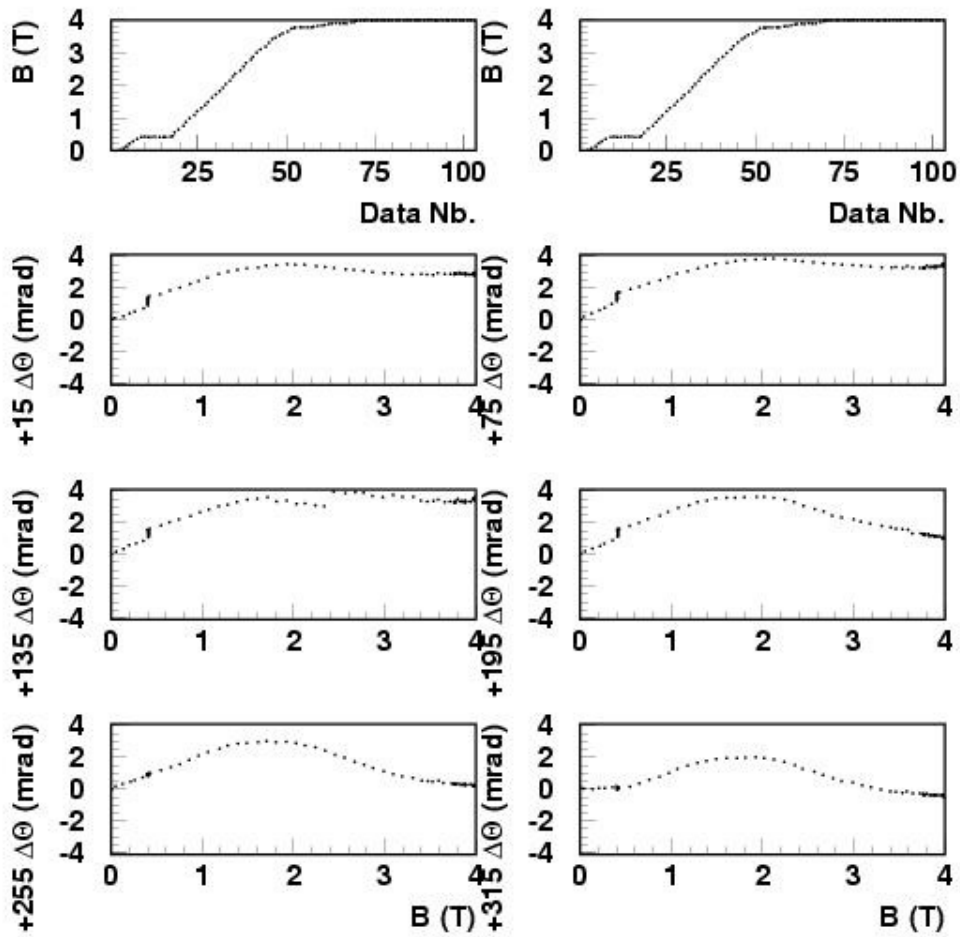


Fig. 63: Monitoring of Θ as a function of the magnet field intensity at +Z side from the recorded underground run data.

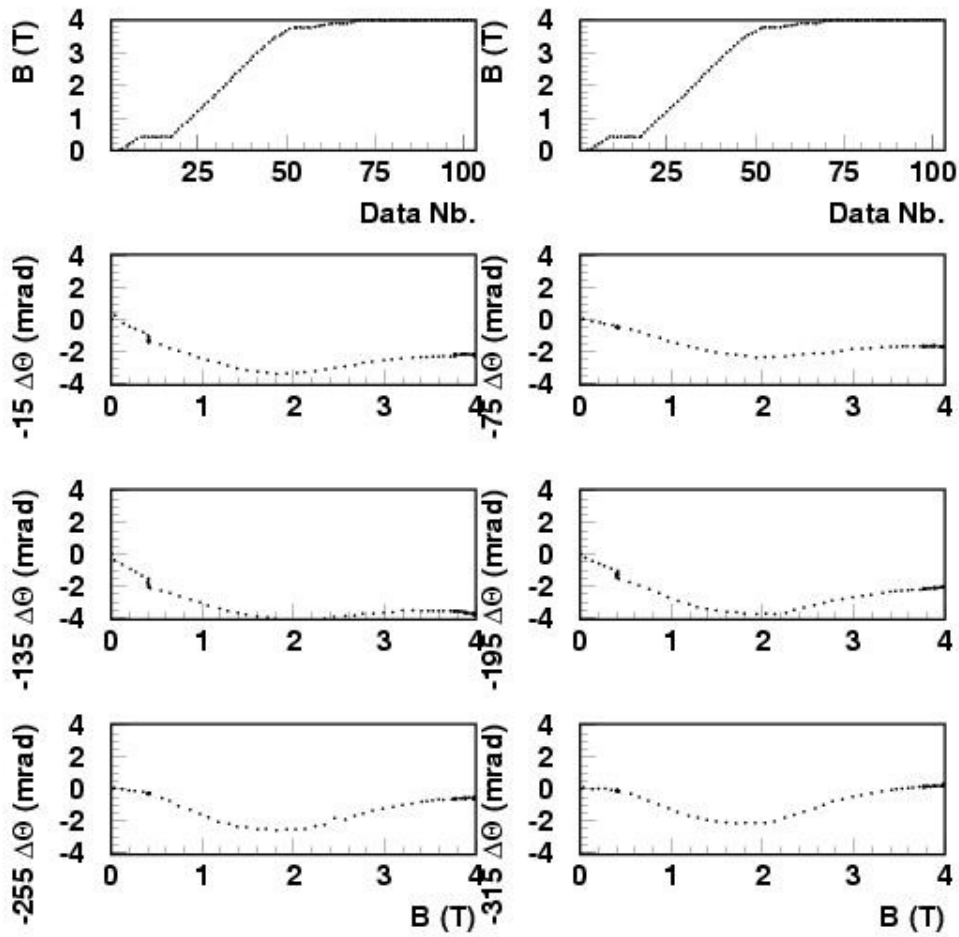


Fig. 64: Monitoring of Θ as a function of the magnet field intensity at -Z side from the recorded underground run data.

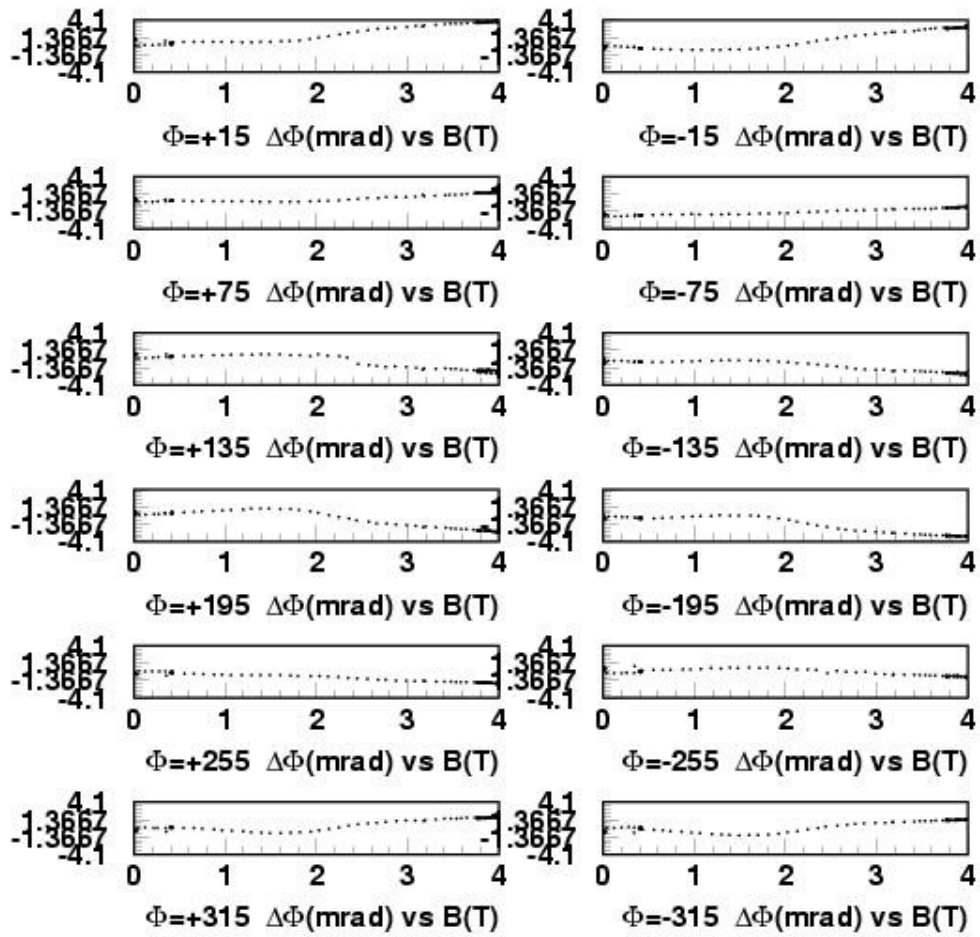


Fig. 65: Monitoring of Φ as a function of the magnet field intensity at both CMS sides from the recorded under ground run data.

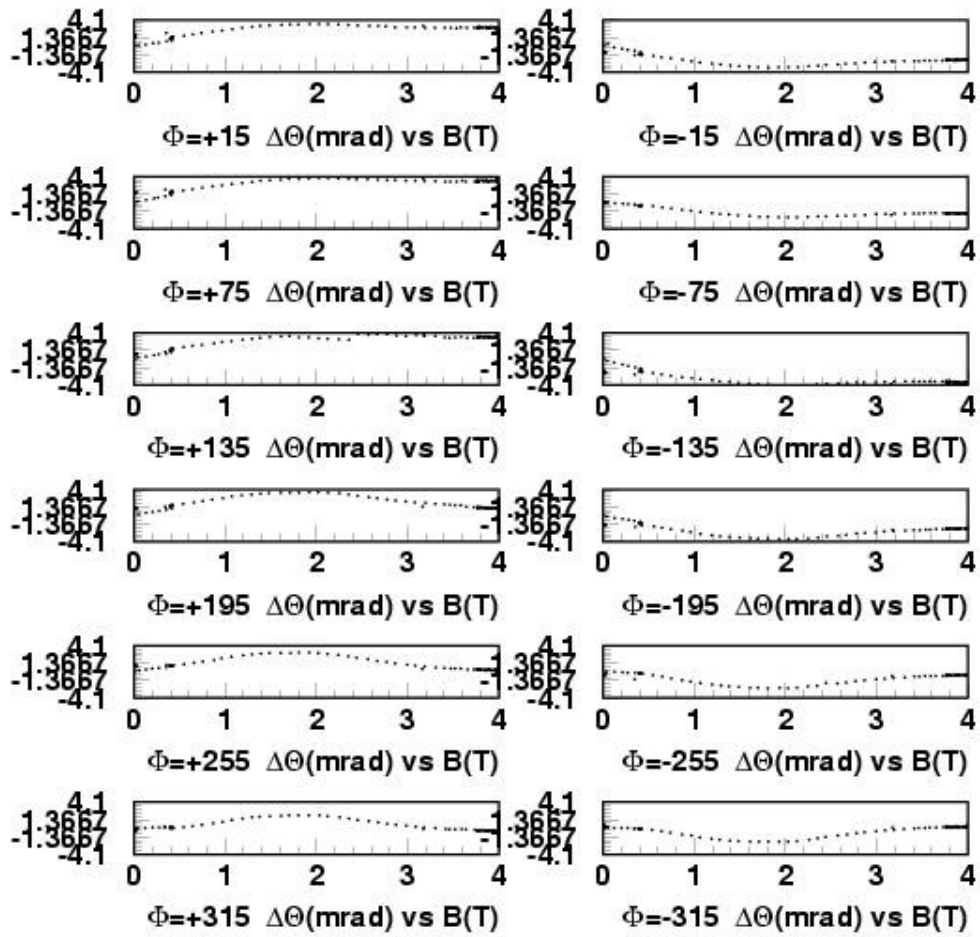


Fig. 66: Monitoring of Θ as a function of the magnet field intensity at both CMS sides from the recorded under ground run data.

10. Summary and Conclusions

A test of part of the CMS Muon Alignment System was performed in summer and autumn 2006 as part of the first commissioning of the four-Tesla Magnet. The test (Magnet Test and Cosmic Challenge, MTCC) took place in the SX5 CMS assembly Hall at CERN. About 5% of the Muon detector was also commissioned with cosmic rays.

A quarter of the Link Alignment System was installed and operated during the test. The readout electronics, DAQ and detector control systems, integrated into the DCS (Detector Control System) environment, were also successfully tested.

Two years later, the full CMS Muon Alignment System was taking data at the underground UX5 point, during the CMS Cosmics Run at Four Tesla (CRAFT08). Further runs were done at 3.8T (CRAFT09) during the year 2009.

Calibrations of individual sensors and laser holder structures, 3D measurements of sensor mounts and associated mechanics, and survey and photogrammetry measurements of the installed components were done prior to and during the installation.

The Link Alignment System was performing well and achieved the expectations concerning the high precision monitoring of displacements and rotations.

Main observations were:

A permanent change in the original positions of the structures (the positions before any magnet operation) was seen. The compression of the structures along Z, towards the interaction point, and the deformations in $R\Phi$ seem to stabilize after a full cycle of the magnet takes place for first time. These initial displacements and deformations are permanent: they are not recovered in subsequent magnet-off states, and can be interpreted as the final closing of the structures due to the magnetic forces acting on the iron pieces. The magnitudes of the measured displacements are specific to each CMS closing experience and cannot be extrapolated to other scenarios.

In general, during the rump up to 3.8 T, the LD approach its corresponding AR due to the motion of the YN1 yoke (to which the LD is attached) towards the Tracker Body Back Disk (to which the AR is attached) by 13 – 14 mm in the Z direction, due to the ~5.6 kt magnetic field force pushing the central end cap yokes towards the CMS geometrical centre at both Z sides. The ME1/1 muon chamber gets apart by 1.5 – 2.5 mm, in the Z direction, from its corresponding TP structures. The ME1/2 chamber approaches its corresponding MAB structure in the $R\Phi$ direction by values ranging between 2 and 4 mm, while getting apart from its corresponding TP structure, in the same $R\Phi$ direction, by about 3 mm.

Given the weights and geometrical dimensions of detector components, the magnitude of the magnetic field forces and the presumably non-negligible frictions between touching elements, the property of elasticity between magnet-on and magnet-off states is not perfect in the motions of the CMS structures. Furthermore, we have noticed that equal magnetic field intensity results in different motions between observed objects. However, discrepancies stay below the ~0.5 mm or ~1 mm (for $R\Phi$ and Z respectively), which seems remarkably good stability from run to run.

The displacements due to the magnetic forces do not depend merely on the square of the magnetic field intensity (current in the coils). Most often a non negligible linear term is necessary to fit the motion and for some couple of pieces a third degree B function is

needed to describe the recorded data. This is clearly showing that other forces, in addition to the magnetic field ones, enter also in play, mainly gravity and frictions between touching elements.

Concerning rotations during the ramp up to 3.8 T, the monitoring of Φ tilts of the LDs (YN1 disks), the ARs and BDs (TK body) and MABs structures show measured values compatible with zero at two standard deviations ($\sim 100 \mu\text{rad}$).

Finally, the comparison of the analysed data resulted in a very good agreement (better than $300 \mu\text{m}$ for displacements and $100 \mu\text{rad}$ for rotations) between the observations done on and under ground as well as between both CMS Z sides.

References

- [1] The CMS Collaboration, “The CMS experiment at the CERN LHC”, submitted to Jinst
- [2] The CMS Collaboration, “The Magnet Project Technical Design Report”, CERN/LHCC 97-10.
- [3] The CMS Collaboration, “The Muon Project Technical Design Report”, CERN/LHCC 97-32.
- [4] V. Karimaki, and G. Wrochna, CMS TN/94-199; F. Matorras and A. Meneguzzo, CMS TN/95-069 and I. Belotelov et al. CMS NOTE 2006/017. .
- [5] “The CMS Magnet Test and Cosmic Challenge (MTCC Phase I and II), Operational Experience and Lessons Learnt” CERN/LHCC 2007-011, LHCC-G-129, CMS Note 2007/005, March 7, 2007.
- [6] P. Arce and A.L. Virto, "CMS Object Oriented Code for Optical Alignment (COCOA)", CMS Note 2002/060.
- [7] The CMS Collaboration, “The Tracker Project Technical Design Report”, CERN/LHCC 98-06.
- [8] Marcus Hohlmann et al., “Design and Performance of the Alignment System for the CMS Muon Endcaps”. CMS CR-2008/016
- [9] A. Calderón et al., Nucl. Instr. and Methods A 565 (2006) 603.
- [10] "Amorphous Silicon Position Detectors for the Link Alignment System of the CMS Detector: Users Handbook", A. Calderón et al., CIEMAT 1126, December 2007.
- [11] C. Kholer et al., NIMA50250, DOI: 10.1016/j. nima.2009.06.058 (in press).
- [12] Sakae Tsushin Kogyo Co., Ltd. - Trade Dept. 322 Ichinotsubo, Nakahara-ku, Kawasaki-city, Kanagawa-prefecture, 211-0016 Japan.
(<http://www.sakae-tsushin.co.jp>)
- [13] Omron Corporation, Tokyo Head Office, 3-4-10 Toranomom Minato-ku, Tokyo 105, Japan. (<http://www.omron.com>).
- [14] “Proximity sensors Link Alignment System of the CMS Experiment: Users Handbook”, J. Alberdi et al. CIEMAT (to be published).
- [15] Applied Geomechanics Incorporated. 1336 Brommer Street, Sanya Cruz, CA 95062 USA. (<http://www.geomechanics.com/>).
- [16] “A Review of the Magnetic Forces in the CMS Magnet Yoke”, F. Kircher et al., CMS Note 1998/048.
- [17] <http://www.sentron.ch/>
- [18] J. Alberdi et al., Nucl. Instr. And Methods A 574 (2007) 199.
- [19] L.A. García Moral et al., Nucl. Instr. And Methods A 606 (2009) 344.
“Geometría del detector CMS reconstruida con el sistema de alineamiento Link”. Text in English. M. Sobrón, Ph. D. thesis. CSIC-University of Cantabria, Santander September 2009.
- [20] J. Alberdi et al., Nucl. Instr. and Methods A 593 (2008) 608.
- [21] “Tiltmeters for the Alignment System of the CMS Experiment: Users Handbook”, J. Alberdi et al. CIEMAT 1107, May 2007.
- [22] J. Alberdi et al., Nucl. Instr. And Methods A 574 (2007) 199.
- [23] “Amorphous Silicon Position Detectors for the Link Alignment System of the CMS Detector: Users Handbook”, A. alderón et al., CIEMAT 1126, December 2007.